Progress on electrochemical and photoelectrochemical urea and ammonia conversion from urine for sustainable wastewater treatment

Sophia Akkari, Carlos M. Sánchez-Sánchez, Guillaume Hopsort, Karine Groenen Serrano, Karine Loubière, Théodore Tzedakis, Raihana Benyahia, Lamia Rebiai, Stéphane Bastide, Christine Cachet-Vivier, et al.

Applied Catalysis B: Environment and Energy 362 (2025) 124718

Contents lists available at ScienceDirect

Applied Catalysis B: Environment and Energy

journal homepage: www.elsevier.com/locate/apcatb

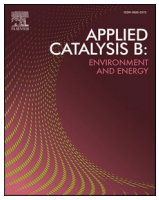

Progress on electrochemical and photoelectrochemical urea and ammonia conversion from urine for sustainable wastewater treatment

Sophia Akkari [a], Carlos M. Sánchez-Sánchez [a,*], Guillaume Hopsort [b,*], Karine Groenen Serrano [b], Karine Loubière [b], Théodore Tzedakis [b], Raihana Benyahia [c], Lamia Rebiai [c], Stéphane Bastide [c], Christine Cachet-Vivier [c], Vincent Vivier [d], Melissa Lopez-Viveros [e], Sam Azimi [e]

[a] Sorbonne Université, CNRS, Laboratoire Interfaces et Systèmes Electrochimiques (LISE), 4 place Jussieu, Paris F-75005, France
[b] Laboratoire de Génie Chimique, Université de Toulouse, CNRS, INPT, UPS, Toulouse, France
[c] Univ Paris Est Créteil, CNRS, ICMPE, UMR 7182, 2 rue Henri Dunant, Thiais 94320, France
[d] Sorbonne Université, CNRS, Laboratoire de Réactivité de Surface, LRS UMR 7197, Paris F-75005, France
[e] Direction de l'innovation, SIAAP, 82 avenue Kléber, Colombes 92700, France

ARTICLE INFO

Keywords:
Wastewater treatment
Urine valorization
Urea electro-oxidation
Ammonia electro-oxidation
Electrocatalysis
By-products
Photoelectrochemical reactors

ABSTRACT

The valorization of urine through the electro-oxidation of urea offers a promising alternative for industrial wastewater treatment plants. This operation, implemented at room temperature, allows, in addition to the depolluting action, the generation of hydrogen at the cathode. Using inexpensive electrodes and photo-assisting the process, this method has potential for industrial application. This review delves into the recent advancements in the electrochemical treatment of urea and ammonia from urine, understanding and optimizing the electrolysis process under various conditions. Notably, the electrolysis of urea and ammonia in alkaline medium over nickel oxyhydroxide (NiOOH) catalyst, has emerged as a promising avenue, offering enhanced selectivity and efficiency. The exploration extends to urine management, urea degradation, catalyst deactivation, reaction selectivity, and the detection of reaction products, as well as photoelectrochemical processes in a future reactor perspective, where the synergistic combination of photocatalysis and electrochemical oxidation opens new pathways for urine valorization.

Abbreviations: AOR, Ammonia Electro-oxidation Reaction; ATR-IR, Attenuated Total Reflection InfraRed; BDD, Boron Doped Diamond; ClER, Chlorine Evolution Reaction; CP, Carbon Paper; CPC, Compound Parabolic Collector; COD, Chemical Oxygen Demand; CV, Cyclic Voltammetry; DAFC, Direct Ammonia Fuel Cell; DEMS, Differential Electrochemistry Mass Spectroscopy; DFT, Density Functional Theory; DNA, Deoxyribonucleic acid; E^o, Thermodynamic standard potential [V]; E^o_{cell}, Overall cell potential [V]; E_{anode}, Anodic potential [V]; E_{app}, Applied potential [V]; EEO, Electric energy per order [Wh]; EAOP, Electrochemical Advanced Oxidation Process; EDS, Energy-dispersive x-ray Spectroscopy; EIS, Electrochemical Impedance Spectroscopy; F, Faraday constant [96485 C mol^{-1}]; FE, Faradaic efficiency [%]; FTIR, Fourier-Transform Infrared Spectroscopy; FTO, Fluorine-doped Tin Oxide; GC, Gas Chromatography; HER, Hydrogen Evolution Reaction; IC, Ionic Chromatography; j, Current density [A m^{-2}]; LCA, Life Cycle Assessment; MAV, Marne Aval Plant; MS, Mass Spectroscopy; MIS, Metal–Insulator–Semiconductor; N, Number of electrons transferred [dimensionless]; NF, Ni Foam; NHE, Normal Hydrogen Electrode; NP, Nanoparticle; OER, Oxygen Evolution Reaction; P, Photolysis; PANI, Polyaniline; PB, Prussian Blue; PC, Photocatalysis; PEC, Photoelectrochemical; PECR, Photoelectrochemical Reactor; R_e, R_p, R_{pe}, Efficiencies of electrochemical, photocatalytic and photo-electrochemical processes, respectively [dimensionless]; RDE, Rotating Disk Electrode; RHE, Reversible Hydrogen Electrode; RPM, Revolution per Minute; SAV, Seine Aval Plant; SCE, Satured Calomel Electrode; SEC, Seine Centre Plant; SEG, Seine Grésillons Plant; SEM, Seine Morée Plant; SERS, Surface-Enhanced Raman Spectroscopy; SEV, Seine Valenton Plant; SF, Synergetic Factor [%]; SHE, Standard Hydrogen Electrode; SIAAP, Greater Paris Sanitation Authority; STH, Solar-to-H_2 conversion efficiency [%]; TCO, Transparent Conductive Oxide; TKN, Total Kjeldahl Nitrogen [kg m^{-3}]; TN, Total Nitrogen [kg m^{-3}]; TOC, Total Organic Carbon [kg m^{-3}]; TRL, Technology Readiness Level; UOR, Urea Electro-oxidation Reaction; WWTP, Wastewater Treatment Plant; XPS, X-ray Photoelectron Spectroscopy; $\Delta_f Gj^\circ$, Standard Gibbs free energy of formation [J mol^{-1}]; $\Delta_R G^\circ$, Standard Gibbs free energy of reaction [J mol^{-1}]; η, Overpotential [V]; ν, Stoichiometric coefficient [dimensionless]; υ, Scan rate [V s^{-1}].

* Corresponding authors.
E-mail addresses: carlos.sanchez@sorbonne-universite.fr (C.M. Sánchez-Sánchez), hopsort.guillaume@gmail.com (G. Hopsort).

https://doi.org/10.1016/j.apcatb.2024.124718
Received 24 June 2024; Received in revised form 4 October 2024; Accepted 16 October 2024
Available online 20 October 2024

1. Introduction

1.1. Motivation for treating urine from large-scale wastewater effluents

It is a well-known fact that urban wastewater contains a mixture of organic molecules and minerals from different origins and that urine represents 80 % of the total nitrogen (TN) load in raw wastewater. Natural urea contained in urine has been studied for a long time as an alternative to synthetic urea produced as fertilizer (with energy and pollution savings) [1,2]. More recently, it has been also envisaged as a molecular carrier for energy production through hydrogen gas production from paired electrolysis. The urea resource from human urine represents ~60 Mt per year (average of ~20 g per day and per person), *i.e.*, one-third of the worldwide demand for synthetic urea (~200 Mt per year).

Previous works [3–5] have demonstrated that diverting urine from wastewater treatment plants (WWTPs), can significantly reduce energy consumption in water decontamination. Wilsenach et al. [6] estimated that nitrogen removal requires around one-half of the total energy demand in WWTPs (mainly due to the intensive aeration required) [7,8]. Hence, urine diversion is gaining interest since the diverted urine is a valuable resource, in addition to the environmental and economic benefits it offers to the WWTPs. For example, the Parisian WWTPs operated by the Greater Paris Sanitation Authority (SIAAP), treated in 2020 close to 110 tons per day of nitrogen from the wastewater produced by close to 9 million inhabitants. This illustrates the present interest in evaluating the impact of urine separation at the source and separate urea treatment. The Parisian case includes 6 WWTPs located upstream and downstream of the Parisian conurbation in the Seine river and their flows vary between 50 000 and 1 700 000 m^3 per day, as presented in Fig. 1. Different technologies for water treatment are implemented in each case as described in detail in Table 1. For instance, the Seine Valenton plant (SEV) uses activated sludge treatment, the Seine Centre (SEC) plant the biofiltration process and the Seine Aval plant (SAV) has two treatment lines, biofilters (80 % of treated water) and membrane filtration (20 % of treated water). This fact might impact

Table 1
Data on the three Parisian WWTPs operated by the SIAAP.

	SEV	SEC	SAV
Nominal hydraulic capacity (m^3 day^{-1})	600 000	240 000	1 700 000
Population equivalent	2 500 000	800 000	5 000 000
Treatment layout in nominal conditions	Pre-treatment – Primary settling – Extended aeration activated sludge – Tertiary physicochemical dephosphatation	Pre-treatment – Physico-chemical lamellar settling – 3 stages biofiltration	Pre-treatment – Primary settling – 2 lines of biological treatment Line 1 (80 % of water) = 3 stages of biofiltration (pre-denitrification – total nitrification – post-denitrification), Line 2 (20 % of water) = Membrane bioreactor
TN (mg_N L^{-1}) [%Removal][a]	63 [70 %]	43 [69 %]	51 [63 %]
Energy consumption attributed to aeration (kWh day^{-1})[b]	84 780	30 861	251 131
Air consumption (Nm^3 air per kg of N-TKN treated)	121	149	106

[a] Average Total Nitrogen (TN) at inlet in 2020.
[b] Average air consumption from 2018 to 2020, energy calculated based on a rate of 0.033 kWh Nm^{-3} [7].

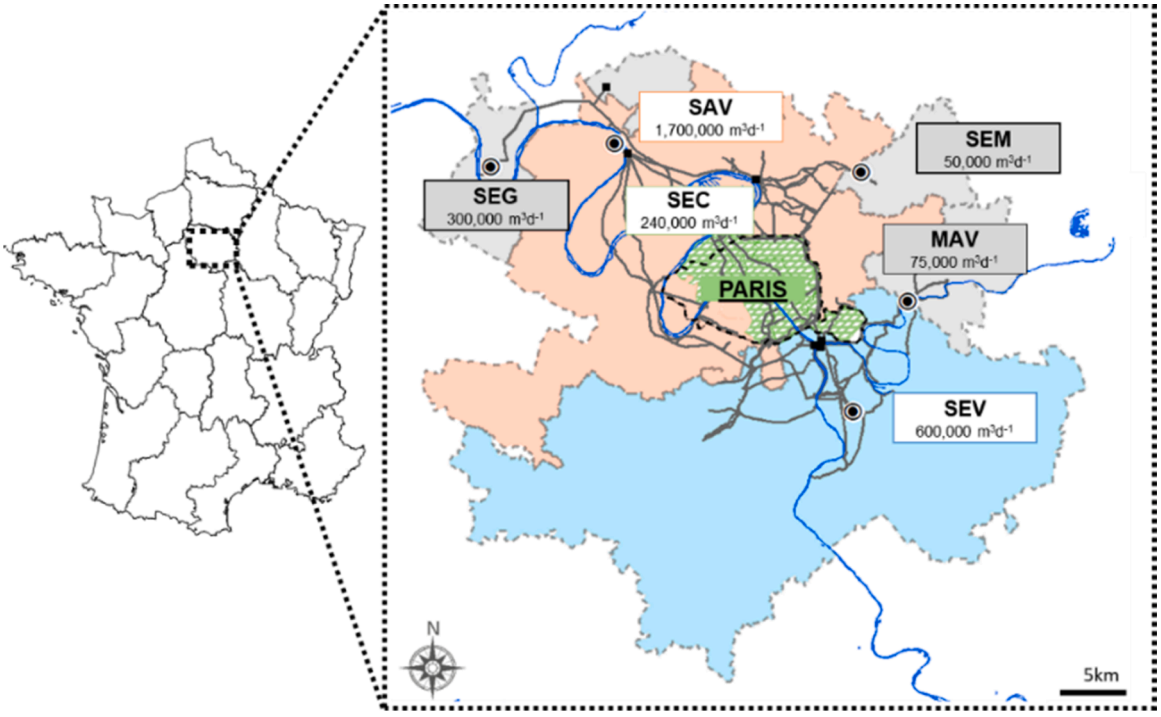

Fig. 1. Location and nominal flow rate of the 6 Parisian WWTPs operated by the SIAAP. The 3 plants mentioned as example here are identified by a white box (SEV, SAV and SEC). Reprinted from [9], with permission from SNCSC.

on the efficiency of diverting urine from wastewater effluents.

According to some recent simulations, Badeti et al. [10] found that around 33 % of energy consumption attributed to aeration could be saved by implementing 90 % urine diversion, representing a daily gain of 27 MWh, 10 MWh and 83 MWh for SEV, SEC and SAV respectively. Thus, urine diversion and treatment concentrate a lot of attention to reduce operational costs in WWTPs [11–13] and their environmental and economic impact need to be evaluated using life cycle assessment (LCA) methodology [11,14].

In the following section, the methods for urine manangement and degration into ammonia will be described.

1.2. Urine management and urea degradation into ammonia

1.2.1. Chemical and enzymatic degradation

The spontaneous hydrolysis of urea ($CO(NH_2)_2$) into two ammonium cations (NH_4^+) and carbon dioxide (CO_2) might significantly impact the final amount of nitrogen as urea reaching the WWTPs, as well as the effluent pH due to the alkalinization produced by the formation of ammonia (NH_3) in equilibrium with NH_4^+ (pKa 9.25 at 25°C). The urease enzyme, illustrated in Fig. 2a, highly abundant in nature, is the main responsible of the rapid biological decomposition pathway of urea into ammonia. Fig. 2b shows the two main pathways for urea decomposition (chemically and biologically). This enzymatic decomposition reaction is already well-described in the bibliography [15–17], and initially leads to carbamate and ammonia, with subsequent carbamate hydrolysis into carbonic acid and a second molecule of NH_3.

In contrast, the chemical urea decomposition firstly produces NH_4^+ and cyanate (^-OCN) [19] and subsequently it is followed by ^-OCN hydrolysis reaction as described in **reactions (1)** and **(2)**, respectively.

$$CO(NH_2)_2 \leftrightarrow NH_4^+ + {}^-OCN \quad (1)$$

$$^-OCN + H_2O + 2H^+ \leftrightarrow NH_4^+ + CO_2 \quad (2)$$

Marier and Rose [20] have studied the chemical urea decomposition at various temperatures and different urea concentrations. At 25°C, they found that cyanates were produced at a rate of 0.07 mmole of $^-OCN\ L^{-1}\ day^{-1}\ mol^{-1}_{urea}$ and with a maximum rate of accumulation after 60 days. At a given urea concentration, the maximum cyanate level at 25°C was ca. 60 % of that obtainable at 38°C after 7 days, and ca. 23 % of that obtained at 85°C after 50 min. Cyanate accumulation was prevented by storage of neutral solutions of urea at 5°C, or by buffering the urea solutions at pH 4.7. More recently, Lilov and Kirilov [19] have studied the decomposition of 8 M urea solution at 298 K for up to 150 days of storage. The concentration of ammonium cyanate increased until it reached a maximum value and then slowly decreased. The urea degradation rate was found to be equal to 0.166 %. In addition to this, Udert et al. performed a study on the practical implications of precipitate formation during the selective collection of urine due to urea degradation, and its potential to cause pipe blockages. X-ray diffraction was used to identify the composition of the precipitate formed, which was found to be $CaCO_3$ from the chemical and enzymatic urea hydrolysis, as well as struvite ($NH_4MgPO_4{\cdot}6H_2O$) and octacalcium phosphate ($Ca_8H_2(PO_4)_6{\cdot}5H_2O$) from the enzymatic decomposition of urine [21, 22]. Thus, physical separator systems should be considered to treat the collected urine separately from solid precipitates.

1.2.2. Urea stabilization by alkalinization of urine

Human urine contains between 0.2 and 0.33 M of urea, besides a long list of ions and molecules (NaCl, KCl, NH_4Cl, Na_2SO_4, creatinine, uric acid…), which results in a complex aqueous matrix of neutral pH [13,16,23,24]. In presence of urease, urea is biologically degraded to ammonia, which is a volatile and malodorous product and causes nutrient loss and clogging of urine collection systems due to carbonate and phosphate precipitates. Among other possible treatments, alkaline treatment of the collected urine prevents the degradation of fresh urea by blocking the action of urease enzymes [13,25]. Thus, Randall et al. [26] have investigated the addition of $Ca(OH)_2$ to fresh urines and recommended a dosage of 10 g of $Ca(OH)_2$ per liter to ensure an alkaline enough pH value by the presence of solid $Ca(OH)_2$ in the urine collector reactor. Moreover, to prevent chemical degradation of urea, they also recommended keeping the urine temperature between 14°C and 40°C. Nevertheless, the massive presence of Ca^{2+} in the chemically alkalinized urine provokes scaling and clogging in the pipelines during downstream processing. Thus, only K^+ or Na^+ based hydroxides might be useful for urine alkalinization without generating additional complications. An alternative electrochemical-based method for alkalinization has been also explored by De Paepe et al. [27]. This system generates hydroxyl anions by electrolysis at the cathode, leading to a pH increase in the urine effluent, but without the addition of solid $Ca(OH)_2$. As a result, urine was stabilized for one week at pH 11 and was stored without urea hydrolysis at pH 12 for more than 18 months, as well as scaling in the pipelines was minimized. Nevertheless, the release of treated water effluents into the environment requires neutral pH values and thus, a subsequent neutralization step should be required after the urea treatment.

1.2.3. Electrochemical treatment of urea as a promising process

Different chemical and biological methods have been already explored to treat water effluents containing urea [13]. Bio-based and microfiltration are the most conventionally used methods, but these methods suffer from membrane fouling. Various others non-EC methods of urea removal are well-developed, with hydrolysis of urea being the most effective. However, this process requires high temperature and pressure, limiting its industrial-scale application. Enzymatic decomposition of urea is also effective, but enzyme stability is a concern. Biological methods involve bacteria strains in biofilters but are not selective, and using oxidizing agents requires an affordable, non-toxic

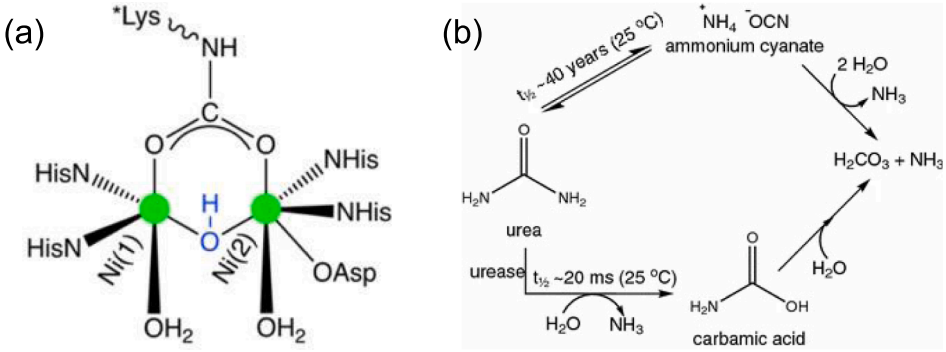

Fig. 2. (a) Urease enzyme representation. (b) Urea chemical and enzymatic decomposition pathways.
(a) Adapted from [18], with permission from John Wiley and Sons. (b) Reprinted from [16], with permission from Springer Nature BV.

oxidant. Adsorbents are an evolving method, but optimization is still under investigation. Catalytic decomposition is expensive due to catalyst costs and requires optimization for maximum efficiency [28]. However, choosing the appropriate method depends on various factors, such as wastewater concentration, required purity, and process cost [29, 30].

Electrochemical [31–36] and photoelectrochemical [37–39] methods represent an attractive alternative for this purpose because they operate at ambient temperature and no addition of chemicals is required except to maintain an alkaline pH. In addition to this, they benefit from simultaneous wastewater treatment and hydrogen production in a paired electrolysis, where both reactions at the anode and the cathode provide useful products and maximize the efficiency of the provided electrons. Thus, urea is electrochemically oxidized at the anode, meanwhile hydrogen gas (H_2) is produced at the cathode. This type of green production of H_2 by electrolysis concentrates a lot of attention as an alternative to carbon-based methods [40–43] and represents one of the main reasons why we consider this review article timely.

1.3. Scope and objectives of the present review

This review article is focused on electrochemical (EC) and photoelectrochemical (PEC) pathways to treat urine for reaching a N-free effluent while generating green hydrogen at the cathode. The originality is to cover the whole chain, from *(i)* the impact of the selective urine collection into the WWTPs and urea stabilization to avoid its degradation, *(ii)* to the electrochemical treatment of either fresh or stored urine, highlighting the presence of urea, ammonia or both species simultaneously. In particular, H_2 production efficiency is considered from an overpotential point of view thanks to the thermodynamic evaluation of different reaction products and electrocatalytic materials. Moreover, this review article covers *(iii)* recent advancements on the detection of urea and ammonia electro-oxidation byproducts, their corresponding reaction mechanisms and the impact of the urine matrix effect on catalyst deactivation, as well as *(iv)* the current status in terms of reactors and photoreactors available for such urine-based waste electro-oxidation, including the potential advantages of applying PEC processes to urine conversion, which is a non-developed approach until now.

To sum up, this review article describes different aspects of urine valorization that have never been addressed in the literature before in such a closely interconnected way. It is noteworthy *(i)* the industrial context of urine separation at the source and its economic impact on the WWTPs; *(ii)* the urea electro-oxidation reaction (UOR), but in the context of the urine matrix, which might produce the formation of toxic chloramines by active chlorine indirect oxidation, *(iii)* the coexistence of two electroactive species (urea and ammonia) when treating stored urine, which were never addressed jointly before, either from the electrocatalysis or the hydrogen production point of view. Thus, a comparative study of catalytic materials for both ammonia electro-oxidation reaction (AOR) and UOR is included here. While most of the previous review articles presented UOR producing N_2/CO_2 as an alternative reaction to oxygen evolution reaction (OER) for diminishing the electrochemical overpotential of H_2 production, the present article addresses the question of the production of all other detected products from UOR (*e.g.*, ammonia, cyanate, carbonate, nitrite, etc.). In particular, the thermodynamic potential value of UOR and AOR is calculated taking into account all formed potential products. Finally, a great effort is devoted to point out future development perspectives for urine valorization processes by reviewing some relevant chemical engineering aspects linked to PEC methods such as type of reactor and illumination source. They were never reported before for urine treatment, most previously reported efforts on PEC methods being concentrated on the design of new photoanodes.

2. Electrochemical treatment of urea and ammonia from urine

Early in the 70's and 80's, initial studies of UOR were undertaken for the development of an artificial kidney, the role of which was to convert urea to ammonia and carbon dioxide [44,45].Then, the first studies involving UOR from urine treatment were performed in the 90' s using platinized electrodes (8 rod type electrodes) introduced into a simple sealed reactor magnetically stirred (with or without flow) with the aim of achieving UOR from internal body solutions (*i.e.*, dialysis application) [46]. The authors reported NH_3 and CO_2 as the main products and showed that the anode potential should be kept below 1.1 V *vs.* $Ag/AgCl/Cl^-$ in order to avoid ClO^- formation by the oxidation of the Cl^- present into the physiological solutions. They claimed the passivation of the electrode and the need to reverse its polarity so as to activate it again. Note that ClO^- electrogenerated on Ni/Co/Rh alloy anode contributed to the urine chemical (homogeneous) degradation, as mentioned later by other authors [47]. In the following decades, a lot of effort was focused on optimization of the electrocatalyst material in order to improve its activity and long-term stability, being the Ni-based alloys the most studied materials for UOR. However, the presence of other electroactive organic molecules present in the urine matrix provoked in most cases the deactivation of those electrodes. Only recently, the UOR mechanism was enriched by the detection of new intermediates and products. Nowadays, there is a rebirth of the interest on UOR [48] mainly focused on the quest of selectivity towards innocuous products (N_2 and CO_2), which usually represents only a fraction of the overall UOR products.

The AOR has received considerable attention as a promising carbon-free energy source and wastewater treatment. Some initial studies in the 60's [49–52] showed that ammonia could be applied in fuel cells combined with oxygen in the Direct Ammonia Fuel Cell (DAFC). Since then, many different investigations have been done on AOR in recent decades.

This section addresses the electrochemical treatment of urine, exploring its electrolysis under various conditions, ranging from fresh urine in chloride-rich media to stored urine where ammonia is the main N-containing compound. Thus, this section covers both urea and ammonia electro-oxidations by reviewing the thermodynamics and the most active electrocatalysts for these reactions, specifically focusing on the low-cost, long-term activity and stability of NiOOH electrodes in alkaline media.

2.1. Electrolysis of fresh urine in presence of chloride

The UOR from fresh urine (pH = 5.5 – 7) takes place in near-neutral medium [13,22] and has been only explored in presence of chlorides (Cl^-) as mentioned by Urbanczyk et al. [28], since 3600 ppm Cl^- (≈ 0.1 M) are present in the standard urine composition [23]. In particular, Simka et al. [53] studied urea oxidation varying the Cl^- concentration in solution on platinum and titanium anodes covered with ruthenium and titanium oxides. In these conditions, urea seems to be oxidized directly on the anode surface through **reaction (3)** or indirectly by electrogenerated active chlorine species, typically hypochlorite (ClO^-), through **reaction (4)**. Li et al. [54] compared the ability of boron-doped diamond (BDD) and IrO_2 anodes, for the UOR, in artificial human urine, at neutral pH, in a single-compartment cell. They found that urea and all other organic compounds present in this artificial urine were efficiently mineralized by the electrocatalytic process, as well as NH_3 from urea hydrolysis, which represented 5 % of the initial urea concentration in this case. However, the anode material had a significant impact on the final products obtained. Fig. 3 compares BDD and IrO_2 anodes for urine oxidation proposed by Li et al. On BDD, the hydroxyl radicals ($^{\bullet}OH$) electrogenerated from water oxidation through **reaction (5)** would be responsible for the oxidation of the majority of the organic compounds, because they would be weakly physisorbed and are therefore available to react with the target compound. Besides, the Cl^- mediated oxidation through ClO^- was responsible for the oxidation of ammonia (that is

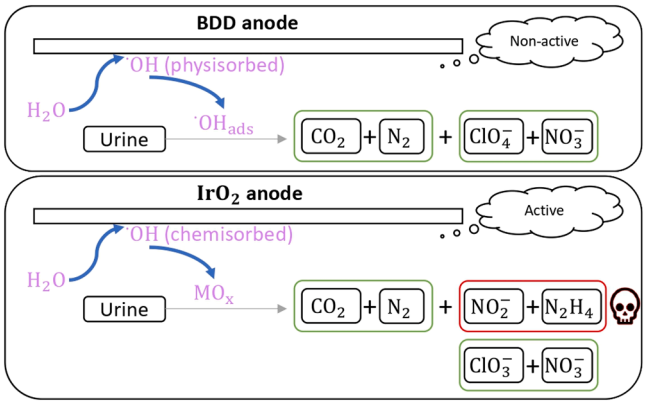

Fig. 3. Schematic representation of UOR in artificial human urine at neutral pH on either BDD or IrO_2 anodes. Adapted from [54], Copyright (2015), with permission from Elsevier.

coming from urea hydrolysis), resulting the formation of nitrate (NO_3^-) and perchlorate (ClO_4^-) as byproducts. In contrast, on the IrO_2 anode, the generated hydroxyl radicals through **reaction (5)** would be strongly chemisorbed, and electrogenerated ClO^- would be responsible for the oxidation process. As a result, the incomplete oxidation of nitrogen species produced toxic byproducts such as hydrazine (N_2H_4) and nitrite (NO_2^-) due to the lower oxidation power of ClO^- in comparison with hydroxyl radicals.

$$CO(NH_2)_{2(aq)} + 6OH^{\bullet} \rightarrow N_{2(g)} + 5H_2O_{(l)} + CO_{2(aq)} + 6e^- \quad (3)$$

$$CO(NH_2)_{2(aq)} + 3ClO^-_{(aq)} \rightarrow N_{2(g)} + 3Cl^-_{(aq)} + 2H_2O_{(l)} + CO_{2(aq)} \quad (4)$$

$$H_2O_{(l)} \rightarrow {}^{\bullet}OH_{(aq)} + H^+ + e^- \quad (5)$$

2.2. Electrolysis of stored urine with simultaneous urea and ammonia oxidations

The composition of fresh and stored urines [55,56] keeps unchanged the Cl^- concentration (≈ 0.1 M), but show three main differences: the urine effluent pH becomes alkaline (pH = 8.8–9.1), neither Ca^{2+} nor Mg^{2+} cations are present anymore in the solution and ≥90 % of the total nitrogen in solution is in the form of NH_3 in stored urine [13,22]. Amstutz et al. [56] compared the electrochemical removal of nitrogen from synthetic solutions of fresh and stored urine on IrO_2 electrodes at 15 mA cm^{-2} in a single-compartment cell. They showed that in fresh synthetic urine, urea is efficiently eliminated from solution (72.4 % of total nitrogen removal). In contrast, in stored synthetic urine, where a significant part of urea has been already transformed into NH_3 by hydrolysis, the presence of carbonate inhibits AOR and a poor total nitrogen removal is reached (10.3 %). Zöllig et al. [57] assessed the feasibility of direct AOR to form either N_2 through **reaction (6)** or NO_3^- through **reaction (7)** from both synthetic and real stored urine on graphite anode at pH 9. Potentiostatic electrolysis at 1.31 V *vs.* SHE were tested to achieve direct electron transfer on the anode surface and avoid indirect oxidation of NH_3 through active chlorine and subsequent formation of chlorinated compounds. It was also demonstrated that only NH_3 was oxidized, whereas NH_4^+ remained electrochemically inert. Fig. 4 shows the correlation between the current density from AOR and the bulk pH of the solution. Thus, NH_3 can be efficiently degraded in alkaline pH solutions by direct AOR, but not in neutral and acidic conditions. The removal rate of NH_3 during AOR at 1.31 V *vs.* SHE in real stored urine was 2.9 ± 0.3 g_N m^{-2} d^{-1} mainly forming gaseous nitrogen species. This rate normalized by anode surface area (m^2) and time (d) was slightly faster than the one from the biological process. In contrast, NH_3 removal rate by galvanostatic electrolysis on BDD and IrO_2 anodes

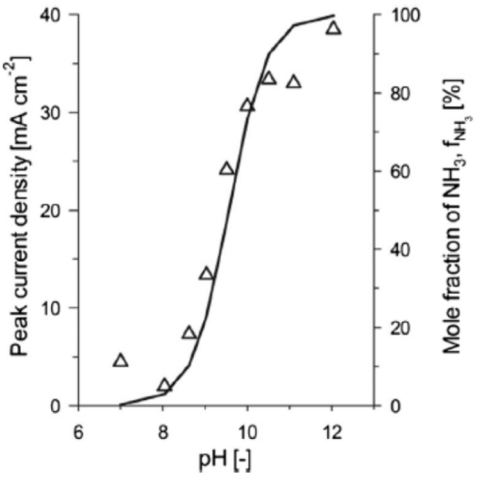

Fig. 4. Correlation between peak current density associated with AOR from cyclic voltammetry on graphite electrode (triangles) and the mole fraction of ammonia (solid line) as a function of bulk pH in supporting electrolyte ($NaClO_4$ 1 M). Scan rate: 200 mV s^{-1}; T= 25 °C. Reprinted from [57], Copyright (2015), with permission from Elsevier.

[58] exhibited a dominant indirect active chlorine-mediated oxidation pathway through **reactions (8)** and **(9)** for NH_3 removal in stored urine. 43 ± 20 g_N m^{-2} d^{-1} and 227 ± 16 g_N m^{-2} d^{-1} were the NH_3 removal rates achieved on BDD and IrO_2, respectively, at 20 mA cm^{-2}. Thus, IrO_2 was found to be a more suitable anode for NH_3 elimination, but BDD revealed more efficient for simultaneously decreasing the organic content in the urine matrix, which is evaluated by the analysis of the chemical oxygen demand (COD). Alternatively, the direct AOR might also produce NO_2^- through **reaction (10)**. However, it has not been reported for the case of treating NH_3 from stored urine. In contrast, selective NO_2^- production from direct AOR on $Ni_{0.8}Cu_{0.2}$ oxyhydroxide electrodes was reported in highly alkaline solution [59].

Chun et al. [60] implemented the active chlorine-mediated electrochemical oxidation treatment on diluted human urine (1:20 v/v urine: water) by adding 40 mM NaCl (1420 ppm Cl^-) to the diluted urine solution and using a $Ti/IrO_2/TiO_2$ anode. The removal rates of NH_3 and total nitrogen in solution were measured at 85 % and 71 %, respectively, after 6 h of treatment. The authors concluded that treated diluted urine could be successfully recycled as flush water in a close toilet system interesting for remote areas, but they did not exclude the formation of chlorinated organic substances. Garcia-Segura et al. [61] studied the generation of organochlorinated byproducts during the indirect active chlorine-mediated oxidation process on a BDD anode. Those byproducts are formed by the reaction of active chlorine species with NH_3 and might yield monochloramines (NH_2Cl), dichloramines ($NHCl_2$) and/or trichloramines (NCl_3). In particular, different water matrices, containing between 0.1 and 0.5 M of Cl^- in addition to either 0.1 M NH_4^+ or 0.1 M urea at neutral pH were studied by *in situ* differential electrochemistry mass spectroscopy (DEMS), which allowed on-line quantification of chloramine formation. Monochloramine production from either NH_4^+ or urea solutions at pH 8 reached current efficiency values of 4.0 % and 0.9 %, respectively, favoring the chlorination of NH_4^+. This pathway becomes inhibited at high alkaline conditions due to activation of the hydroxyl radicals production on the BDD electrode through **reaction (5)**. Moreover, synthetic fresh urine containing less than 5 % of the total nitrogen in solution in the form of NH_4^+/NH_3 was evaluated by DEMS showing that electrogeneration of chloramines in actual fresh urine matrices is of low relevance with current efficiencies below 0.5 %, which will not likely be the case in stored urine matrices containing a much higher NH_4^+/NH_3 concentration. All these published works, except [61], were mainly focused on the detection of dissolved N-compounds, however N-gaseous products (N_2 particularly) were neither identified

nor quantified.

In conclusion, the fact that urea from urine gets spontaneously degraded during both storage at the collection point and transportation to the WWTPs indicates that UOR and AOR are likely concomitant reactions in most cases and require a comparative study of the most promising catalytic materials, as the one described later in Section 2.3. Moreover, a competitive reaction pathway between direct and indirect UOR and/or AOR is often reported due to the presence of ≈ 0.1 M Cl^- in both fresh and stored urines. Cl^- is the second most concentrated compound in urine and the presence of ClO^- (by-product of chlorine evolution reaction (ClER) in an alkaline environment) could provoke an accelerated corrosion of the anode due to its oxidising nature. In principle, OER occurs at anodic potentials higher than 1.23 V *vs.* RHE, whereas ClER occurs only when the applied potential is more positive than 1.72 V *vs.* RHE [62]. There could therefore be competition between the oxidation of $Ni(OH)_2$, water and Cl^- at high potentials (>1.72 V *vs.* RHE [63]). To the best of the authors' knowledge, no prevention work has been done on the anodic corrosion caused by the presence of chlorides in the context of the alkaline UOR. Nevertheless, research solution could be developed to avoid this possible passivation behavior, which has already been deployed in seawater electrolysis (typical chloride concentration of 19 g L^{-1} in seawater [64] and 5 g L^{-1} in fresh urine [65]). These include depositing a protective layer on the surface of the anode [66], pre-treating the effluent [67] or inserting a polyanionic layer to act as an electrostatic repulsive layer [68].

$$2NH_{3(aq)} + 6OH^- \rightarrow N_{2(g)} + 6H_2O_{(l)} + 6e^- \quad (6)$$

$$NH_{3(aq)} + 9OH^- \rightarrow NO_{3(aq)}^- + 6H_2O_{(l)} + 8e^- \quad (7)$$

$$2NH_{3(aq)} + 3ClO_{(aq)}^- \rightarrow N_{2(g)} + 3Cl_{(aq)}^- + 3H_2O_{(l)} \quad (8)$$

$$NH_{3(aq)} + 4ClO_{(aq)}^- \rightarrow NO_{3(aq)}^- + 4Cl_{(aq)}^- + H_2O_{(l)} + H^+ \quad (9)$$

$$NH_{3(aq)} + 7OH^- \rightarrow NO_{2(aq)}^- + 5H_2O_{(l)} + 6\ e^- \quad (10)$$

2.3. Electrocatalysts for urea and ammonia electro-oxidations

As previously discussed, an interesting alternative to handle the presence of NH_3 formed in stored urine, could be to find a catalyst that oxidizes both NH_3 and urea into N_2. Table 2 summarizes the set of catalysts used independently for both reactions including the experimental conditions and their activity performances. As shown in Table 2, most ammonia electrolyses were performed using low NH_3 concentrations, in contrast with urea electrolyses mainly performed in 0.33 M urea solutions (*i.e.*, physiological concentration of urea in urine). Moreover, AOR has been mainly performed using Pt-based catalysts, where two mechanism pathways have been proposed: *(i)* the N_2 formation mechanism [69], in which NH_3 is successively dehydrogenated into NH_{ads} that dimerizes with another NH_{ads} into NH_x–NH_y and undergoes dehydrogenation to form N_2 and *(ii)* the NO_2^- and NO_3^- formation mechanism [70], in which NH_3 is successively dehydrogenated to form N_{ads} that gets over-oxidized into NO_x, since the oxidation of N_{ads} is more thermodynamically favorable than the dimerization of N −N on Pt.

Table 2
Electrocatalyst performances during electrolysis for either UOR or AOR, including the experimental conditions and the products selectivity.

Material	Target molecule	Solution	Electrolysis conditions[a]	pH	Products (FE)	Ref.
$Pt_{70}Ir_{30}$	NH_3	0.1 M KOH 5 mM NH_3	E_{anode}=(0.4 – 1.0) V *vs.* RHE DEMS study	13	N_2 at (0.4–0.8) V *vs.* RHE N_2O and NO at >0.8 V *vs.* RHE	[76]
$Pt_{90}Ru_{10}/C$	NH_3	1 M KOH 1 M NH_4OH	j =25 mA cm^{-2} t = 8 h	≈14	NO_2^- (25 % of initial NH_3), NO_3^- (54 % of initial NH_3)	[77]
$Ni_{20\%} - WC_{20\%}/C$	Urea	1 M KOH 0.33 M urea	E_{anode}=(0.6 – 0.7) V *vs.* Hg/HgO	≈14	CO_2, ^-OCN by FTIR detection	[78]
$Ni(OH)_2$/NF	Urea	1 M KOH 0.33 M urea	E_{anode}=1.4–1.6 V *vs.* RHE t= 1 h	≈14	~65 % NO_2^- ~30 % N_2	[79]
$Ni_{0.8}Cu_{0.2}(OH)_2$/NF	Urea	1 M KOH 0.33 M urea	E_{anode}=1.4–1.6 V *vs.* RHE t= 1 h	≈14	~45 % NO_2^- ~55 % N_2	[79]
Activated-NF	Urea	1 M KOH 0.33 M urea		≈14	~76 % NO_2^- 15 % N_2 0.5 % NO_3^-	[80]
$NiMoO_4$ – NF	Urea	1 M KOH 0.33 M urea	E_{anode}=0.45 V *vs.* Ag/AgClt= 1 h	≈14	85 % NO_2^- 0.1 % NO_3^-	[80]
Ni – C/CP	Urea	1 M KOH 0.33 M urea		≈14	~85 % NO_2^- 0.2 % NO_3^-	[80]
NiO – NF-NF	Urea	1 M KOH 0.33 M urea		≈14	~77 % NO_2^- 0.3 % NO_3^-	[80]
Cu/Ni-B	Urea	1 M KOH 0.33 M urea	E_{anode}=1.7 V *vs.* RHE t= 1 h	≈14	~30 % NO_2^- ~70 % N_2	[81]
NiCoGe	Urea	1 M KOH 0.33 M urea	E_{anode}=1.4 V *vs.* RHE t= 1 h	≈14	~85 % NO_2^- ~15 % N_2	[74]
Ni – SO_x	Urea	1 M KOH 0.33 M urea	E_{anode}=1.4 V *vs.* RHE	≈14	~65 % NO_2^- ~30 % N_2	[82]
Ni – O – Ti	Urea	1 M KOH 0.33 M urea	E_{anode}=1.4 V *vs.* RHE	≈14	~100 % N_2	[75]
Ni – O – Ni	Urea	1 M KOH 0.33 M urea	t= 30 min	≈14	~40 % NO_2^- ~60 % N_2	[75]
Ni foam	Urea	1 M KOH 0.33 M urea		≈14	~55 % NO_2^- ~35 % N_2 ~10 % NO_3^-	[75]
$NiCu/MnO_2$	NH_3	0.5 M NaOH 55 mM NH_4Cl	E_{anode}=0.6 V *vs.* Hg/HgO	13.7	97 % N_2	[83]
$NiCu/MnO_2$	NH_3	0.5 M NaOH 55 mM NH_4Cl	E_{anode}=0.7 V *vs.* Hg/HgO	13.7	57 % N_2 25 % NO_x 18 % OER	[83]
$Ni_{0.8}Cu_{0.2}$ oxyhydroxide	NH_3	0.1 M KOH 0.5 mM $(NH_4)_2SO_4$	E_{anode}=1.53 V *vs.* RHE t= 3 h	13	98% NO_2^-	[59]
NiOOH	NH_3	0.1 M KOH 0.5 mM $(NH_4)_2SO_4$		13	25 % NO_2^- 16 % NO_3^- 59 % N_2	[59]
Ni foam	NH_3	0.1 M Na_2SO_4 20 ppm -N	E_{anode}=0.7–0.85 V *vs.* Hg/HgO t= 6 h	11	49–0 % N_2 3–19 % NO_3^- <1 % NO_2^-	[73]

[a]E (V/SHE) = E (V/Hg/HgO/1 M KOH) + 0.14 V and E (V/SHE) = E (V/Ag/AgCl/3 M KCl) + 0.197 V. E (V/RHE) = E (V/Ag/AgCl/3 M KCl) + 0.197 V + 0.059 pH

The mechanism of AOR on Ni-based catalysts has been less studied, but several reports exist in the bibliography [59,71–73]. They report that the final product is highly controlled by the applied potential during NH_3 electrolysis. N_{ads} is favored at high overpotentials and undergoes oxidation into NO_2^-, while NH_{ads} pathway is favored at lower overpotentials to generate N_2 [59,73]. Shih et al. [73] showed that the production yield of N_2-N on nickel foam decreased from 44.5 % to 21.3 % when the potential was swept from 0.75 to 0.85 V *vs.* Hg/HgO/OH^- (Fig. 5). Alternatively, bi-metallic Ni-based catalysts have been also proposed to improve the selectivity of AOR towards N_2 on $Ni(OH)_2$/NiOOH catalyst, which is mostly reported below 60 % (Fig. 6b). However, it has been found that introducing Cu into NiOOH improves the activity of AOR, but shifts its selectivity towards NO_2^- production instead of N_2 [59]. A similar NO_2^- generation enhancing effect has been reported for UOR using bimetallic (Co and Ge) co-doping on $Ni(OH)_2$ [74]. In contrast, atomically isolated Ni-O-Ti sites on Ti foam reach 99 % selectivity for N_2 production during UOR [75].

Finally, there are few examples in the bibliography of catalysts independently applied to both UOR and AOR in electrolysis. One of those scare cases is nanostructured $Ni(OH)_2$ doped with Cu for UOR electrolysis, where the presence of Cu increased the possibility for both N atoms to bind together favoring the NH−NH pathway, hence increasing the selectivity towards N_2 and doubling its faradaic efficiency (FE) to 55 % at 1.4 V *vs.* RHE (pH>14) (Fig. 6a) [79]. In contrast, a comparable electrocatalyst formed by NiOOH doped with $Cu(OH)_2$ nano-islands ($Ni_{0.8}Cu_{0.2}$) for AOR electrolysis at 1.53 V *vs.* RHE (pH = 13) increased the NH_3 conversion rate and showed selectivity of 98 % towards NO_2^- (Fig. 6b), meanwhile initially bare NiOOH electrode yielded around 60 % of N_2, 25 % of NO_2^- and 16 % of NO_3^-, but suffered from a low NH_3 conversion rate [59]. Thus, the specific synthetic route used to generate those two Ni_x-Cu_{1-x} catalysts seems to play a major role in the final product ratio FE(N_2):FE(NO_2^-) obtained from both urea and ammonia electrolysis.

2.4. Electrocatalyst deactivation during urea electro-oxidation

Recently, the UOR was investigated within the urine matrix by Carpentier et al. [84,85] on different anodic materials composed by Ni foam (NF) covered by $Fe_xNi_{1-x}(OH)_2$ or Fe-doped $Ni(OH)_2$. Those authors showed that the performance of those anodic materials for UOR in alkaline media was impacted by the presence of creatinine (the second most concentrated biological molecule in dialysate, 0.18 mM), which can be electrochemically oxidized and causes the anodic passivation of the NF electrode. In addition to the creatinine, other electroactive organic molecules (histidine and creatine) also present in the urine matrix together with urea have been identified as competitive electro-oxidation reactions, which contribute to the electrode deactivation [86]. Such electrode deactivation pointed out the need to recover/separate those organic molecules (pre-treatment step) before performing UOR in biological effluents at industrial scale. It is also important to mention that, in the presence of Cl^- from urine, pitting corrosion of the NF-anode occurred, due to the combined effects of the applied potential and the electrogenerated ClO^- acting as a corroding agent. Thereafter, different recommendations have been proposed in order to minimize the electrode corrosion, which is considered one of the major drawbacks in the UOR [32,87]. Among them, one can cite the use as anode/photoanode of some expanded metal, three dimensional composite Ni-based materials covered by NiOOH, Fe_2O_3, and nano-crystalline TiO_2 or RuO_2.

Noteworthy, several works have studied UOR isolated from the urine matrix and have demonstrated, by chronoamperometry and cyclic vol-

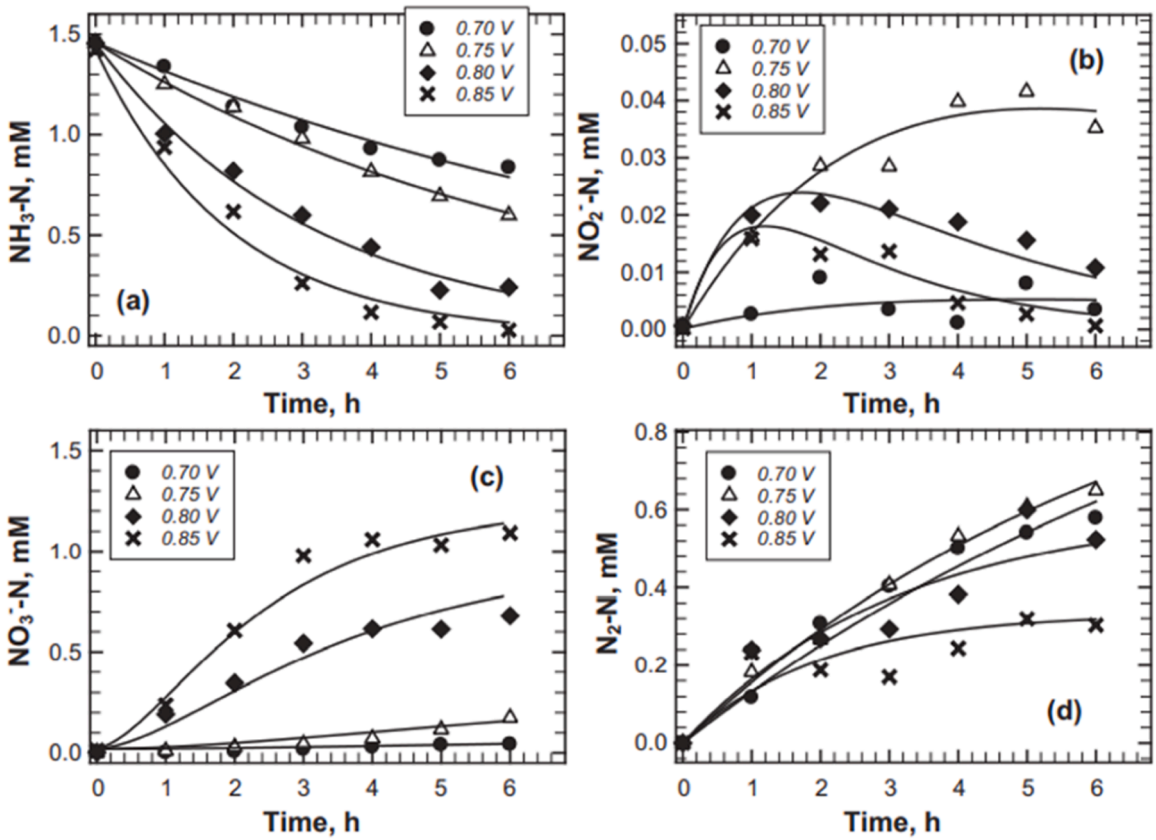

Fig. 5. Concentration changes of nitrogen species (a) NH_3-N, (b) NO_2^--N, (c) NO_3^--N, (d) N_2-N during batch electrolysis at constant potentials of 0.7–0.85 V *vs.* Hg/HgO/OH^- on nickel foam electrode as a function of reaction time. Initial [NH_3-N] = 20 ppm, pH = 11, 0.1 M Na_2SO_4. Reprinted from [73], Copyright (2018), with permission of Elsevier. E (V/SHE) = E (V/Hg/HgO/1 M KOH) + 0.14 V.

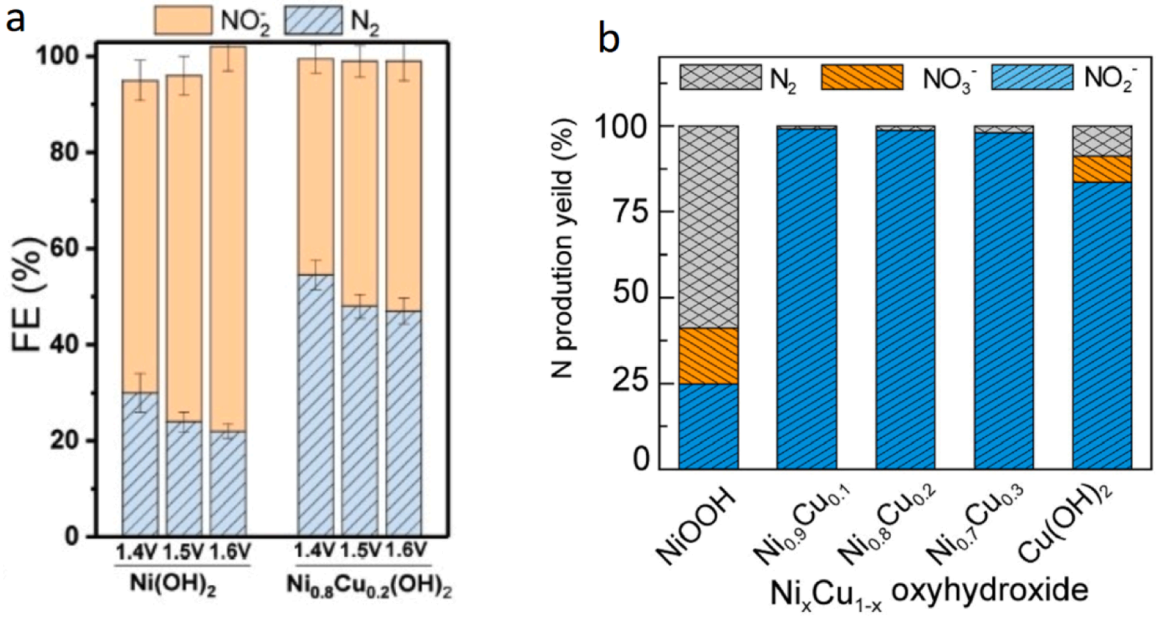

Fig. 6. (a) Faradaic efficiencies (FEs) of the major products of potentiostatic urea electrolysis of 0.33 M urea in 1 M KOH solution on $Ni(OH)_2$ and $Ni_{0.8}Cu_{0.2}(OH)_2$ electrodes at different applied potential *vs.* RHE. (b) Yield ratio of N products during potentiostatic ammonia electrolysis at 1.53 V *vs* RHE in 10^{-3} M NH_3 and 0.1 M KOH solution on Ni_x-Cu_{1-x} oxyhydroxide with different x (x=0–1).
(a) Reprinted from [79], Copyright (2022), with permission from John Wiley and Sons. (b) Reprinted from [59], Copyright (2020), with permission from Elsevier.

tammetry, that nickel-based electrodes performance showed and accelerated decrease with reaction time (Fig. 7A), which was probably due to either the catalyst instability or poisoning. Moreover, electrochemical impedance, Raman and *in-situ* Fourier transform infrared (FTIR) spectroscopies showed modifications at the electrode surface during UOR, wherein most likely the intermediate/products adsorbed and blocked the active sites of the catalyst (Fig. 7B). Therefore, different possible intermediate/products species have been proposed as responsible for the catalyst's deactivation/degradation process, including ^{-}OCN, CO_2/CO_3^{2-}, CO, other N-based species (N_2O, NO_2^- and NO_3^-) and NH_3.

2.4.1. *Effect of cyanate (*$^{-}$*OCN)*

Attenuated total reflection infrared (ATR-IR) spectroscopy [78] confirmed the absence of ^{-}OCN adsorbed on the surface of the NiOOH electrode and its single presence in the diffusion layer during UOR. Furthermore, it is hypothesized that acidic sites present at the NiOOH surface (Lewis acid) could catalyze the hydrolysis of ^{-}OCN into NH_3 and CO_2 [90–92] by following **reaction 2**, which means that ^{-}OCN might not be a stable product under urea electrolysis conditions.

2.4.2. *Effect of* CO_2/CO_3^{2-}

DFT calculations done by Daramola et al. [93] showed that the desorption of CO_2 from the surface of the electrode was the rate-limiting step during UOR. Thus, CO_2 could be considered among the species that are responsible for catalyst deactivation. Forslund et al. [88] reported that CO_2 in a strong alkaline solution reacted with Ni-based perovskite electrodes, to form a new structure, nickel carbonate. As shown in Fig. 8, the peaks associated with oxidation and reduction of Ni species disappeared after purging the solution with CO_2, suggesting the existence

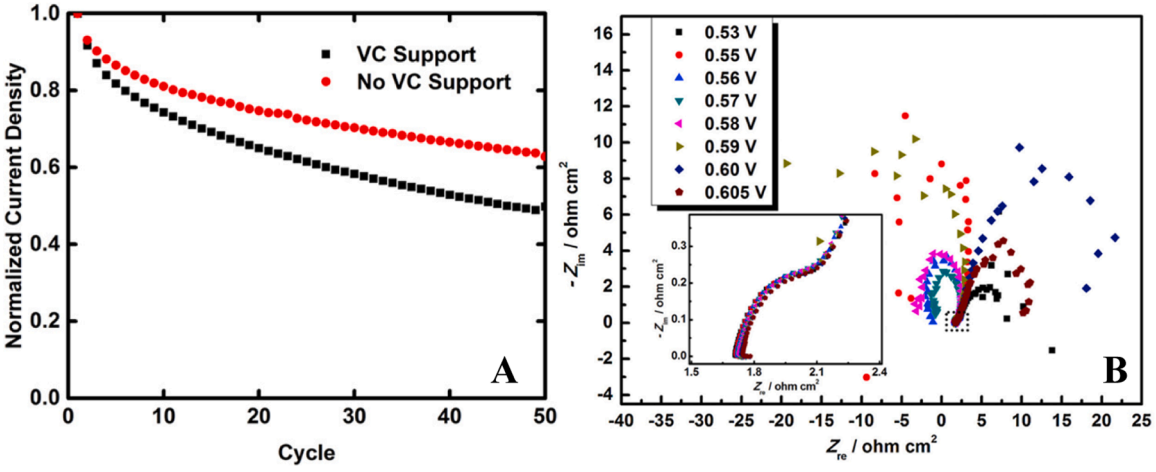

Fig. 7. (A) Plot of normalized peak current densities with repeated voltammetry cycling in 5 M KOH and 0.33 M urea solution, with and without the Vulcan carbon (VC) support for $LaNiO_3$. Copyright (2016) American Chemical Society. (B) Nyquist plots of Ni catalyst in 1 M KOH and 0.1 M urea solution at various polarization potentials vs. Ag/AgCl/Cl-. E (V/SHE) = E (V/Ag/AgCl/3 M KCl) + 0.197 V.
(a) Reprinted with permission from [88]. (b) Reprinted from [89], Copyright (2016), with permission from Elsevier.

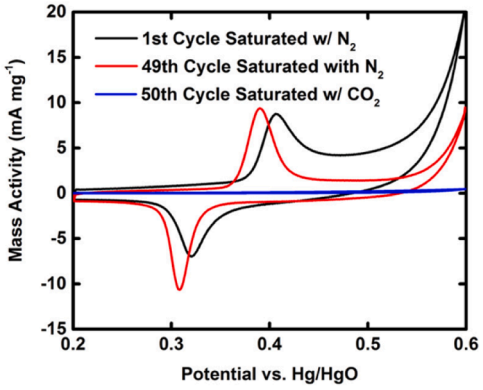

Fig. 8. $LaNiO_3$ supported on Vulcan carbon cycled 49 times in an N_2-saturated solution of 5 M KOH. The 50th cycle was performed in the same electrolyte saturated with CO_2. All cycles were performed with a scan rate of 100 mV s^{-1}. All currents were normalized by the mass of the perovskite drop-cast on the electrode (in mg) to obtain mass activities. Reprinted with permission from [88], Copyright (2016) American Chemical Society. E (V/SHE) = E (V/Hg/HgO/1 M KOH) + 0.14 V.

of a blockage on the electrode surface. However, the authors have not taken into account the strong pH modification of the electrolyte provoked by CO_2 purging. Indeed, the KOH in solution would be partially neutralized by the purged CO_2 into K_2CO_3, leading to a significant decrease of pH, and in return, the oxidation and reduction peaks associated with Ni would shift in potential according to Nernst equation and disappeared from the studied potential window.

Guo et al. [89] have studied UOR by EIS and have concluded that nickel catalyst was poisoned by the adsorption of CO_2 released from UOR and proposed to explore new CO_2-insensitive catalysts. Those authors considered that the presence of a reverse semicircle loop in the Nyquist plot at relevant potentials for urea oxidation between 0.55 V and 0.59 V *vs.* Ag/AgCl/Cl^- (Fig. 7B) could be attributed to an adsorption process on the electrode surface and thus, confirmed the catalyst deactivation by CO_2/CO_3^{2-} from UOR. Interestingly, when the potential reached values higher than 0.59 V *vs.* Ag/AgCl/Cl^-, the Nyquist plot jumped again to a positive loop, probably due to the concurrent OER, which unblocked the electrode surface by releasing gas bubbles. Nevertheless, this conclusion has been recently argued by Akkari et al. [94]. These authors proposed that a reverse semicircle loop observed in the Nyquist plot represented a negative polarization resistance value, regardless of either the presence or absence of any adsorption process. Thus, some controversy regarding the adsorption of CO_2/CO_3^{2-} on Ni-based catalysts during UOR is still in the bibliography. Some other authors previously suggested the precipitated salt K_2CO_3, as responsible for blocking the nickel catalyst surface in air-breathing methanol/O_2 alkaline fuel cells [95].

2.4.3. Effect of CO

Guo et al. [96] suggested, based on EIS data from a different electrocatalytic reaction than UOR [97], that the reverse loop displayed by EIS in the Nyquist plot on the nickel nanowires surface (Fig. 9) could be due to the electrode blockage by CO. Nevertheless, in situ FTIR experiments performed by Wang et al. [78] showed the total absence of evident IR bands associated with CO presence on the surface of Ni-based electrodes during UOR, which made the effect of CO in Ni-based catalyst poisoning very unlikely.

2.4.4. Effect of other N-based species (NH_3, N_2O, NO_2^- and NO_3^-)

UOR on nickel-based catalysts can produce NH_3 as product, as well as over-oxidized N-compounds such as NO_3^-, NO_2^- and N_2O rather than pure N_2, being $NH_3$and NO_2^- the main byproducts detected together with N_2 from urea electrolysis (Table 2). To the best of our knowledge,

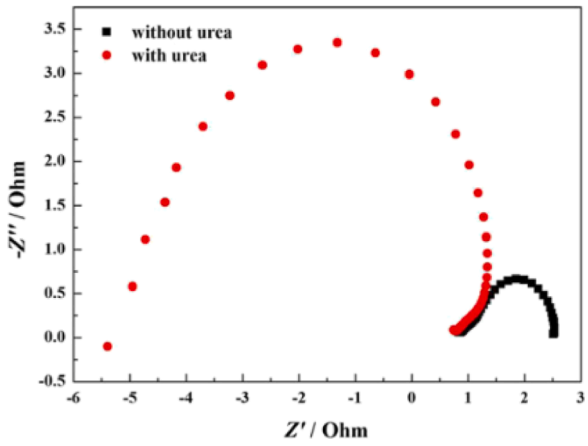

Fig. 9. Nyquist plots of nickel nanowire array electrode at 0.47 V *vs.* Ag/AgCl/Cl^- in 5 M KOH solution in the presence and the absence of 0.33 M urea. Reprinted from [96], Copyright (2016), with permission from Elsevier. E (V/SHE) = E (V/Ag/AgCl/3 M KCl) + 0.197 V.

N_2O and NO_3^- have not been studied yet in the bibliography as potentially responsible for the degradation/deactivation of the catalyst during UOR. Thus, it cannot be ruled out their effect on the catalyst performance. In contrast, the role of NH_3 and NO_2^- have been recently addressed by Akkari et al. [94] by EIS performed at 0.53 V *vs.* Hg/HgO/OH^- (Fig. 10) and these authors concluded that neither NH_3 nor NO_2^- has a substantial impact on the catalytic activity of Ni-based electrodes during UOR.

2.4.5. Overcoming electrocatalyst degradation/deactivation

It has been reported the importance of doping or alloying the Ni catalyst with other metals to improve the current density achieved during UOR and to minimize blockage/deactivation at the electrode surface. For example, some different approaches based on electrocatalyst engineering can be encountered in the bibliography: *(i)* adding nitrogen dopants on Ni [98], which weakens the link strength between CO_2 and Ni, *(ii)* adding a graphene coating on Ni [99], which protects it from passivation and *(iii)* alloying Rh with Ni, which improves the catalyst stability as well [100,101]. Moreover, depending on the

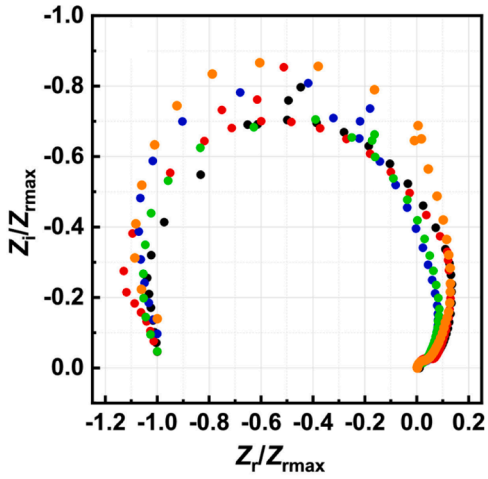

Fig. 10. Nyquist plots corresponding to EIS spectra obtained on NiO/NiOOH NPs at 800 rpm and 0.53 V *vs.* Hg/HgO/OH^-. Solution composition: 5 M NaOH and 0.01 M urea (black plot) and in the presence of 0.01 M CO_3^{2-} (red plot), 0.01 M NO_2^- (blue plot), 0.01 M ^-OCN (green plot), or 0.01 M NH_3 (orange plot) in solution. Reprinted from [94], Copyright (2023), with permission from Elsevier. E (V/SHE) = E (V/Hg/HgO/1 M KOH) + 0.14 V.

operating conditions, the electrocatalyst degradation/deactivation may be variable in extension. For any potential industrial application, it would be necessary to identify the nature of the degradation process in order to propose a well-adapted solution, which improves the service life of the electrocatalyst. In particular, the ability of Ni-based catalysts to regenerate the NiOOH active film consumed during UOR in a fast and reversible way together with recovering/separating competitive electroactive organic molecules present in the urine matrix before performing UOR represent critical key points to overcome the catalyst degradation/deactivation process.

2.5. Thermodynamic considerations for urea and ammonia electro-oxidations

The thermodynamic standard potential (E^o) is one of the primary criteria for assessing the affinity of an electrochemical reaction, since it indicates the minimum theoretical value of the energy required to initiate this reaction. The overpotential (η) of an electrochemical reaction such as the UOR or AOR corresponds to the difference between the applied potential (E_{app}) necessary for reaching a given current and the thermodynamic standard potential. Thus, the overpotential represents a key parameter for evaluating electrocatalyst activity based on reaction efficiency. The presence of an electrocatalyst is crucial in most electrochemical reactions for diminishing the reaction's overpotential and reduce the consumed energy. Reporting accurate E^o values for the UOR and AOR is important to get a proper evaluation of η. Unfortunately, different E^o values have been reported in the bibliography, particularly in the case of UOR. As presented later in the next section, UOR and AOR mechanisms offer complex reaction schemes with multiple possible reaction pathways. Nevertheless, the E^o values found in the literature for both UOR and AOR refer only to the formation of N_2 in a single step, **reactions (3)** and **(6)**, respectively.

Different E^o values for UOR to produce N_2 (**reaction (3)**) in alkaline media have been reported by Boggs et al. [100] (-0.46 V *vs*. SHE) and by Yang et al. [102] (-0.746 V *vs*. SHE), which corresponds to almost 300 mV difference. Guo et al. [89] also reported a value of −0.746 V *vs*. SHE for UOR, despite these authors have considered the generation of CO_3^{2-} in alkaline medium as a byproduct rather than CO_2 (**reaction (3d) in** Table 3). This points out the need of additional investigation in this area to get accurate values of E^o, since, *(i)* as mentioned before, the E^o value is an essential parameter to evaluate the electrochemical reaction affinity against electrocatalyst, *(ii)* the data available in the bibliography [31–35,87,103] show significant dispersion in E^o values, and *(iii)* the production of highly oxidized N-species other than N_2 has been seldom considered in detail. For all those reasons, we have included in Table 3 our own calculated E^o values for both UOR and AOR. All Gibb's free energy values necessary to perform these calculations following Eqs. (1) and (2) were obtained from the bibliography [104].

$$\Delta G^o_{reaction} = \Sigma\nu_{product} \times \Delta G^o_{product} - \Sigma\nu_{reactant} \times \Delta G^o_{reactant} \quad \text{(Eq. 1)}$$

$$E^o = \frac{-\Delta G^o_{reaction}}{nF} \quad \text{(Eq. 2)}$$

Where ΔG^o is the Gibbs free energy (J mol^{-1}), ν the stoichiometric coefficient (dimensionless), E^o the standard potential of the involved reaction (V), n number of electrons transferred (dimensionless), and F the Faraday constant (96485 C mol^{-1}).

Table 3 presents the calculated E^o values for UOR to produce N_2 involving 6 electrons by considering all different possible forms of CO_2 (aqueous (**reaction 3a**), gas (**reaction 3b**), HCO_3^- (**reaction 3c**) and CO_3^{2-} (**reaction 3d**)). This leads to a dispersion in E^o values of 110 mV, being $E^o = -0.85$ V *vs*. SHE the most likely one, because it considers the realistic approach of forming CO_3^{2-} in an alkaline solution. An alternative reaction pathway for UOR recently proposed in the bibliography [79] considers the formation of two different N-species also involving 6 electrons (**reaction 11**). In particular, one of the N atoms contained in urea remains without any change in the oxidation state ($^-$OCN) and the other N atom is oxidized forming NO_2^- ($E^o = -0.43$ V *vs*. SHE). Moreover, the production of highly oxidized N-species (N_2O, NO_2^- and NO_3^-) from UOR is considered as well. Thus, the formation of N_2O involving 8 electrons (**reaction 12**), two NO_2^- involving 12 electrons (**reaction 13**) or two NO_3^- involving 16 electrons (**reaction 14**), exhibit E^o values −0.40, −0.22 and −0.16 V *vs*. SHE, respectively, which are between 450 and 690 mV less negative than the E^o value corresponding to the production of N_2 (**reaction 3d in** Table 3). Some discrepancies appear when comparing these E^o values for **reactions 13** and **14**, with those reported by Li et al. [80], −0.166 and −0.126 V *vs*. SHE, respectively.

Table 3 also presents the calculated E^o values for AOR to produce N_2 (**reaction 6**) and for other highly oxidized N-species such as NO_3^- (**reaction 7**) and NO_2^- (**reaction 10**), being −0.77, −0.12 and −0.16 V *vs*. SHE, respectively. No significant dispersion of the E^o values for AOR is observed when comparing values in Table 3 with previous E^o values reported in the bibliography [71,105]. Both UOR and AOR display, independently of the N-product formed, a significantly more negative E^o value than H_2O electro-oxidation to produce oxygen gas (O_2) (**reaction 15**). This fact should allow producing green H_2 in alkaline solution at the cathode (**reaction 16**) either by combination with UOR at the anode exhibiting an overall cell potential (E^o_{cell}) between +0.02 and −0.67 V (depending on the oxidation pathway) [106,107] or by combination with AOR at the anode exhibiting an E^o_{cell} between −0.06 and −0.71 V. It is important to point out that all those thermodynamic E^o_{cell} values are significantly lower than green H_2 production from H_2O electrolysis (-1.23 V). However, the sluggish kinetics of both UOR and AOR cause high overpotentials, which does not allow to produce H_2 at $E^o_{cell} \leq$ 1.23 V. In particular, NiOOH is one of the few electrocatalytic materials able to efficiently oxidize either urea or NH_3. Nevertheless, it means that the oxidation potential of $Ni(OH)_2$ or NiO to form NiOOH (**reactions 17** and **18**, respectively) must be reached as a prerequisite. For this reason, the E^o value for the formation of NiOOH is also included in Table 3 (0.49 V *vs*. SHE). Then, the production of green H_2 coupled with either UOR or AOR on NiOOH anodes requires an E^o_{cell} of −1.32 V, a bit larger than the one required for H_2O electrolysis. Thus, finding new highly active catalysts for either UOR or AOR is crucial to minimize the overpotential and consequently the cost of the urea/NH_3 effluent treatment, as well as H_2 production.

Table 3
Calculation of thermodynamic standard potentials (E^o) in alkaline media (pH = 14).

Reaction number	Electrochemical Reactions	E°/ [V vs. SHE]
(3a)	$CO(NH_2)_{2(aq)} + 6OH^- \rightleftharpoons N_{2(g)} + 5H_2O_{(l)} + CO_{2(aq)} + 6e^-$	−0.74
(3b)	$CO(NH_2)_{2(aq)} + 6OH^- \rightleftharpoons N_{2(g)} + 5H_2O_{(l)} + CO_{2(g)} + 6e^-$	−0.75
(3c)	$CO(NH_2)_{2(aq)} + 7OH^- \rightleftharpoons N_{2(g)} + + 5H_2O_{(l)} + HCO^-_{3(aq)} + 6e^-$	−0.81
(3d)	$CO(NH_2)_{2(aq)} + 8OH^- \rightleftharpoons N_{2(g)} + 6H_2O_{(l)} + CO^{2-}_{3(aq)} + 6e^-$	−0.85
(11)	$CO(NH_2)_{2(aq)} + 8OH^- \rightleftharpoons {}^-OCN_{(aq)} + 6H_2O_{(l)} + NO^-_{2(aq)} + 6e^-$	−0.43
(12)	$CO(NH_2)_{2(aq)} + 10OH^- \rightleftharpoons N_2O_{(g)} + 7H_2O_{(l)} + CO^{2-}_{3(aq)} + 8e^-$	−0.40
(13)	$CO(NH_2)_{2(aq)} + 16OH^- \rightleftharpoons 2NO^-_{2(aq)} + 10H_2O_{(l)} + CO^{2-}_{3(aq)} + 12e^-$	−0.22
(14)	$CO(NH_2)_{2(aq)} + 20OH^- \rightleftharpoons 2NO^-_{3(aq)} + 12H_2O_{(l)} + CO^{2-}_{3(aq)} + 16e^-$	−0.16
(6)	$2NH_{3(aq)} + 6OH^- \rightleftharpoons N_{2(g)} + 6H_2O_{(l)} + 6e^-$	−0.77
(7)	$NH_{3(aq)} + 9OH^- \rightleftharpoons NO^-_{3(aq)} + 6H_2O_{(l)} + 8e^-$	−0.12
(10)	$NH_{3(aq)} + 7OH^- \rightleftharpoons NO^-_{2(aq)} + 5H_2O_{(l)} + 6e^-$	−0.16
(15)	$4OH^- \rightleftharpoons O_{2(g)} + 2H_2O_{(l)} + 4e^-$	0.40
(16)	$2H_2O_{(l)} + 2e^- \rightleftharpoons H_{2(g)} + 2OH^-$	−0.83
(17)	$Ni(OH)_{2(s)} + OH^- \rightleftharpoons NiOOH_{(s)} + H_2O_{(l)} + e^-$	0.49
(18)	$NiO_{(s)} + OH^- \rightleftharpoons NiOOH_{(s)} + e^-$	0.49

2.6. Electrolysis of urea and ammonia in alkaline medium

As previously mentioned, NiOOH is one of the few electrocatalytic materials able to efficiently oxidize both urea and NH_3. In particular, the use of Ni-based catalysts [31,59,72,73,108,109–115] shows promising results working as anode in alkaline media, since Ni is a non-precious metal, which forms conductive oxides in alkaline conditions [116–118]. Moreover, Ni-based anodes display higher activity for UOR than platinoid-based materials (Pt, Rh, Ru) [100], but their deactivation represents a significant drawback, as previously discussed in Section 2.4. Ni-based anodes also present significant corrosion during AOR due to the complexing activity of NH_3, which provokes the release of $Ni^{2+/3+}$ in solution [72].

Synthetic urea solutions and other urea-containing effluents different than urine have been also studied in alkaline solution in the presence of Cl^- using different anode materials, such as DSA, precious metals (Pt – Ir) and different metal oxides (PbO_2, MnO_2 – RuO_2, PdO – Co_3O_4) supported on Ti [28,119–121]. Nevertheless, this indirect chlorine-mediated oxidation pathway involves the formation of toxic chloramine species, as previously discussed in Section 2.2. Fig. 4 demonstrated that direct AOR is strongly pH-dependent and only proceeds at pH >8 [72]. Thus, a lot of effort has been focused on reaching a complete mechanistic understanding of both UOR and AOR by studying these reactions in Cl^- free alkaline solutions. In the following sections, the most relevant mechanistic features of both reactions on NiOOH electrodes are presented in detail by describing their behavior as a function of reactant mass transfer and electrolyte concentration.

2.6.1. Electrochemical oxidation of urea on NiOOH

Investigations on Ni-based anodes by cyclic voltammetry have demonstrated that NiOOH is the active catalytic material for UOR. Fig. 11 shows the reversible transformation between $Ni(OH)_2$ and NiOOH as a function of the applied potential (dotted red plot). Moreover, Fig. 11 shows the electrocatalytic process of UOR (solid violet plot), which starts as soon as the NiOOH is formed at the electrode surface. Most of the reported studies for UOR on Ni-based catalysts are based on the use of cyclic voltammetry and chronoamperometry [31, 110,122–127], and other techniques such as electrochemical impedance spectroscopy (EIS) are seldom used for studying the UOR mechanism [128,129].

Two main reaction pathways have been described in the literature accounting for UOR on Ni-based catalysts: the direct electron-transfer pathway, where urea is adsorbed onto the NiOOH surface without altering it [89,93,130], and the indirect pathway (Fig. 12), in which the urea is oxidized *via* a chemical reaction with the electrogenerated NiOOH (**reaction (17)** in Table 3), which is chemically reduced to $Ni(OH)_2$ by urea through **reaction (19)**, and subsequently electrochemically regenerated to NiOOH at the applied potential [124,129, 131–136]:

$$6NiOOH_{(s)} + CO(NH_2)_{2,(aq)} + 2OH^- \Leftrightarrow 6Ni(OH)_{2,(s)} + N_{2,(g)} + CO^{2-}_{3,(aq)} \quad (19)$$

In early UOR studies, Botte et al. [131,137] investigated the mechanism of UOR using *in-situ* XRD and time resolved surface enhanced raman spectroscopy (SERS). Results indicated that UOR primarily follows an indirect pathway. This is confirmed by the reduction peak of NiOOH during the reverse scan of CV, where the peak decreases in the presence of urea, likely due to its consumption (reduction) into Ni(II) during UOR. Recent works have shown [94,138,139] that the decrease of UOR performance over time may not only be due to the catalyst deactivation by the accumulation of products/byproducts, but also due to slow catalyst NiOOH regeneration into Ni(II) compound. In particular, Rao et al. [138] investigated the reduction peak of NiOOH during CV, and their results showed that the catalyst is only 60 % regenerated in the presence of UOR. Therefore, a few recent studies have attempted to improve UOR by directing the mechanism toward the direct reaction pathway, where no catalyst regeneration is needed since NiOOH remains intact. For instance, by incorporating Nd^{3+} into the catalyst structure ($NdNiO_3$). However, more research is needed in this area as it could be a promising approach to enhancing UOR performance.

The relevant impact of the ($[NaOH]/[CO(NH_2)_2]$) ratio (R) has been investigated in the bibliography [94,140], which identified R>8 as the optimal condition for UOR according to the stoichiometry in **reaction 3d in** Table 3. Fig. 13 shows the impact of urea concentration and the combined effect of NaOH and urea concentrations on the current density obtained by UOR. This figure shows that the current density achieved with a solution of 0.33 M urea (R=3) after 1600 s of electrolysis at a constant potential (orange plot) is equivalent to that provided by a solution of 0.02 M urea, but with R=50 (black plot). Moreover, increasing from 0.01 to 0.1 M the urea concentration only provides a modest increase in current density of about 10–15 % (black line).

EIS was also used to investigate the two reaction mechanisms for UOR and the deactivation of the catalyst [89,94], which is previously discussed in detail in Section 2.4. *In-situ* X-ray diffraction [137] and *in-situ* Raman spectroscopy [131] have provided evidences about the consumption of NiOOH during UOR, indicating that the indirect pathway mechanism is the most likely one for UOR on NiOOH electrode. In addition, Botte et al. [124] studied the effect of urea concentration by cyclic voltammetry on a Ni anode in 5 M KOH and 0.33 M urea solution [124]. Presented in Fig. 14, these results showed that the cathodic peak, centered at 0.42 V *vs*. $Hg/HgO/OH^-$ and attributed to the electrochemical reduction of NiOOH to $Ni(OH)_2$, decreased in intensity with increasing the concentration of urea in solution. This behavior is associated with a more extensive chemical reduction of NiOOH by UOR in the presence of a higher concentration of urea during the forward scan. Thus, such observations strongly suggest an indirect mechanism pathway for the UOR as initially proposed by Botte et al. [93,100,131].

The kinetics and mechanism of UOR were also examined by cyclic voltammetry under convective conditions using a Ni RDE. Botte et al. [124] investigated the UOR in a 0.33 M urea and 5 M KOH solution on Ni electrode as a function of the rotation rate. The results, presented in the form of a Levich plot (Fig. 15) exhibited a linear relationship between the limiting current density and the square root of the rotation speed at low rotation speeds. In contrast, this plot deviated from linearity as soon as the rotation speed became higher than 500 rpm. This observation suggested the existence of two distinct regimes in the UOR: a diffusion-controlled regime at low rotation speeds, where the mass-transfer of urea from the bulk solution to the electrode surface controls UOR activity and a kinetic-controlled regime at high rotation speeds. More recently, by employing a Ni RDE as well, Hopsort et al. [141] have deeply investigated the impact of electrolyte concentration, urea concentration, and their ratio (Fig. 16) leading to determine the complete set of kinetic parameters for the indirect UOR mechanism and

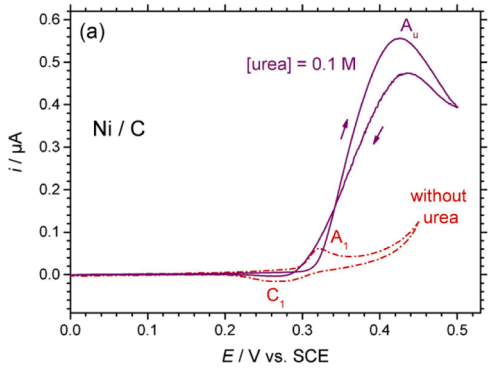

Fig. 11. Voltammograms recorded for Ni/C electrode in 1 M KOH and 0.1 M urea solution, at 10 mV s^{-1}. Reprinted from [101], Copyright (2019), with permission from Elsevier. E (V/SHE) = E (V/SCE 3 M KCl) + 0.24 V.

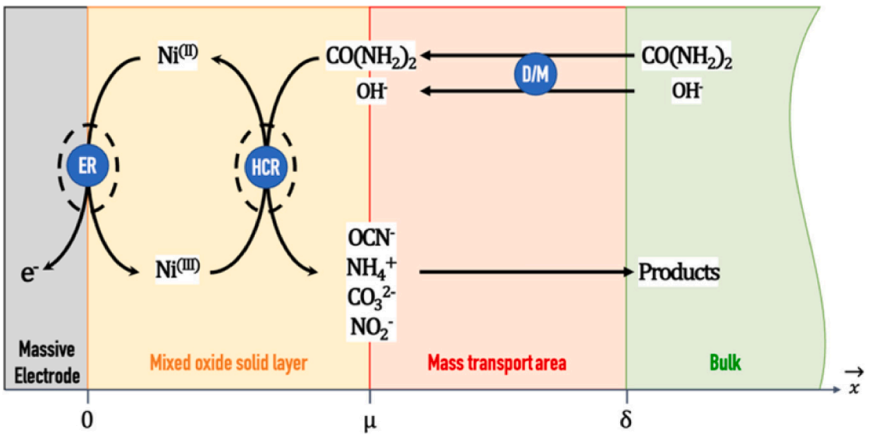

Fig. 12. Schematic representation of the indirect oxidation of urea on NiOOH/$Ni(OH)_2$ operating on the surface of a massive nickel anode in alkaline medium. ER, HCR, and D/M respectively refer to the NiOOH Electrogeneration Reaction, to the Heterogeneous Catalytic Reaction and to the mass transport by Diffusion and Migration. Reprinted from [136], Copyright (2023), with permission from Elsevier.

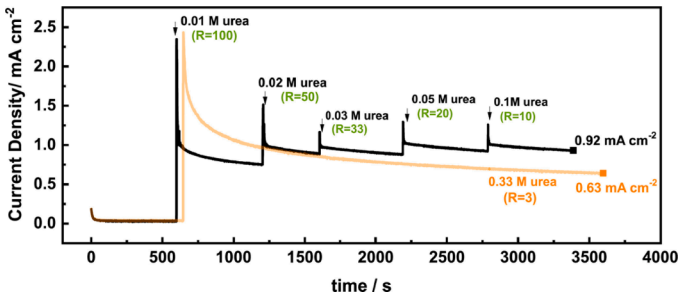

Fig. 13. Chronoamperometry curves during UOR at 0.45 V *vs.* $Hg/HgO/OH^-$ on NiO/NiOOH nano-particles deposited on a rotating disk glassy carbon electrode in 1 M NaOH solution with different ratios $[NaOH]/[CO(NH_2)_2]$ and at a rotation rate of 800 rpm. Each vertical arrow in the black plot indicates the addition of urea in the solution. Reprinted from [94], Copyright (2023), with permission from Elsevier. E (V/SHE) = E (V/Hg/HgO/1 M KOH) + 0.14 V.

to establish a predictive model for potentiostatic electrolysis. Partial orders of 0.3, 1 and 5 were estimated for urea, hydroxide ions and NiOOH, respectively. In conclusion, a large number of investigations have already been devoted to get a deep understanding of the UOR mechanism on NiOOH in alkaline solution [88,94,131,136,140-142]. However, detection of reaction intermediates and other N-products in solution remained a gap in the mechanistic understanding of UOR.

2.6.2. *Electrochemical oxidation of ammonia on NiOOH*

Herein we focus our interest on the mechanism of AOR and its comparison with UOR. In particular, noble metals such as Pt and Pt-alloys [76,77,115,143–145] have been identified as the highest catalytic activity materials for AOR. Moreover, they present high selectivity for the formation of N_2 (see Table 2) as a main product following **reaction 6**. However, their high cost and low abundance have recently shifted the attention of researchers towards Pt deposited on non-noble metals [71], as well as Ni-based catalysts, since similarly to UOR, Ni-based catalysts show high activity towards AOR in alkaline solution [72,73,114,146]. However, nickel oxides are not highly selective for N_2 production and mainly oxygenated nitrogen species such as NO, N_2O, NO_2^- and NO_3^- have been detected as products from AOR electrolysis. In particular, AOR kinetics on $Ni(OH)_2$/NiOOH electrode were investigated by cyclic voltammetry [72]. Initially, two mechanism pathways were proposed: direct and indirect, in the same way as for UOR. Cyclic voltammetry results on AOR (Fig. 17) showed a redox coupled signal (A_1/C_1), which corresponded to the reversible transformation between $Ni(OH)_2$ and

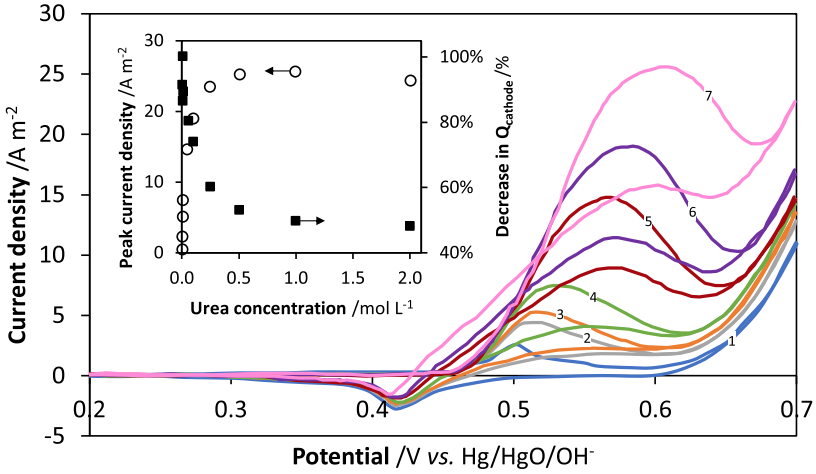

Fig. 14. Cyclic voltammetry on Ni electrode at a scan rate of 10 mV s^{-1} in 1 M KOH solution with variable urea concentration: (1) 0 M, (2) 0.05 M, (3) 0.1 M, (4) 0.2 M, (5) 0.3 M, (6) 0.4 M, and (7) 0.5 M. Insets: Changes in anodic peak current density and the decrease in cathodic charge at various urea concentrations. Adapted from [124], Copyright (2012), with permission from Elsevier. E (V/SHE) = E (V/Hg/HgO/1 M KOH) + 0.14 V.

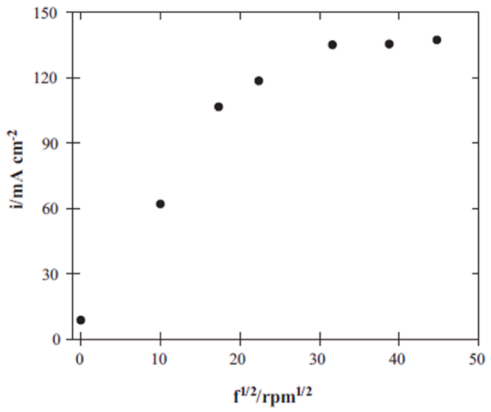

Fig. 15. Levich plot on Ni electrode in 0.33 M urea and 5 M KOH solution using a RDE at various rotation speeds: 100, 300, 500, 1000, and 1500 rpm. Reprinted from [124], Copyright (2012), with permission from Elsevier.

NiOOH as a function of applied potential, as previously described in Fig. 11 (dotted red plot). In addition to this, the appearance of another oxidation peak (A_2) at a more positive potential suggested that ammonia was oxidized at the potential in which NiOOH was dominant at the electrode surface in analogous way as urea (peak A_u in Fig. 11 solid violet plot). Notably, these CVs showed that AOR followed a direct reaction pathway, where chemical NiOOH reduction to $Ni(OH)_2$ was not involved [72]. This is evidenced by the fact that the peak associated with NiOOH reduction (C_1) did not decrease in intensity in the presence of an increasing concentration of ammonia (Fig. 17). This differs from the behavior observed during UOR on the same electrocatalyst NiOOH (Fig. 14b), where the cathodic peak attributed to the electrochemical reduction of NiOOH decreased in intensity with increasing the concentration of urea in solution and this was associated to the indirect reaction pathway of UOR [31,89,131]. In conclusion, AOR could follow on NiOOH electrode an inner sphere reaction mechanism where the reactant is initially adsorbed on the electrode before the electron transfer takes place as described in **reaction 20**.

$$\begin{aligned} &2NiOOH_{(s)} + 2NH_{3,(aq)} + 6OH^- \leftrightarrow 2NiOOH(NH_3)_{ads} + 6OH^- \\ &2NiOOH(NH_3)_{ads} + 6OH^- \leftrightarrow 2NiOOH_{(s)} + N_{2(g)} + 6H_2O_{(l)} + 6e^- \end{aligned} \quad (20)$$

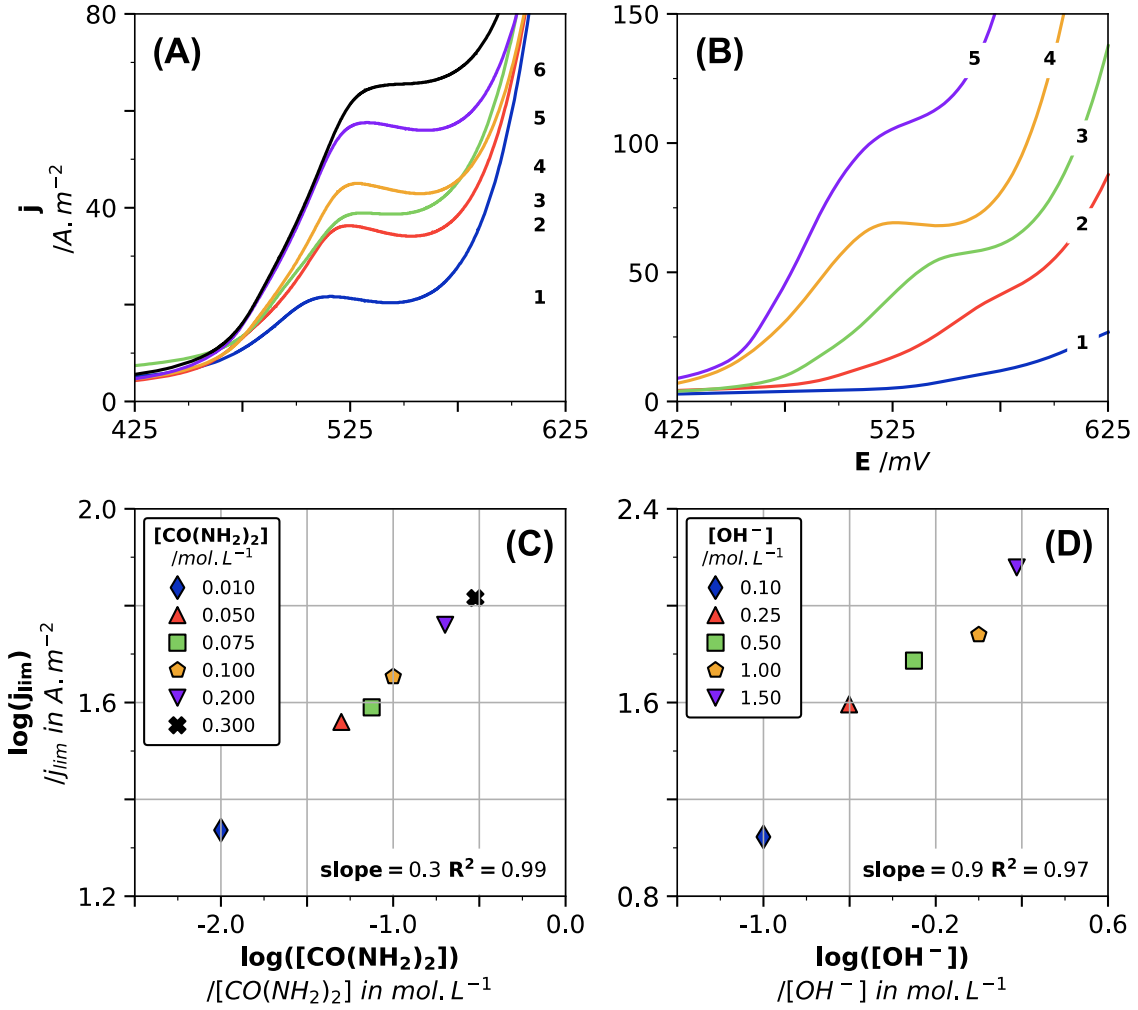

Fig. 16. Kinetic experiments on Ni RDE. Graphs (A)-(B) present linear voltammetry curves obtained at the steady state (0.12 mV s^{-1}) using alkaline solutions of urea, thermoregulated at 298 K. Graph (A) presents the effect of urea concentration in an alkaline solution of KOH (1 M) at 1000 rpm with urea concentrations at 0.01 M (1), 0.05 M (2), 0.075 M (3), 0.1 M (4), 0.2 M (5) and 0.3 M (6). Graph (B) presents the effect of KOH concentration in a solution of urea (0.3 M) at 1000 rpm with hydroxide concentrations at 0.1 M (1), 0.25 M (2), 0.5 M (3), 1 M (4) and 1.5 M (5). The partial reaction orders of urea and hydroxide ions were determined from the curves respectively plotted in figures (D)–(E), deduced from the logarithm plot of the limiting current magnitude as a function of the logarithmic reactant and electrolyte concentration, respectively. Adapted from [141] (CC-BY 4.0 Wiley Periodicals LLC). E (V/SHE) = E (V/Hg/HgO/1 M KOH) + 0.14 V.

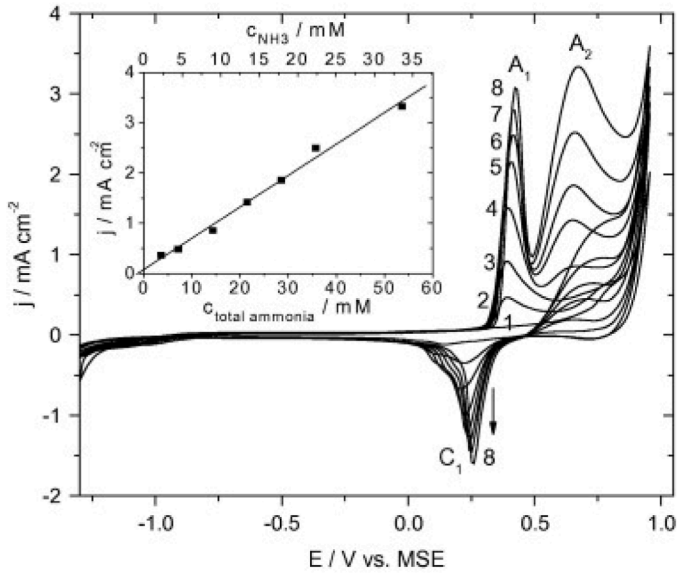

Fig. 17. Cyclic voltammograms of (1) 0 mM, (2) 10 mM, (3) 20 mM, (4) 40 mM, (5) 60 mM, (6) 80 mM, (7) 100 mM, (8) 150 mM NH_4ClO_4 in 1 M $NaClO_4$ + NaOH at pH 9 and 25 °C, recorded on Ni electrode at 50 mV s^{-1}. Reprinted from [72], Copyright (2010), with permission of Elsevier. E (V/SHE) = E (V/Hg/Hg_2SO_4/sat K_2SO_4) + 0.65 V.

Additionally, electrodeposited Pt on Ni RDE was used to study AOR under a controlled hydrodynamic system, and thus, to evaluate the role of ammonia mass transfer in the AOR mechanism [71]. Polarization curves at different rotation speeds and scan rates were collected in 0.1 M KOH and 0.01 M NH_4Cl solution. The corresponding linear relationship between oxidation peak current and the square root of the scan rate ($\upsilon^{1/2}$) reported in Fig. 18 proved AOR as a diffusion-controlled process. However, the peak current density of AOR did not increase linearly with the square root of the rotation speed beyond 1000 rpm (Fig. 18), implying that the reaction was limited by kinetics. Likewise UOR behavior, wherein the oxidation current density showed a diffusion-controlled regime at low rotation speeds (up to 500 rpm), and a kinetic-controlled reaction regime at higher rotation speeds.

Fig. 19 shows the results of bulk electrolysis of ammonia on a Ni electrode in a one-comparment electrochemical cell at pH 11 and 20 mA cm^{-2}. 55 % of the ammonia was degraded after 12 h of electrolysis, 34 % collected as volatile N-products and 11 % as NO_3^-. However, significant electrode corrosion was reported and this provoked the release of Ni ions in solution [72]. Botte et al. [90,99] also suggested that Ni oxides-based electrocatalysts could undergo significant corrosion in the presence of ammonia. Ammonia facilitates Ni corrosion by forming

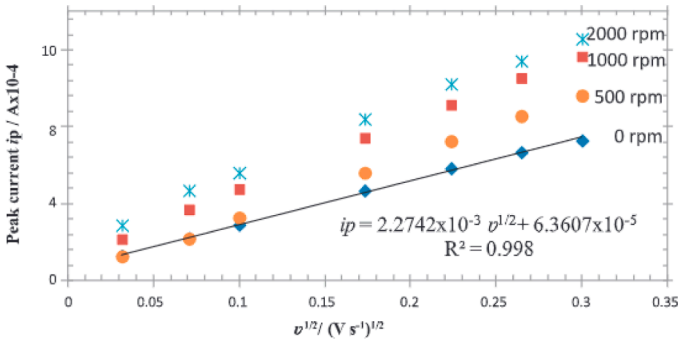

Fig. 18. I_p (peak current) for the AOR *vs.* $\upsilon^{1/2}$ (potential scan rate) at different angular velocities (0, 500, 1000 and 2000 rpm) in a 0.1 M KOH and 0.01 M NH_4Cl solution. Reprinted from [71], Copyright (2013), with permission from Elsevier. E (V/SHE) = E (V/Hg/HgO/1 M KOH) + 0.14 V.

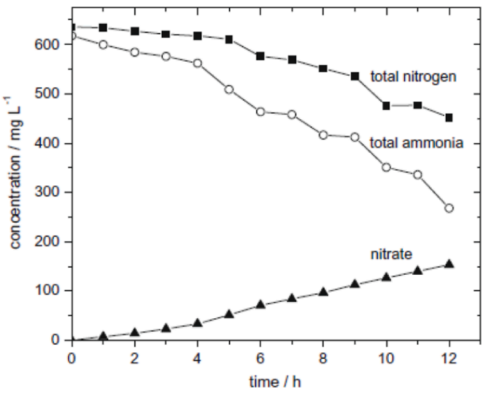

Fig. 19. Reactant and product concentration temporal evolution during the ammonia electrolysis on NiOOH at 20 mA cm^{-2}. Solution composition: 50 mM NH_4ClO_4 + 1 M $NaClO_4$ + NaOH at pH 11. Reprinted from [72], Copyright (2010), with permission of Elsevier. E (V/SHE) = E (V/Hg/Hg_2SO_4/sat K_2SO_4) + 0.65 V.

different Ni-ammonia coordination complexes in the pH range between 8 and 12 [147], as shown in Fig. 20. Moreover, the partial neutralization occurring at the electrode surface by the OH^- consumption during AOR (**reaction 6**) might favor the formation of those Ni-ammonia coordination complexes.

2.7. *Present focus on urea electro-oxidation: selectivity, products detection and reactional pathways*

In recent years, the understanding of the UOR mechanism has been significantly enhanced by discovering new intermediates and products. These findings have shed light on new reaction pathways and broadened the spectrum of potential products [48]. The main focus of current research is to guide the selectivity of UOR towards specific target products. This section aims to analyze the mechanisms of urea over-oxidation that result in NO_x products as well as non-oxidized products like ^-OCN. A comparative review of the documented reaction pathways is provided. Moreover, preliminary methods for influencing UOR selectivity through the purposeful design of catalysts are extensively discussed.

2.7.1. *Reaction product detection and quantification*

Only a few reports in the bibliography have addressed the quantification of the products formed during the UOR electrolysis in alkaline solution, and are mainly focused on the determination of gaseous products by gas chromatography (GC). For instance, G. Botte et al. [100,

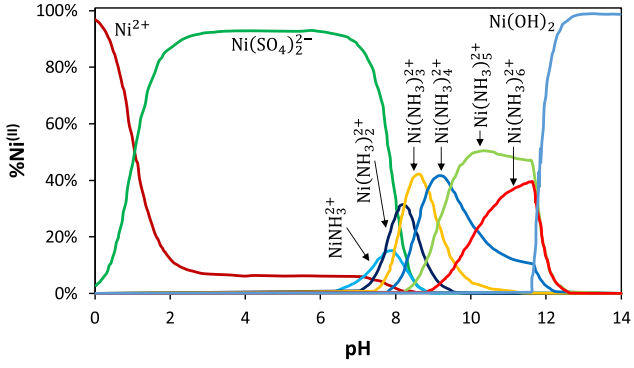

Fig. 20. Predominance distribution–pH diagram for 0.01 M Ni^{2+} and 1.0 M $(NH_4)_2SO_4$ in solution.
(a) Adapted from [147] Copyright (2006), with permission from Elsevier.

148,149] have obtained proportions of N_2, up to 96.1 % (note that this is not a faradaic efficiency, just the percentage in the generated gas at the anode). Recently, Chen et al. [150] were able to demonstrate, using the *in situ* DEMS technique and the $CO(^{15}NH_2)_2$ isotope, that urea was fully oxidized to $^{15}N_2$. They proposed a mechanism of intramolecular coupling of the N −N bond accompanied by a proton-coupled electron transfer, hydration and rearrangement processes. In contrast, Li et al. [80] detected only 15 % of FE for N_2 by GC and showed with ion chromatography (IC) that urea was over-oxidized to nitrite (NO_2^-) with FE of 76 %. Traces of nitrate (NO_3^-) and N_2O were also detected. With GC-MS, these authors also showed that the mechanism for N_2 formation was mainly intramolecular and thus, this pathway was favored when the urea concentration increased. From the mechanistic understanding, a novel strategy was implemented to improve the N_2 production rate based on increasing the residence time of urea within the diffusion layer at the nickel electrode by adding a porous polyaniline (PANI) film, which provides additional hydrogen-bonding network on the electrode surface, and increased the N_2 production by a factor of 2 (FE of 31 %) [80].

The determination of nitrogen-based products in solution is not usually found in the bibliography and only a few examples are reported. Lu and Botte [91] compared the UOR and the thermal decomposition of urea at different KOH concentrations and at 70°C over the NiOOH catalyst. They identified cyanates ($^-$OCN) in the electrode diffusion layer by FTIR, which was later confirmed by ATR-IR spectroscopy [78], and ammonia in the bulk by selective electrodes. They showed that the UOR and the thermal decomposition of urea occurred in parallel at 70°C, with and increasing formation of ammonia with the increase in KOH concentration. In addition, by coupling IC-mass spectroscopy and GC analyses, Hopsort et al. performed recently the complete mass balance of nitrogen and carbon-based products during long-term electrolysis of both urea and urine solutions [86,151] (long-term meaning that almost full conversion of urea/urine was achieved).

To sum up, only NO_3^-, NO_2^-, $^-$OCN and NH_3 species have been identified in solution and N_2 and N_2O together with O_2 in the gas phase (CO_2 remains in aqueous phase as CO_3^{2-}). Table 4 summarizes the catalytic material, solution composition, analytical detection/quantification method and product detected in UOR.

It is worth noting that the products shown in Table 4 are strongly influenced by the potential applied to the cell (in terms of nature and ratio). Indeed, in a conventional EC water electrolysis system, the OER at the anode is coupled with the hydrogen evolution reaction (HER) at the cathode [152]. Thus, replacing the OER with more oxidizable anodic reactions has proven to be a possible alternative to reduce the theoretical cell potential for H_2 production (*e.g.*, methanol [153], ethanol [154], hydrazine [155], etc.), highlighting the benefit of coupling HER and UOR [156,157]. However, UOR electrocatalysts are not able to totally avoid the OER competition for electrons. Notably, this competition between UOR and OER particularly exist at high operating potentials, which arises a significant challenge due to the adsorption of OH^- ions at the electrode surface. While OH^- are necessary for UOR, excessive OH^- adsorption can block urea adsorption and accelerate the competing OER [82,93,131]. This competition not only reduces UOR efficiency, but also over-oxidizes NiOOH [140], degrading electrode stability and thus decreasing further UOR. Gao et al. [82] have explored novel strategies to overcome this challenge, such as incorporating sulfur oxyanions to nickel catalysts (Ni-SO_x). These oxyanions help improve UOR selectivity vs. OER by protecting Ni active sites from excessive OH^- adsorption, thereby enhancing urea adsorption. However, the competition between UOR and OER has not been adequately addressed so far, (with the first study emerging in 2022 [82]) and further studies are required to develop effective strategies that optimize UOR performance by suppressing OER.

Table 4
Various analytical methods reported to monitor the UOR evolution and to perform the corresponding mass and charge balances.

Electrode material	Solution	Detection method / Identified products	Ref.
Ni/Ti electrodeposition	5 M NaOH + 0.33 M urea	GC / Anode: N_2+O_2+H_2 GC / Cathode: H_2	[31]
Ni nanowires electrodeposition	1 M KOH + 0.33 M urea	GC / Anode: N_2+O_2+H_2 GC / Cathode: H_2	[148]
Ni/M (M = Ni, Ti) electrodeposition	Different KOH and urea concentrations	GC / Qualitative results	[43, 90]
$NiCo_2O_4$ nanosheets Hydrothermal method and annealing	5 M KOH + 0.33 M urea	GC / Anode: N_2 + O_2	[149]
$NiMo_2O_4$ nanosheets Hydrothermal method	1 M KOH + 0.33 M urea	GC / Qualitative results: H_2 and N_2 detection	[100]
$\beta - Ni(OH)_2$	1 M KOH + 0.5 M urea	DEMS / 100 % selectivity towards N_2	[150]
Activated NF PANI/ Activated NF	1 M KOH + urea concentrations (0.05 – 3 M)	GC / N_2 - IC / NO_2^-	[80]
Ni plate	1 M KOH + 0.33 M urea	Quantitative evaluation GC / N_2 (H_2 at the cathode) IC / NH_4^+, $^-$OCN, NO_2^-, CO_3^{2-} - MS / Urea	[151]
Ni plate	1 M KOH + human urine (0.23 M urea)	Quantitative evaluation GC / N_2 (H_2 at the cathode) IC / NH_4^+, Na^+, K^+, Mg^{2+}, Ca^{2+}, NO_2^-, $^-$OCN, CO_3^{2-}, $HCOO^-$, Cl^-, SO_4^{2-}, $C_2O_4^{2-}$, PO_4^{3-} - MS / Urea, creatinine	
Ni mesh	1 M KOH + 0.33 M urea	Quantitative evaluation GC / N_2 (H_2 at the cathode) IC / NH_4^+, $^-$OCN, NO_2^-, CO_3^{2-} - MS / Urea	[86]
Ni mesh	1 M KOH + human urine (0.22 M urea)	Quantitative evaluation GC / N_2 (H_2 at the cathode) IC / NH_4^+, $^-$OCN, NO_2^-, CO_3^{2-}, $HCOO^-$, $C_2O_4^{2-}$ - MS / Urea, creatinine	

2.7.2. *Selectivity and new reactional pathways*

Reaction product detection and quantification inform about the selectivity of the reaction, and represent a keystone for building a plausible reaction mechanism. So far, excessive attention has been paid on finding a catalyst for UOR able to lower the overpotential and increase the oxidation rate of urea, setting aside the importance of the selectivity towards N_2 production, which represents the main goal for water denitrification.

Lately, Tatarchuk et al. [79] have proposed two distinct reaction pathways leading to different final products from UOR. Pathway (a) in Fig. 21 is based on the detection of $^-$OCN and NO_x^- (x = 2 or 3) and takes place when one single nitrogen from urea molecule binds to the catalytic active site and proceeds oxidation/over-oxidation into NO_x^-, while the second nitrogen atom and the carbon atom from urea form $^-$OCN, which does not involve any change in the oxidation state of nitrogen. Pathway (b) in Fig. 21, which is based on N_2 and CO_2 detection, takes place when both nitrogen atoms from urea molecule bind on the catalytic active site, undergo oxidation and dimerize to form N_2. However, Li et al. and Tatarchuk et al. [79,80] have considered that $^-$OCN is only formed during urea electrolysis, ruling out the possibility of any contribution from the urea chemical decomposition (**reaction 1**) catalyzed by NiOOH, as previously suggested by Botte et al. [90,91]. Moreover, the

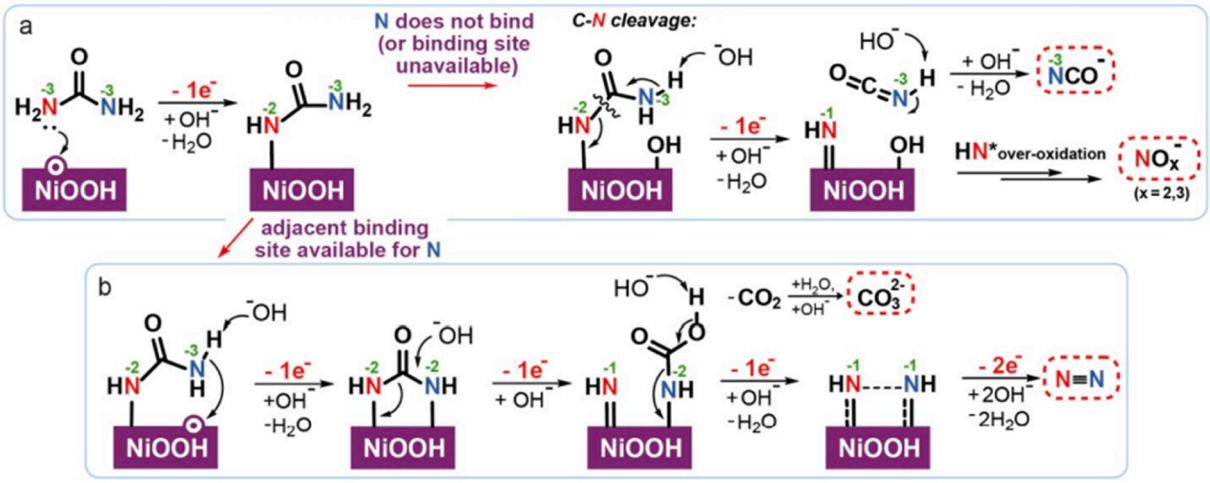

Fig. 21. Proposed reaction pathways for UOR from Tatarchuk et al. Reprinted from [79], Copyright (2022), with permission from John Wiley and Sons.

formation of NH_3 as a product from UOR is not included in the reaction pathways at present. Nevertheless, a significant amount of NH_3 has been quantified during urea electrolysis by Hopsort et al. [136] (44 mol% at the end of the electrolysis with 80 % of urea conversion rate). This shows the importance of investigating more deeply the reaction mechanism of UOR, as well as to find a catalyst that could oxidize both ammonia and urea into N_2. Fig. 22 provides an overview of the 3 different reaction pathways for UOR considered at present in the literature:

- Pathway (1) based on successive electrochemical oxidation reactions of urea, which is only able to justify N_2, NO_2^- and NO_3^- production;
- Pathway (2) based on urea chemical decomposition reaction, which does not involve any electron transfer and only justify the detection of ^-OCN and NH_3;
- Pathway (3) where only one of the two nitrogen atoms present in urea gets oxidized and the other one remains at the same oxidation state, which justify the detection of NO_2^-, NO_3^- and ^-OCN.

Nowadays, one single reaction pathway is not able to justify all detected products. Then, it is probably the simultaneous combination of those 3 reaction pathways shown in Fig. 22 that could explain detecting that large variety of products during UOR.

2.7.3. *Novel electrocatalytic materials for UOR*

Table 5 summarizes the most recent advances in novel electrocatalytic and photoelectrocatalytic materials for UOR by highlighting some examples and mentioning their main advantages. In particular, high surface area anodes based on layered double hydroxides (LDH) such as Cu doped NiFe-LDH are able to overcome some of the previous limitations observed on Ni based materials by enhancing the direct electron transfer mechanism for UOR. Cu doped NiFe-LDH is able to run for more than 300 h at a current density of 10 mA cm^{-2} [158]. In contrast, electrocatalysts containing noble metals such as the Ruthenium-doped nickel oxynitride (Ru@NiON) provide an active electrocatalyst for both reactions (OER and UOR) simultaneously [159].

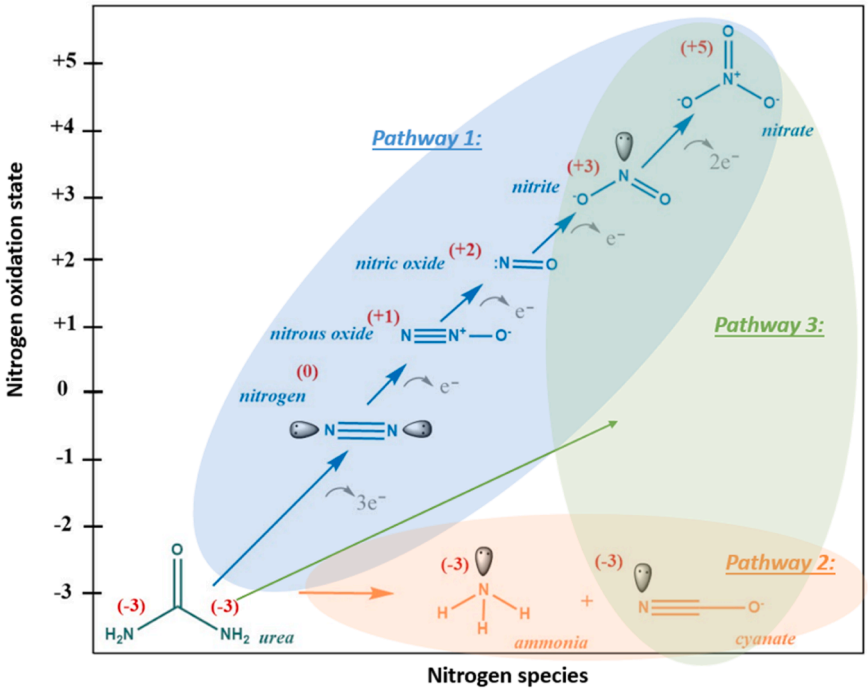

Fig. 22. Reaction pathways during UOR showing all possible N-based products and their oxidation state in each case in red color.

Table 5
a) Electrocatalytic and b) photoelectrocatalytic materials recently used for UOR.

	Examples	*Advantages*	*Ref.*
a) Electrocatalytic materials			[164]
Layered double hydroxide (LDH)	Cu-NiFe-LDH		[158]
	NiMn-LDH	High specific surface area	[165]
	V-NiFe-LDH		[156]
Nitride	Ru@NiON	Dual function UOR and EOR	[159]
Phosphide	Pt-Ni_2P	Highly selective for NO_2^-	[146]
	F-Ni_2P-MoO_2	UOR in natural seawater	[160]
Nickel spinel	$NdNiO_3$	Direct mechanism for UOR	[138]
	$NiCo_2O_4$	High specific surface area	[166]
MOF	Fe_2V-MOF	Works as cathode and anode	[161]
Perovskites	Ni-Zn ABF_3	Well-tuned electronic configuration	[167]
b) Photoelectrocatalytic materials			
Sulfide	Mo-Ni_3S_2	Highly selective for N_2 production	[162]
Nitrogen doped carbon	$Ni(OH)_2$/g-C_3N_4	Formation of heterojunctions	[168]
MOF	Ni-BDT MOF	High specific surface area	[163]

Ni_2P-based anodes for UOR have been already tested in natural seawater, which is considered a promising electrolyte for H_2 production [160]. $NdNiO_3$ is one of the few examples reported where UOR is preferentially driven by the direct electron transfer mechanism [138]. Nanoporous metal-organic frameworks (MOF) have been also successfully tested for UOR achieving an excellent stability during electrolysis over 60 h at current density of 10 mA cm^{-2} [161]. In addition to this, photo-assisted strategies for UOR are concentrating more attention nowadays. In particular, it has been reported that Mo-Ni_3S_2 under AM 1.5 G illumination favors N_2 production from UOR [162]. Moreover, a sulphur-containing organic ligand 1,4-benzenedithiol (BDT) MOF (Ni-BDT MOF) has been recently synthesized on TiO_2 and tested as cocatalyst for urea photoelectrocatalysis under AM 1.5 G illumination [163]. Thus, Table 5 presents a promising new generation of electrode materials displaying an enhanced deactivation resistance during UOR.

3. Photo-assisted urea electro-oxidation: photoanodes and processes

Photoelectrochemical (PEC) processes combine, inside a single apparatus, photo- and electrochemical methods with the aim of generating a photocurrent and highly reactive species either by photon absorption and/or by redox reactions at the surface of the semiconducting electrodes. It is noteworthy that a few photo-assisted processes are already well-developed in the field of wastewater treatment and synthetic chemistry. But it is the case neither for UOR nor AOR from urine. This section explores the domain of UOR from the perspective of PEC processes, focusing on the design and functionality of enhanced photoanodes able to intensify the photocurrent produced and thus the efficiency of the photoassisted electrochemical process. It details some of the most relevant investigations in photoanode materials utilizing semiconductor/nickel-based catalysts for the direct photoelectro-oxidation of urea. Indirect photo-assisted processes rely on active chlorine-mediated radicals to oxidize urea and require semiconductors with large band gaps [39,87], particularly WO_3 [169–174] and TiO_2 [175,176]. As a result, photon absorption occurs only in the UV region of the solar spectrum, which leads to very low solar energy conversion efficiency. For this reason, they are not discussed here; however, the reader can find information on these studies in the references provided above.

Furthermore, this section covers the performance optimization and innovation of different types of reactors for photo-assisted UOR, including batch-stirred, cylindrical continuous-flow, and filter-press continuous-flow reactor designs. A comparative study of these reactors highlighting their significance in advancing sustainable photo-assisted UOR from urine is also addressed because of the lack of any previous study at pilot-scale for the photo-assisted urine valorization.

3.1. Direct photoelectro-oxidation of urea, photoanode materials and design

Most reports in PEC processes are devoted to the design of highly efficient photoanodes (Table 5b), which overcome some of the limitations encountered when scaling up photo-assisted electrochemical processes. Two recently published review articles provide an overview on photo-assisted UOR since its inception in 2012 [39,87]. Table 6 lists some of the most relevant works in the field. In general, the main constraint for choosing the photoanode material and composition is related to the fact that UOR is an anodic process that requires an n-type semiconductor, as well as a catalyst, both of which are susceptible to undergo corrosion processes in contact with the electrolyte. Nevertheless, this limitation depends on the main mechanism followed during the photo-assisted UOR, either the direct photoelectro-oxidative degradation of urea on the surface of a Ni-based catalyst (photo-assisted **reaction (3d) in** Table 3) or the indirect pathway *via* the photogeneration of reactive active chlorine species (**reaction (4)**). Thus, avoiding photoanode corrosion does not require the same semiconductor and/or catalyst material in both cases. In particular, the corrosion issue is more or less limiting depending on the type of architecture present at the photoanode, for example if the semiconductor is protected from the electrolyte by the catalyst (*e.g.*, homogeneous layer covering the semiconductor), or if it is not (*e.g.*, the catalyst is in the form of nanoparticles covering only a part of the semiconductor surface). Moreover, the semiconductor bandgap controls the corrosion extent on the photoanode, since a large bandgap semiconductor (*e.g.*, TiO_2) avoids corrosion, but limits the absorption of the visible part of the solar spectrum and thus the related photocurrent. In contrast, for smaller bandgap semiconductors, the problems of corrosion and band edge position become more relevant. This leads to the use of metal oxides or protective layers and to bias the photoanode potential sufficiently to allow redox reactions to occur. In the following, the main results reported in the bibliography for the photo-assisted UOR are detailed, depending on the semiconductor and catalyst that are chosen. Particular interest is devoted to semiconductors able to afford large solar energy conversion efficiencies.

Semiconductor materials under light irradiation produce pairs of charge carriers that might carry out charge-transfer reactions at the photoelectrode interface. In particular, photooxidative degradation reactions of organic compounds such as urea are conducted by photoinduced holes. Some of the most studied semiconductors for photo-assisted UOR such as TiO_2 [177,185], hematite (Fe_2O_3) [177,178,186] and more recently silicon (Si) [38,181] are listed in Table 6.

TiO_2 is an abundant and stable semiconductor, but it does not absorb photons in the visible spectrum of sunlight and is therefore, not suitable for solar-illuminated PEC processes. In contrast, Fe_2O_3 is often chosen because it offers highly suitable characteristics: it is inexpensive to synthesize, presents low toxicity and is stable at high pH, which is a prerequisite for performing UOR on $Ni(OH)_2$/NiOOH-based catalysts (see Section 2.3). Moreover, Fe_2O_3 is naturally n-type and absorbs light in the visible wavelength range (band gap Eg ~ 2.1 eV), giving a theoretical maximum photocurrent of 12 mA cm^{-2} under AM1.5 solar illumination [187]. Finally, abundant bibliography exists on hydrothermal methods for synthetizing Fe_2O_3 nanowires, which is well-adapted for photoelectrochemistry [188–190]. In 2012, Wang et al. were pioneers in the production of H_2 coupled to photo-assisted UOR from urine under solar illumination [177]. They studied TiO_2 and Fe_2O_3 electrodes on which $Ni(OH)_2$ was deposited by a dip-coating method in alkaline solution (Fig. 23a). These authors showed a significant decrease in the oxidation potential of urea from 1.36 V *vs.* RHE in the dark to 0.91 V *vs.* RHE in the presence of Fe_2O_3 under solar illumination (Fig. 23b). After adding $Ni(OH)_2$ as a catalyst, the onset potential was further shifted by

Table 6
Main results reported in the bibliography on the direct photoelectro-oxidation of urea on semiconductors/Ni-based catalysts.

Electrode	Electrolyte	E_{onset} [a]	Photocurrent density [b]	Ref.
Ni-TiO_2 ($Ni(OH)_2$ deposited by dip-coating)	1 M NaOH + 0.33 M urea	−0.92 V *vs.* Ag/AgCl (0.08 V *vs.* RHE)	3 mA cm^{-2} at 0.2 V *vs.* Ag/AgCl (1.20 V *vs.* RHE)	[177]
	Urine	−0.90 V *vs.* Ag/AgCl (0.10 V *vs.* RHE)	2.7 mA cm^{-2} at 0.2 V *vs.* Ag/AgCl (1.20 V *vs.* RHE)	[177]
Ni-Fe_2O_3	1 M NaOH + 0.33 M urea	−0.5 V *vs.* Ag/AgCl (0.5 V *vs.* RHE)	0.25 mA cm^{-2} at zero-bias 1.75 mA cm^{-2} at 0.2 V *vs.* Ag/AgCl (1.20 V *vs.* RHE)	[177]
Ti-Fe_2O_3 + electrodeposited Ni $(OH)_2$	1 M KOH + 0.1 M urea	0.7 V *vs.* RHE	1.57 mA cm^{-2} at 1.3 V *vs.* RHE	[178]
TiO_2-CdS-$Ni(OH)_2$ (Successive immersion in Ni^{2+} solution then OH^- solution)	1 M NaOH + 0.33 M urea	−1 V *vs.* Ag/AgCl (0 V *vs.* RHE) and activation of Ni at 0.45 V *vs.* Ag/AgCl (0.55 V *vs.* RHE)	~1 mA cm^{-2} at −0.7 V vs. Ag/AgCl (0.3 *vs.* RHE)	[179]
SnO_2@$BiVO_4$/CoPi nanorods	Phosphate buffer solution (pH=7) + 0.33 M urea	0.22 V *vs.* Ag/AgCl (1.22 V *vs.* RHE)	3.44 mA cm^{-2} at 1.23 V *vs.* RHE	[180]
Si + NiFePB	1 M KOH + 0.33 M urea	0.95 V *vs.* RHE	17.0 mA cm^{-2} at 1.23 V *vs.* RHE	[181]
nSi/SiOx/Ni/NiRuPB−150cy	1 M KOH + 0.33 M urea	0.92 V *vs.* RHE	17.5 mA cm^{-2} at 1.23 V *vs.* RHE	[182]
$Ni(OH)_2$/NiFe/n-Si	1 M NaOH + 0.33 M urea	0.83 V *vs.* RHE	37 mA cm^{-2} at 1.23 V *vs.* RHE	[183]
Si + Ni-Mo-O	1 M NaOH + 0.33 M urea	0.87 V *vs.* RHE	17.3 mA cm^{-2} at 1.23 V *vs.* RHE	[38]
WO_3/g-C_3N_4-Ni/CF	1 M KOH + 0.33 M urea	~0.9 V *vs.* RHE	45.3 mA cm^{-2} at 1.23 V *vs.* RHE (100 W halogen lamp)	[184]
Fe_2O_3/$Ni(OH)_2$	1 M NaOH + 0.33 M urea	0.70 V *vs.* RHE	0.53 mA cm^{-2} at 1.23 V *vs.* RHE (1 sun)	[37]

[a] E (V/SHE) = E (V/Hg/HgO/1 M KOH) + 0.14 V and E (V/SHE) = E (V/Ag/AgCl/3 M KCl) + 0.197 V. E (V/RHE) = E (V/Ag/AgCl/3 M KCl) + 0.197 V + 0.059 pH

[b] calculated in all cases with respect to the geometrical area of the photoelectrode under illumination at AM 1.5 G, unless otherwise specified.

−400 mV (0.51 V *vs.* RHE) and the photocurrent substantially increases to ~1.75 mA cm^{-2} at 1.23 V *vs.* RHE (0.23 V *vs.* Ag/AgCl/Cl^-). They also showed voltammograms obtained in urine similar to those obtained in urea solutions.

Xu et al. [178] obtained titanium-doped hematite (Ti-Fe_2O_3) nanowires by hydrothermal synthesis, which were decorated with $Ni(OH)_2$ by cathodic electrodeposition from an aqueous $Ni(NO_3)_2$ solution. They studied the influence of the electrodeposition time (Fig. 24a – d) on the photoelectrochemical performances (Fig. 24e) and showed that the presence of the catalyst (optimized in thickness, a few nanometers) induced a shift of ~ −100 mV in the voltammograms, with an onset potential of UOR at 0.7 V *vs.* RHE under illumination compared to 1.35 V *vs.* RHE for UOR (without photo-assistance), representing a gain of 0.65 V. Accordingly, the photocurrent (at 1.3 V *vs.* RHE) increased from ~0.3 mA cm^{-2} (Ti-Fe_2O_3 alone) to ~1.6 mA cm^{-2} when adding Ni $(OH)_2$.

More recently, Gan et al. [186] measured a photocurrent of 5 mA cm^{-2} in a urea solution (1 M NaOH + 0.33 M urea) and 7.5 mA cm^{-2} in human urine (mixed with an unspecified volume of 1 M NaOH) (Fig. 25a), using arrays of Co-doped Fe_2O_3 nanowires (Fig. 25b) deposited on flexible support and functionalized with Au nanoparticles (Fig. 25c). $Ni(OH)_2$ was deposited by a dip-coating method. Au and Ni $(OH)_2$ could eventually act as plasmonic nanostructures. Interestingly, the alkaline urine samples generated a higher photocurrent than the urea samples, which was attributed by the authors to the presence of other metabolites present together with urea in the urine solution. A photocurrent density of 0.68 mA cm^{-2} was measured in urine solution at 1 V *vs.* RHE. Furthermore, this photoanode gave a stable photocurrent in urine for at least 400 min, as well as continuous H_2 evolution at the Pt counter electrode under low polarization (1.23 V *vs.* RHE).

Rebiai et al. investigated the performances of FTO/Ti-Fe_2O_3 photoelectrodes decorated with sputtered Ni or photoelectrodeposition of NiOOH for solar photo-assisted UOR [37]. The Fe_2O_3 was synthesized in the form of nanorod arrays (hydrothermal route), as shown in Fig. 26a. Two types of Ni coating were tested, sputtered Ni^0 (Fig. 26b), and anodic photoelectrodeposition of NiOOH from a Ni^{2+} solution (Fig. 26c).

Fig. 27 shows voltammograms of Ti-Fe_2O_3 samples before and after NiOOH photoelectrodeposition in NaOH (a) and NaOH + urea (b) solutions. After deposition of NiOOH, the reversible $Ni(OH)_2$/NiOOH peaks appeared centered at 0.90 V *vs.* RHE under solar illumination (a). This potential was much lower than that for a conventional Ni electrode (1.40 V *vs.* RHE), *i.e.,* it corresponded to a gain in potential of 0.5 V. In NaOH + urea solution under solar illumination, the photocurrent started from the $Ni(OH)_2$ oxidation peak (0.7 V *vs.* RHE) and reached 0.53 mA cm^{-2} at 1.23 V *vs.* RHE.

Photoelectrolysis on Ti-Fe_2O_3/NiOOH gave faradaic efficiencies of 10–18 % and 9–35 % for N_2 and O_2 formation, respectively. A significant and unexpected NO_2^- production (~65 %) was detected suggesting an alternative reaction pathway during UOR (**reactions (11)** and/or **(13)**). In the end, photo-assisted UOR accounted for ~ 80 % of the total circulated charge. These authors pointed out that photoelectrocatalytic removal of nitrogen from urea solutions was demonstrated, but significant progress is still needed in photo-assisted UOR to improve its selectivity towards N_2 production and its overall photovoltaic conversion efficiency.

The use of Si photoanodes for the photo-assisted UOR is very recent and represents an alternative to Fe_2O_3 photoanodes. Loget et al. in 2019 [181] published the first article following this approach, which was followed by several others from the same group [38,182,191]. To the best of our knowledge, only one additional work has been reported by Lee et al. on silicon-based electrodes [192]. Loget et al. have investigated metal-insulator-semiconductor (MIS) junctions in PEC cells to produce solar fuels [38,181]. Homogeneous (n)c-Si/SiOx/Ni junctions were first developed by sputtering a compact Ni layer of 17–25 nm thickness onto chemically oxidized (n)c-Si (1.5 nm). These electrodes were then modified with a Prussian blue derivative (NiFePB) by electrochemical oxidation of the Ni layer in the presence of $Fe(CN)_6^{3-}$ at pH 2.5. Ni^0 was converted to soluble Ni^{2+} during successive anodic cycles, which together with $Fe(CN)_6^{3-}$ forms a NiFePB coating on the surface. The thickness of this layer was adjusted with the number of cycles, so that the initial Ni layer was progressively dissolved during the cycling. This electrodissolution corresponded to the decomposition of NiFePB into $Ni(OH)_2$ and the release of Fe hydroxides in solution. The optical transmission increased from 37 % to 75 % (150 cycles) minimizing the loss of photons due to the reflection on Ni. Electrodissolution resulted in inhomogeneous MIS junctions with high potential barriers, but it also had the effect of increasing the surface density of catalytically active

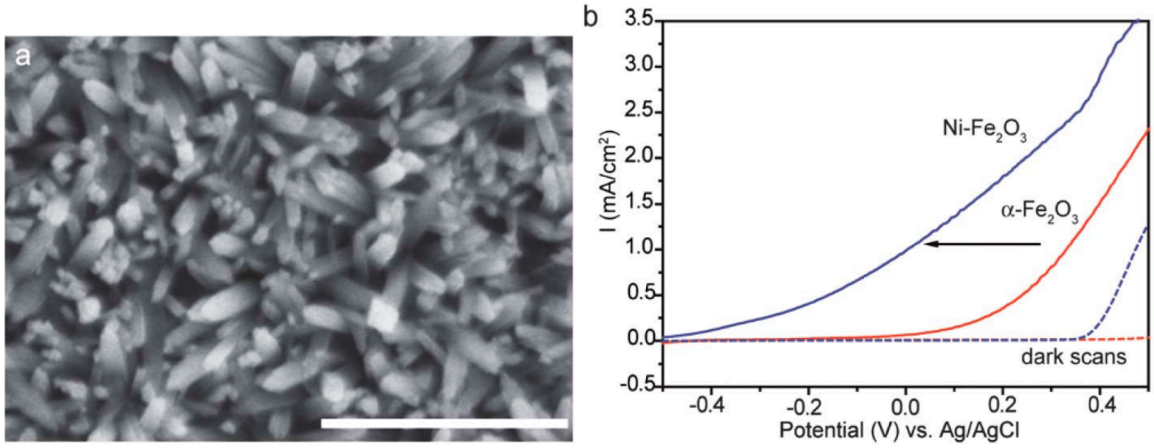

Fig. 23. (a) SEM image of an array of α-Fe_2O_3 nanowires on FTO; scale bar: 2 μm. (b) Linear scanning voltammograms (LSV) of Ni-Fe_2O_3 and α-Fe_2O_3 in urea solution recorded in the dark (dotted lines) and under AM1.5 G illumination. Used with permission of Royal Society of Chemistry, from [177]; permission conveyed through Copyright Clearance Center, Inc. E (V/SHE) = E (V/Ag/AgCl/sat KCl) + 0.197 V and E (V/RHE) = E (V/Ag/AgCl/sat KCl) + 0.197 + 0.059 * pH.

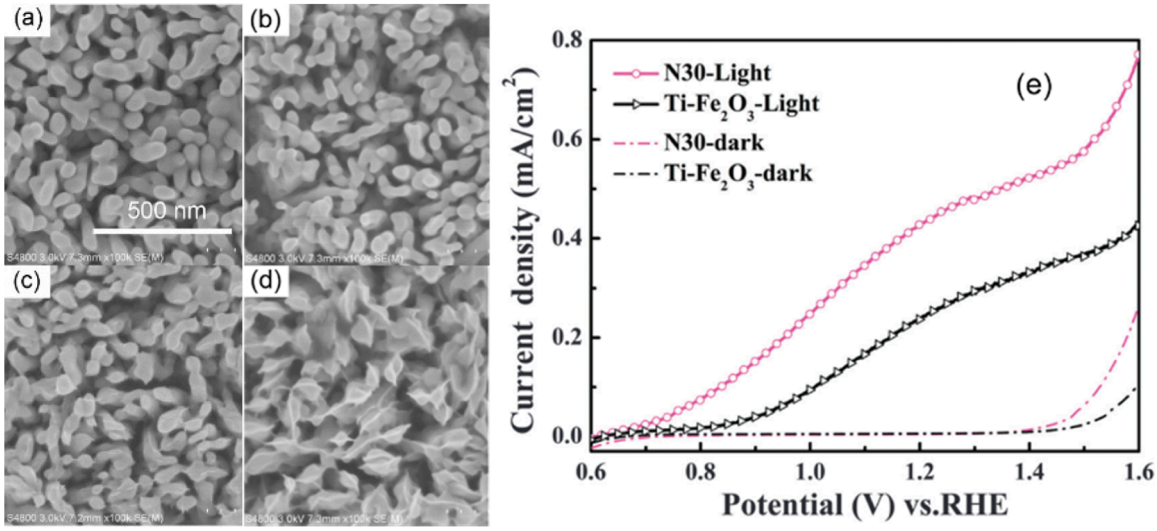

Fig. 24. Plan view SEM images of (a) Ti-Fe_2O_3, plus $Ni(OH)_2$ electrodeposited for a time of (b) 120, (c) 300 and (d) 600 s. (e) Line scan voltammograms for Ti-Fe_2O_3 and Ti-Fe_2O_3/$Ni(OH)_2$ (30 s deposition) in the dark (dashed lines) and under illumination (line + symbols). NaOH 1 M with 0.1 M urea. Scan rate: 10 mV s^{-1}. Illumination: 100 mW cm^{-2}. Reprinted from [178]; Copyright (2015), with permission from Elsevier.

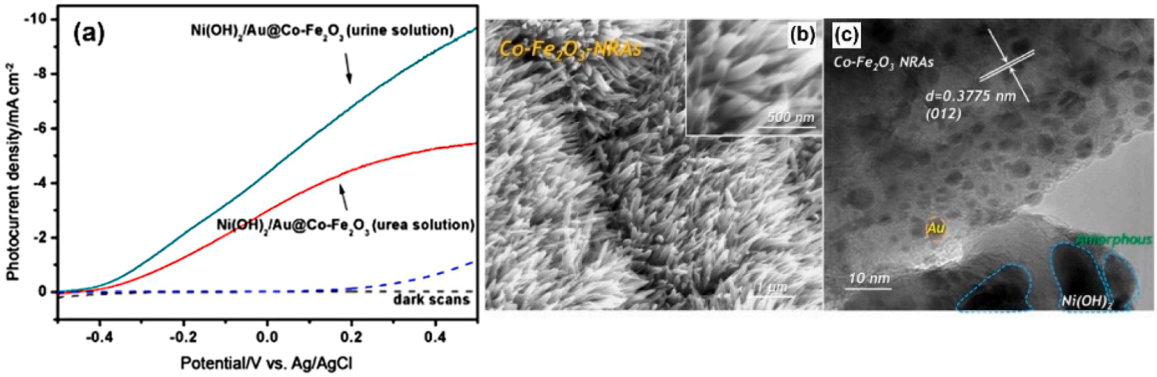

Fig. 25. (a) Line-scan voltammograms of a $Ni(OH)_2$/Au@Co-Fe_2O_3 photoanode in urea solution and human urine solution in the dark (dashed lines) and under AM1.5 G illumination (100 mW cm^{-2}) (solid lines). (b) SEM and (c) TEM images of a $Ni(OH)_2$/Au@Co-Fe_2O_3 photoanode. Reprinted from [186]; Copyright (2019), with permission from Springer Nature. E (V/SHE) = E (V/Ag/AgCl/sat KCl) + 0.197 V.

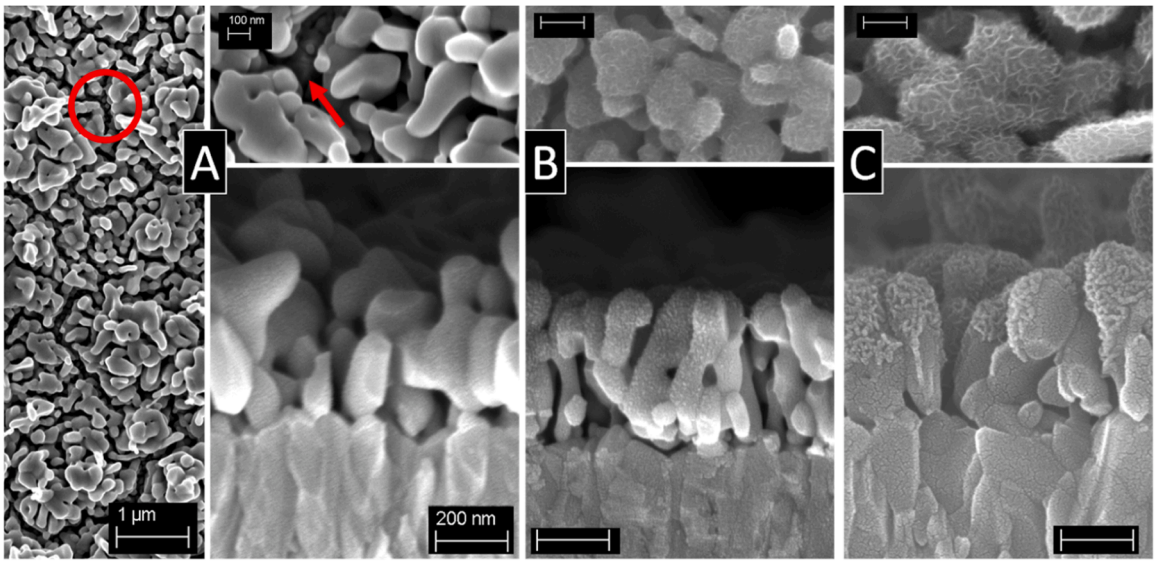

Fig. 26. SEM plane view (higher part) and cross-section (lower part) images of Ti-Fe_2O_3 samples (a) before and (b) after deposition of 2 nm of Ni by sputtering or (c) after NiOOH PEC deposition at 17.5 mC cm^{-2}. The red circle and arrow in (a) indicate areas where the FTO substrate was not covered by hematite. Scale bars: 100 and 200 nm for plan view and cross-section images, respectively. Reprinted from [37]; Copyright (2023), with permission of Elsevier.

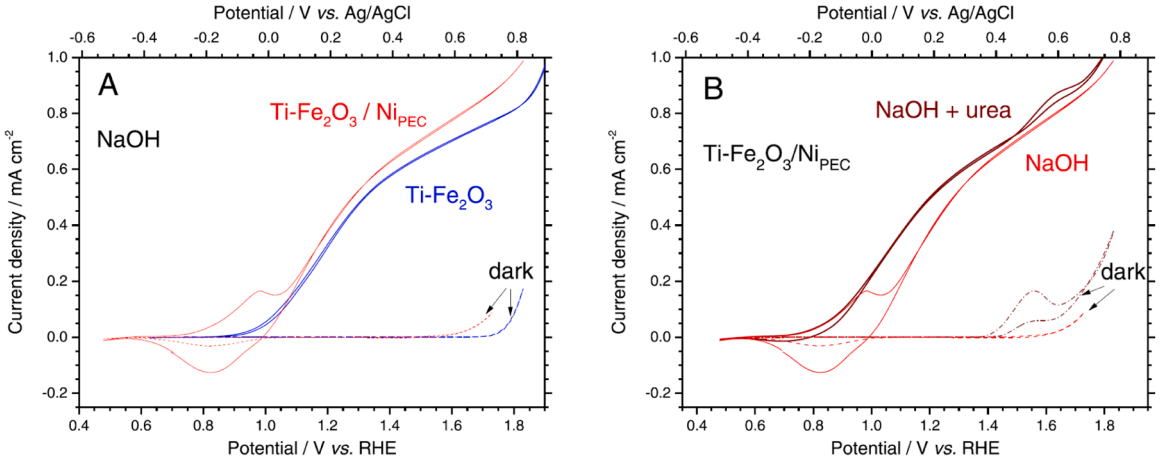

Fig. 27. Voltammetry in the dark and under illumination of (A) FTO/Ti-Fe_2O_3 in NaOH, before and after PEC deposition of NiOOH (8.75 mC cm^{-2}); (B) Ti-Fe_2O_3/Ni_{PEC} in NaOH, with or without urea. [NaOH] = 1 M; [urea] = 0.33 M. Scan rate: 10 mV s^{-1}. Illumination: AM1.5 G, 1000 W m^{-2}. Reprinted from [37]; Copyright (2023), with permission of Elsevier.

nickel sites.

Fig. 28 summarizes the results obtained with this type of electrode. Fig. 28a shows the CVs recorded on n-Si/SiOx/Ni/Ni(OH)$_2$-75cy (75 cycles of NiFePB dissolution) in KOH in the absence and presence of urea. The current densities, which were very low in the dark (<1.5 mA cm^{-2}), reached 20.6 mA cm^{-2} under illumination (AM1.5 G), showing that photogenerated holes were well collected at the interface for both UOR and OER (band diagram in Fig. 28b). There was a gain in electrical energy for both reactions when using illuminated (n)c-Si (red CVs) instead of a similar non-photo-active p^+-Si based electrode (blue CVs) which was related to a potential shift of −0.28 V at 10 mA cm^{-2}. In addition to this gain, the UOR further shifted negatively (0.19 V) compared to the voltammograms relative to the OER. The overall thermodynamic gain was thus 0.47 V on n-Si/SiO_x/Ni/Ni(OH)$_2$-75cy in the presence of urea. According to the authors, this clearly demonstrated the importance of urea for energy saving in photoelectrochemical H_2 production.

Dabboussi et al. reported the use of amorphous Ni-Mo-O (NMO) layers on (n)c-Si/SiOx/Ni/NMO junctions as photoanodes for UOR [38]. The junction was prepared in the same way with a SiO_x tunnel layer (1.3–2 nm) and a Ni layer of 17 nm (sputtering) to obtain n-Si/SiOx/Ni. This substrate was modified using a hydrothermal method in the presence of a solution of nickel nitrate and sodium molybdate, followed by annealing under Ar for 6 h, to form a porous and relatively homogeneous coating (amorphous Ni-Mo-O with a Ni/Mo ratio of 3 and an optimum thickness of ~ 80 nm) as shown in Fig. 29a – b. The voltammograms of (n)c-Si/SiO_x/NMO (purple, Ni-free) in Fig. 29c show an E_{onset} of 1.41 V *vs.* RHE (at 1 mA cm^{-2}) and a sharp decrease upon cycling due to photocorrosion. Therefore, a Ni layer was necessary to prevent photoanode deactivation. Conversely, photoanodes with a Ni thin film, but without NMO ((n)c-Si/SiO_x/Ni, blue CV) had a low E_{onset} of 0.91 V *vs.* RHE, attesting to a definite activity for UOR, but *j* decreased sharply after 1.23 V *vs.* RHE, due to the deactivation of accessible catalytic sites. At more positive potentials than the UOR wave, the current density increased again due to the OER.

Photoanodes comprising Ni and NMO (red CV in Fig. 29c) showed a lower E_{onset} of 0.87 V *vs.* RHE, a high fill factor due to high UOR kinetics, and no sign of urea oxidation current decay. A non-photoactive p^{++}-Si/

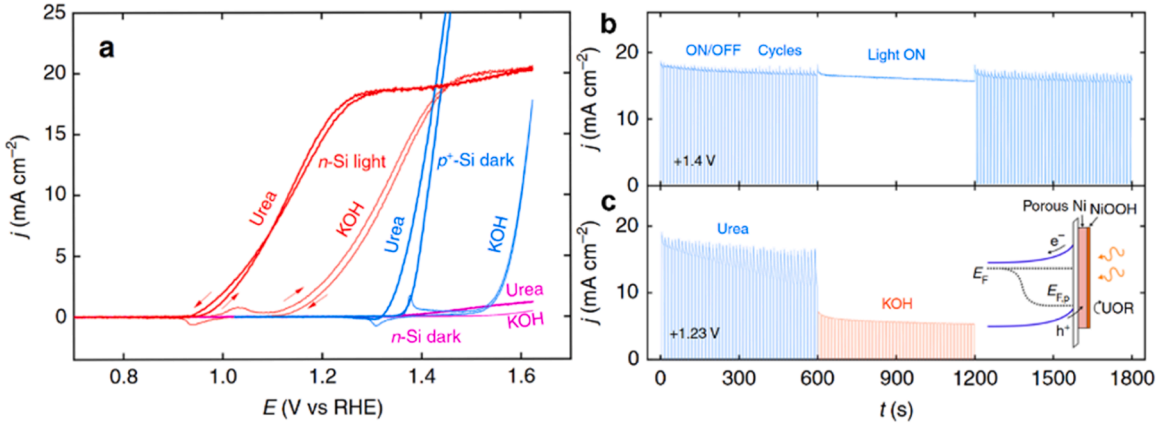

Fig. 28. Photoelectrocatalysis on (n)c-Si/SiO_x/Ni/$Ni(OH)_2$ in 1 M KOH solution in the absence or the presence of 0.33 M urea. (a) CVs of p^+-Si/SiOx/Ni/$Ni(OH)_2$-75cy in the dark (blue), n Si/SiO_x/Ni/$Ni(OH)_2$-75cy in the dark (pink) and under illumination (red); (b, c) Plots of *j vs. t* for photo-assisted UOR on (n)c-Si/ SiO_x/Ni/$Ni(OH)_2$-75cy recorded at (b) 1.40 V and (c) 1.23 V *vs.* RHE; under intermittent/continuous illumination in urea and KOH solution. In (c), the electrolyte becomes KOH at 600 s. Insert: band diagram of an operating n-Si/SiO_x/Ni/NiOOH photoanode at 10 mV s^{-1}; illumination: AM1.5 G. Reprinted from [193]; Copyright (2019), with permission of Springer Nature.

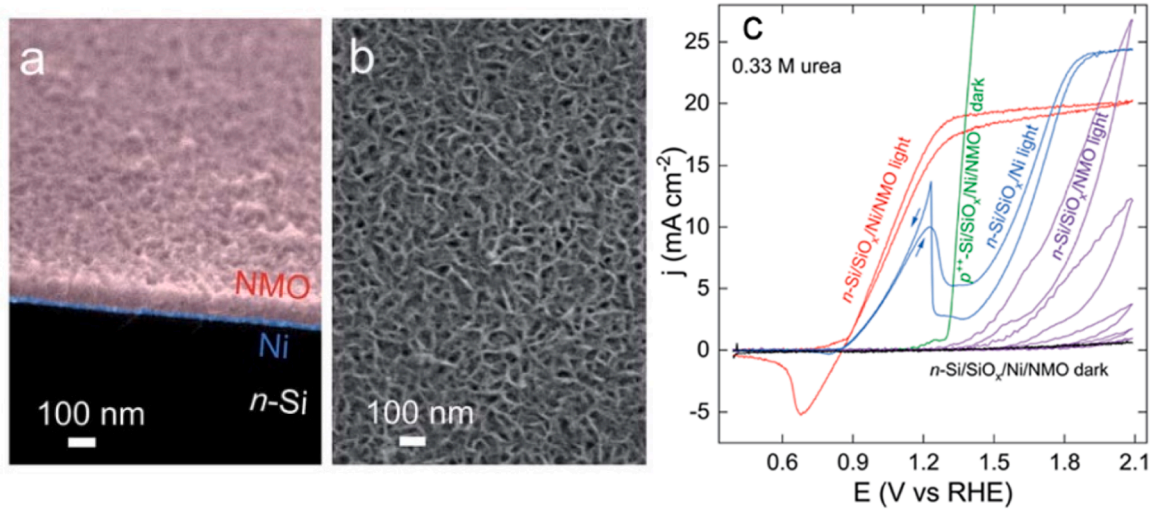

Fig. 29. (a) Tilted SEM cross-section color image of an (n)c-Si/SiO_x/Ni/NMO surface; (b) Top view SEM image of an (n)c-Si/SiO_x/Ni/NMO surface. (c) Voltammograms recorded in 1 M KOH + 0.33 M urea in the dark on (n)c-Si/SiO_x/Ni/NMO (black curve) and (p^{++})-Si/SiO_x/Ni/NMO (green curve) and under illumination on (n)c-Si/SiO_x/NMO (purple curve, 5 consecutive cycles), n-Si/SiOx/Ni (blue curve), and (n)c-Si/SiOx/Ni/NMO (red curve). Scanning speed 100 mVs^{-1}, solar illumination (100 $mWcm^{-2}$, AM 1.5 G). Reprinted from [194]; Copyright (2013), with permission of Royal Society of Chemistry.

SiO_x/Ni/NMO anode was also used in the dark in the same electrolyte (green CV in Fig. 29c). The E_{onset} difference between this anode and the n-Si/SiOx/Ni/NMO photoanode (photopotential) was 400 mV. These authors suggested that there was a conversion of NMO into an opaque NiOOH-rich catalytic film. Indeed, EDS and XPS analyses revealed a considerable leaching of Mo during electrolysis (no longer detectable after 15 hours). Mo thus played the role of a structuring agent in NMO, whose dissolution increased the surface density of the NiOOH active sites (like Fe in the NiFePB layers). The authors emphasized the advantage of photo-assisted UOR, which allowed a considerable increase of current density at a low overpotential. For example, at the standard O_2/H_2O potential (1.23 V *vs.* RHE), the current density was 17.3 mA cm^{-2} *vs.* 5.4 mA cm^{-2} without UOR. In summary, this type of electrode was characterized by a photopotential of 0.40 V, a wave onset at 0.9 V *vs.* RHE, an activity of several hours, and a FE of 85 % for urea abatement.

3.2. *From photoelectrochemical dialysis and organics degradation to photo-assisted urine valorization at large scale*

As mentioned in Section 3.1, over the last decade, researches on PEC methods were mainly focused on design, elaboration and characterization of photo-electrodes, photoanodes being particularly developed [195]. Most of these works deal with pollutant removal (degradation of organics or other refractory compounds in wastewater) and with the production of H_2 by water splitting [47,196,197]. In addition, some studies are devoted to treat wastewater effluents from medical facilities by the degradation and/or monitoring of organic molecules by PEC methods; one can cite for example the chemical oxygen demand (COD) analyzers, the functional transducers for DNA sensors or specific biomolecular sensors [84,198]. Carbon dioxide reduction using photocathodes [199,200], and more generally the valorization to hydrocarbon fuels (such as methanol, formic or acetic acids…) are other applications for PEC methods [201]. Those studies are devoted to the design of enhanced photo-electrode materials with the aim of intensifying the conversion of the photon energy to a photocurrent and thus of efficiently

photo-assisting the electrochemical process. The contribution of the photocurrent is then generally quantified by comparing the performance of electrolysis under an applied potential (by an external device) with and without illumination.

However, only little attention has been paid on the design, optimization and operation of the photoelectrochemical reactors (PECR) as a way to increase the overall performance, especially at large scale. Generally, it is claimed that the limitations encountered when scaling up photo-assisted electrochemical processes mainly come from the photoelectrode efficiency, unaware of other possible limitations (transport phenomena, light absorption, etc.). Wang et al. [195] reported one of the seldom studies discussing different PECR alternatives from a chemical engineering point of view. In particular, these authors presented the strategies enabling to enhance the performances of TiO_2-based PECR (cell design, photoelectrode morphology, bandgap engineering, light absorption or mass transfer). As a low-cost material, TiO_2 photoanodes are considered by these authors as promising systems for pollution degradation, fuel generation processes or water splitting, as well as PEC sensing, and this despite the poor light absorption of TiO_2 in the solar spectrum.

As deeply discussed later, PECR reported in the bibliography, often described briefly [195,202], exhibit various shapes and configurations (*e.g.*, simple cubic or cylindrical open vessels, closed vessels, H-type cells, sandwich assembly, and some other more complex cells). Note that some works also deal with the modelling and simulation of the PECR, such as Kelsall et al. applied to the H_2 generation by water splitting [203–205]. However at the whole, it is evidenced from the state-of-art that there is a lack of experimental and theoretical chemical engineering studies so as to:

(i) optimize the design of the PECR, in particular for a) minimizing the inhomogeneities in spatial distributions of potentials and current densities, and b) optimizing the overpotential of HER;
(ii) optimize and increase the photon energy conversion efficiencies (direct photochemical treatment or additional photocurrent added to an external bias, or even external voltage lowering caused by the illumination);
(iii) achieve the industrial transfer of large-scale PECR.

Concerning UOR and AOR applications (either from urea or urine), the related bibliography mainly focuses on the characterization of photoanodes and/or on investigations on the mechanism [32,206–208] (see Sections 2.7.2 and 3.1). To the best of the authors' knowledge and as suggested in the recent review of Wang et al. [35], neither studies on the design and operation of the UOR (at the pilot or at the industrial scale), nor on the optimization of the cell design and geometry still exist.

Consequently, the following sections propose a synopsis of the studies focusing on the performance optimization on reactor's design and geometry encountered for photo-assisted electrochemical reactions. Because of the lack of studies performed at pilot-scale for the photo-assisted urine valorization, this synopsis has been voluntarily extended to other applications exhibiting as a common feature the generation of H_2. This includes pollution removal, water splitting, or even biological solution purification. The present synopsis has been built by considering the following criteria: monitoring mass and energy balances *vs* conversion, yields (photocurrent/electrocatalyst), parametric optimization, as well as the PECR peripheral elements. The underlying idea is to identify the most efficient systems that could be extrapolated at large-scale for the UOR application, while simultaneously producing hydrogen at the cathode. For this purpose, the PECR are classified according to the reactor geometry and to the coupling mode with other reactor types (*i.e.*, electrochemical, photochemical, anode generating a photocurrent, electro-Fenton). Note that most of the electrolyses in PECR are carried out under potentiostatic conditions, as enabling to easily compare both photochemical and electrochemical contributions on the overall rate of organics removal or hydrogen production flux. Moreover, different sources of illumination in PECR are involved (Table 7). Solar simulators are widely used as allowing to mimic the natural solar irradiation, which includes 3 main components, ultraviolet (UV) rays (< 400 nm), visible light (400–700 nm) and infrared rays (> 700 nm), with energy distribution of 2 %, 47 % and 51 %, respectively [209,210].

For educational purposes, Table 8 reminds the principle of some wastewater decontamination processes based on the coupling of photo to electro-chemical methods (*i.e.*, photolysis (P), electro-oxidation (EO) or photocatalysis (PC)). These processes generate highly reactive species (hydroxyl, chlorinated or sulfated radicals) either: *(i)* by photon absorption and/or *(ii)* by redox reactions at the surface of the electrodes. In the following sections, the technologies used to implement these methods and to evaluate their efficiency for pollutants removal are presented in detail by describing PECRs according to their operation mode and geometry and their possible extension to photo-assisted urine valorization is discussed

3.2.1. *Batch-stirred type electrochemical and photoelectrochemical reactors*

Mixed metal oxides (Ti/Ir/Ru/Pt) are widely implemented as the anode to oxidize urea into discontinuous stirred type reactors (*i.e.*, batch reactors) of a low capacity (~ 10 mL) [223], using stainless steel as the cathode. In the presence of Cl^- in the anolyte, the electrogenerated ClO^- acts as an oxidant of the urea (**reaction (4)**). in this work, several systematic studies (*i.e.*, current density, pH, [NaCl], electrolysis time anode stability) and parametric analysis were carried out, thus enabling conclusions on the efficiency of the electrolysis compared to the mineralization of urea. Consumed urea and COD measurements were performed without establishing a full mass balance. The total cost for the removal of 1 kg of urea from 1 m^3 of aqueous solution (initial concentration of 2 kg m^{-3}) was estimated to be 0.78 $. A comparative assay was also performed by coupling a photochemical treatment system based on the use of 10 lamps illuminating at 365 nm (UV-A) to the initial electrochemical experimental set-up. However, no significant improvement in the urea conversion was obtained and the authors did not study the effect of H_2 cathodically electrogenerated on the electrolysis performances.

A discontinuous undivided PECR (Fig. 30) containing a suspension of TiO_2 photocatalyst powder was used by An and coworkers [201] to photo/electro/oxidize formic acid. The photocatalyst particles (30 nm mean size) were maintained in suspension in the liquid phase by injecting compressed air (slurry flows), and internally illuminated by an UV lamp (500 W high-pressure mercury lamp). The efficiency of formic acid removal was evaluated by measuring the COD. A so-called synergetic factor, SF, was introduced to describe the contribution of the three involved processes, as described in Eq. (3).

$$SF = R_{pe} - (R_p + R_e) \quad \text{(Eq. 3)}$$

Where R_e was the efficiency of the electrochemical process (*i.e.*, direct EO with low degradation rates), R_p the efficiency of the photocatalytic process (increased degradation rates), and R_{pe} the efficiency of the photo-electrochemical process (strongly enhanced degradation rates). Positive values of SF indicated the synergetic effect of both photocatalysis and electrochemistry in the oxidation of the pollutant (when compared to the single electrochemical process).

Based on the parametric optimization of the system, the authors have

Table 7
Different types of illumination sources used in PECR.

Illumination source	Device	Wavelenght (nm)
Natural solar light	Sun	100 – 2500
Simulated solar light	Solar simulator	280 – 4000
Visible light	Tungsten or Xenon lamp	400 – 700
UV-A	UV lamp	315 – 400
UV-B	UV lamp	280 – 315
UV-C	UV lamp	100 – 280

Table 8
Summary of existing electrochemical and/or photo-assisted processes in the field of wastewater treatment (Adapted from [211]; Copyright (2022), with permission of Elsevier and from [212]; Copyright (2020), with permission of Springer Nature).

Process type	Description		Ref.
	Principle	**Chemical reactions**	
Photolysis (P)	A chemical compound is broken down directly by the light absorption (generally in the UV-C domain)	Pollutants $\xrightarrow{h\nu}$ Degradation products	[213]
Photocatalysis (PC)	A photocatalyst material exposed to light facilitates a chemical reaction	$\text{Semiconductor} + h\nu \rightarrow h^+_{VB} + e^-_{CB}$ $\text{Pollutants} + (*OH,\ h^+,\ e^-, *OOH \text{ or } *O_2^-) \rightarrow \text{degradation products}$	[214]
Electro-oxidation (EO)	An electric current causes the oxidation of a substrate	$\text{Direct: Pollutants} \rightarrow \text{Degradation products} + e^-$ Mediated : $\text{Oxidant} + \text{Pollutant} \rightarrow \text{Reductant} + \text{Degradation products}$	[215]
EO & P	Synergistic effects of light and electrical energies for oxidizing a substrate	Coupling of EO and P reactions (as above)	[216]
EO & PC	Two different ways to oxidize the substrate: i) EO *i.e.,* direct oxidation at the electronic collector ii) PC which proceeds following two steps: first a photocatalyst in the bulk absorbs the light and then the electron transfer occurs from the photocatalyst to the substrate	Coupling of EO and PC reactions (as above)	[217]
Photoelectrocatalysis	Same as EO & PC but the photocatalyst is coated on the electrode (*via* photoanode)	Coupling of EO and PC reactions (as above)	[218]
Electrochemical advanced oxidation process (EAOP)	Technologies that use an high overvoltage electrode (for water oxidation) to generate highly reactive oxidizing agents, such as hydroxyl radicals	Anodic oxidation: $\begin{cases} M + H_2O \rightarrow M(^{\bullet}OH) + H^+ + e^- \\ M(^{\bullet}OH) + \text{Pollutants} \rightarrow M + \text{Degradation products} \end{cases}$ Electro-Fenton: $Fe^{2+} + H_2O_2 \rightarrow Fe^{3+} + {}^{\bullet}OH + OH^-$	[219]
EAOP & P	Electro oxidation involving hydroxyl radicals coupled to a degradation through light absorption by direct photolysis	Coupling of EAOP and P reactions (as above)	[220]
EAOP & PC	Electro oxidation involving hydroxyl radicals coupled to a degradation through light absorption on dispersed catalyst	PhotoElectro-Fenton: $\begin{cases} \text{Photocatalyst} + h\nu \rightarrow e^-_{CB} + h^+_{VB} \\ h^+_{VB} + H_2O \rightarrow {}^{\bullet}OH + H^+ \\ h^+_{VB} + OH^- \rightarrow {}^{\bullet}OH + H^+ \end{cases}$	[221]
EAOP & photoelectrocatalysis	Electro oxidation involving hydroxyl radicals coupled to a degradation through light absorption on coated catalyst	Coupling of EAOP and Photoelectrocatalysis (as above)	[222]

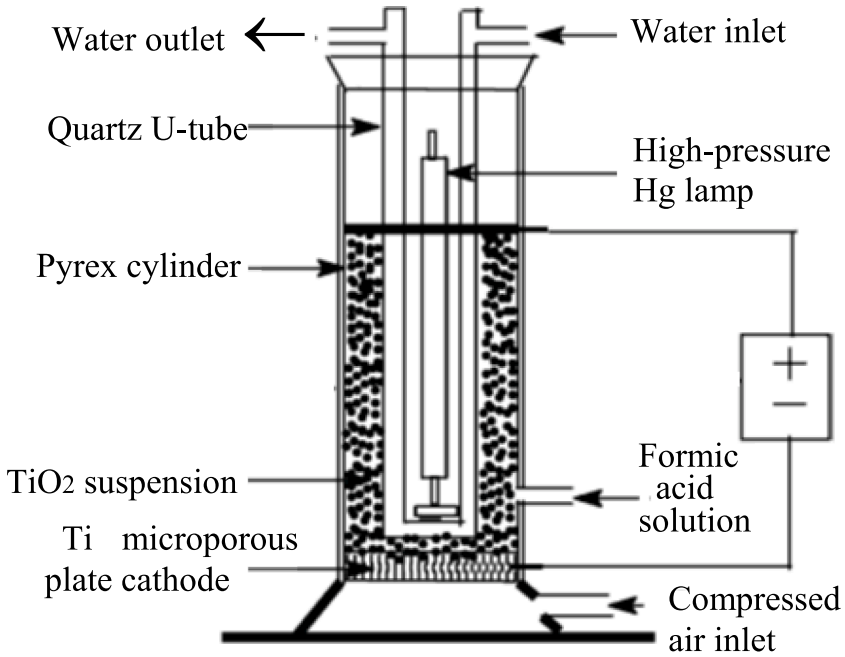

Fig. 30. Schematic representation of discontinuous slurry PECR stirred by sparged air, used for formic acid photoelectrochemical degradation. The outer cylindrical Pyrex casing was 55 mm in diameter and 250 mm in height. The thickness of the annulus containing TiO_2 particle suspension was 5 mm. Adapted from [201]; Copyright (2002), with permission of Elsevier.

pointed out the complex combined effects of the various parameters such as applied cell potential, treating time, airflow, pH, catalyst amount, and conductivity of the solution. The sparged air was expected to enhance the collisions of photoexcited TiO_2 particles in suspension with the surface of the electrode, and thus the probability of the photogenerated electrons to be captured by the electrochemical collector. Moreover, a beneficial effect of the introduced air microbubbles (*i.e.*, O_2) on the mass transfer of the formic acid was demonstrated. As air first

went through the cathode, the reduction of dissolved O_2 could also generate hydrogen peroxide (H_2O_2) that would act as an eventual oxidant of the pollutant. However, the presence of bubbles could reduce the rate of the photon transfer to the photoactive sites (light scattering). The synergetic effect of the three processes was evidenced, as well as the low efficiency of formic acid degradation in the presence of a simple process (either direct electrochemical (EO) or photocatalytic (PC) oxidation).

Even if such cylindrical geometry internally lighted (Fig. 30) seems efficient, some improvements could be proposed on various points. Firstly, the contact surface of the anode with the TiO_2 particles needs to be enhanced in order to increase the rate of the process. Several alternatives are available in this area, for example by depositing the photocatalyst directly at the anode and by illuminating from the external side, as shown later. Secondly, even if the value is not reported, the specific area (defined by the ratio of the electrode surface to the reactor volume) could be easily increased by modifying the location of the electrodes (electronic collectors) that are here placed orthogonally to the air flow direction. Lastly, even if this geometry is suitable to demonstrate the feasibility of the photoelectrochemical degradation of formic acid, it is not adapted because the production of H_2 at the cathode induces light scattering phenomenon, ohmic drop and loss of current by its oxidation. For these reasons, one can conclude that this type of discontinuous PECR is not relevant for the UOR.

A batch divided H-type PECR (Fig. 31(a)) was used 'as a battery' by Antoniadou and Lianos [197] to photo-oxidize, without external bias, various organic products (such as derivatives of biomass, surfactants and also urea) on nanocrystalline titanium dioxide (n-TiO_2) deposited on a FTO plate. The size of the active window for illumination was 2.5×3 cm^2 and the distance between the anode and the cathode 5 mm. O_2 was reduced on the cathode thanks to the electrogenerated protons at the anode.

The main objective of this study was to generate in situ photoelectricity by applying solar radiation (UV-A radiation was supplied by 4 Black Light tubes, 4×0.8 mW cm^{-2}), to use it for water decontamination (removal of some biomass derivatives). Note that *(i)* this PECR could also operate in natural solar light by exploiting the UV portion of the solar spectrum, and *(ii)* the produced photocurrent could be enhanced by adding other materials that absorb visible light as well. Different types of cathode material were tested (carbon cloth seeded by noble metallic nanoparticles of Pt, Pd or Au) in order to reduce the cathodic overpotential and, consequently to optimize the produced photocurrent (from 2 to 12 A m^{-2} for open-circuit voltages in the range of 1.4/1.8 V). In these PEC experiments, it is noteworthy that the pollutant conversion systematically remained lower than 15 %. Later, the same research group have built a more efficient PECR by pasting a Nafion membrane on the cathode electrode, an assembly directly inspired from hydrogen fuel cells, as shown in Fig. 31(b) [224]. However, no significant enhancement of the photoelectrical parameters was reported. Moreover, it was observed that the 'low' electronic conductivity of the FTO used as a current collector at the anode could cause noticeable ohmic drop when significant currents were involved as in industrial-type processes. At last, the used photoanode (n-TiO_2) exhibited low performances, and the efficient recovery of the H_2 generated at the cathode was challenging in this PECR geometry.

Hopsort et al. have implemented a batch-stirred electrochemical reactor (with and without membrane, illustrated in Fig. 32a) at the lab scale for UOR (~2 g of urea, ~100 mL) to get a better understanding of the effect of the operating parameters on the electrochemical urea abatement [136], before adding light irradiation in a PECR configuration. An analytical method, coupling total organic carbon (TOC) and IC, was developed to determine complete mass balances in the liquid phase for UOR (*i.e.*, accounting for all the electrolysis products). The impacts of alkalinity, temperature, and the presence of an anionic separator were specifically investigated. These authors showed that 80 % of the amount of charge supplied during UOR was consumed to produce other products different than N_2 and CO_3^{2-} (**reaction (3d) in** Table 3) such as ^-OCN and NO_2^- (**reaction (11) in** Table 3), as well as NH_3. Conversely to what was claimed by other authors, less than 10 % of N_2 was detected at the studied potentials (0.55 V *vs.* $Hg/HgO/OH^-$) [151]. Additional electrolysis in undivided H-type cell, revealed that NO_2^- electrogenerated at the anode could be subsequently reduced at the cathode, which decreased by 50 % the amount of harmful byproducts formed during UOR, when compared to those obtained when using the same H-type divided cell (note that the H_2 production decreased in equal proportion) [136]. Several criteria concerning the reactor configuration should be investigated further before approaching industrial conditions. In particular, the use of membrane –which usually represents a major part of the costs for the industrial development of EC reactors [225]– should be compared more rigorously. Indeed, the presence of this separator (*e.g.*, ion exchange membrane, diaphragm, etc.) will mostly affect the process performance in terms of energy and investment costs, and even more so with the high concentrations of organic compounds present in urine (*e.g.*, creatinine, creatine, bilirubin, etc.) which could limit the separator lifetime [226]. Optimization studies aimed at varying membrane materials, thickness and conductivity could, for example, be

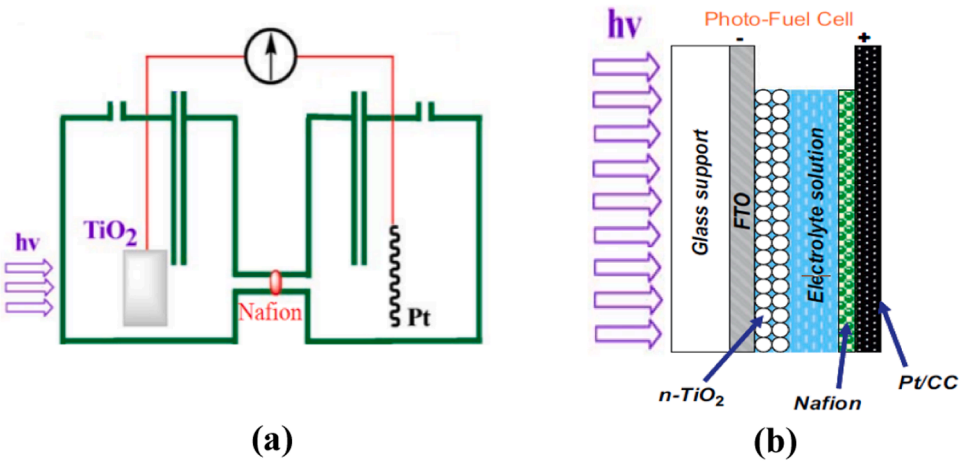

Fig. 31. Schematic representation of two types of lab-scale PECR, built with the same anode (nanocrystalline titanium (n-TiO_2) deposited on a FTO) and devoted to organics oxidation *via* the generated photocurrent. In Figure (a) (Adapted from [197]; Copyright (2009), with permission of Elsevier), the cathode was introduced into a separated compartment, while in Figure (b) (Adapted from [224]; Copyright (2010), with permission of Elsevier), the composite type cathode (Nafion graphite porous media) was located into the single compartment of the cell.

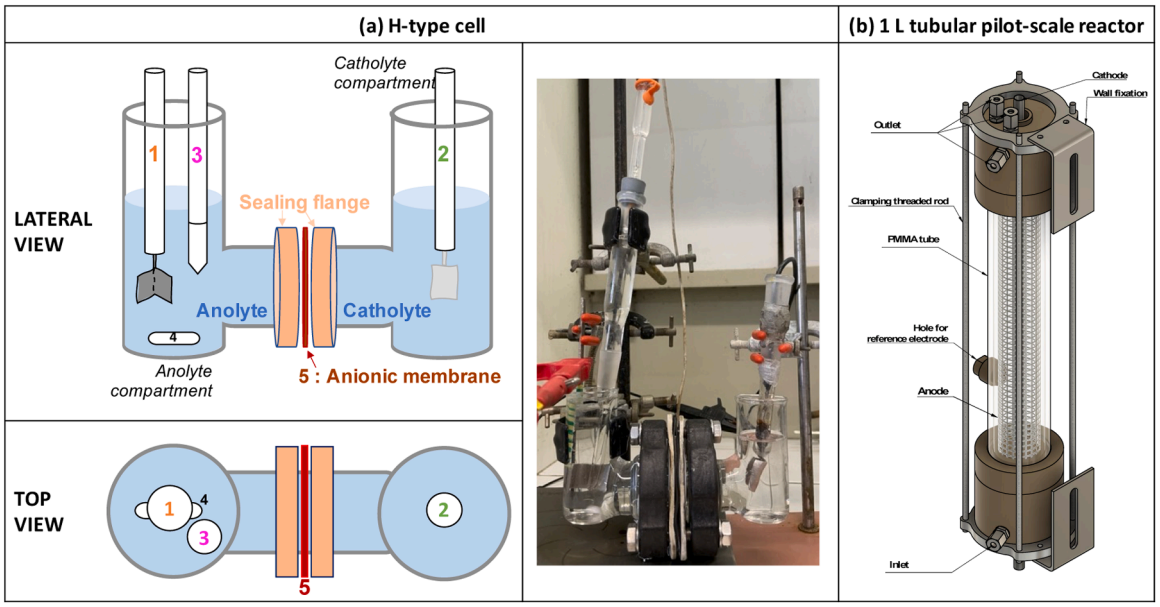

Fig. 32. Scheme and pictures of the experimental reactors used for electrolysis of urea in alkaline solution. a) divided compartment cell. Working electrode (WE) and counter electrode (CE) were identified as 1 and 2. Reference electrode was labelled 3. A magnetically stirring bar (4) was used to mix the electrolyte solution. The membrane separator (5) was held in place by flanges that maintained the seal. (b) Pilot scale reactor.
(a) Adapted from [136]; Copyright (2023), with permission of Elsevier. (b) Adapted from [86] (CC-BY 4.0 Elsevier).

carried out [227]. This group also studied reaction medium temperature influence and observed no effect on byproduct formation when varying from 293 to 313 K. The concentration of KOH in the electrolyte did not impact the composition of the byproducts produced. However, an increase in KOH concentration allowed the maximum oxidation current during UOR to increase, and thus the duration of potentiostatic electrolysis to be reduced. This advantage was counterbalanced by the fact that concentrated alkaline solutions are difficult to recycle in large-scale operation mode, a compromise has thus to be reached.

The same group has recently developed a 1 L tubular pilot-scale reactor operating in multi-pass mode [86] (illustrated in Fig. 32b). Potentiostatic electrolysis of urea synthetic solutions was conducted over 70 h. Complete analytical protocol (namely IC-MS [65] and TOC), nitrogen and carbon species mass balances were achieved of over 97 %, a milestone previously unreported at this scale. The study further examined the influence of operating parameters such as anode surface area, solution flow rate and applied potential on the UOR. This investigation underscored the impact of factor like reactor geometry, controlled potential and temperature on process efficiency. Parameters for optimal N_2 production, highest urea conversion rate, etc., were also defined. Finally, the electrolysis of human urine at pilot-scale unveiled new challenges distinct from those encountered with urea synthetic solutions. One can cite the interaction among various organic compounds (creatitine) in human urine, that significantly impacted the efficiency of the process.

An undivided stirred PECR (without flow) containing a graphite cathode and a large surface 316 stainless steel anode (active area of 180 cm^2), coated with TiO_2 NPs, was used by Chehade et al. [228] for H_2 production (Fig. 33). This PECR operated water splitting under potentiostatic conditions (E_{anode} = 1.5–1.8 V *vs.* NHE) and allowed to compare the results with and without solar-simulated illumination. The authors compared the volumetric flow rate of H_2 formed at the cathode without light (42 $cm^3\ h^{-1}$) and with photo-assistance involving an illumination power of 600 W m^{-2} (51 $cm^3\ h^{-1}$), which corresponded to an increase of the potentiostatic current by 10 mA (at the same applied potential). An extensive study was then performed to optimize the deposition of the TiO_2 NPs and the associated electrokinetic, expecting to improve the performances of the photoanode. This study demonstrated that under

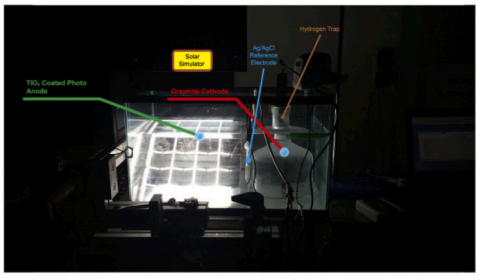

Fig. 33. Experimental setup of the PECR with TiO_2 photoanode used for H_2 production. Reprinted from [228]; Copyright (2018), with permission of Elsevier.

potentiostatic conditions, the irradiation enabled to increase, by more than 73 %, the global current of the system and thus the energy efficiency of the PECR (assuming the cell voltage constant) for H_2 production.

A batch stirred PECR (400 mL) was also used by Singla et al. [223] to investigate the photochemical/electrochemical effects on the oxidative treatment of urea (2 g L^{-1}) contained in wastewater under galvanostatic conditions, using mixed metal oxide anodes and a stainless steel cathode. The related mechanism combined the action of active chlorine species and the electro-Fenton process by coupling photocatalysis and EO. The influence of various parameters was systematically investigated and the UOR performance was evaluated in terms of both urea removal (more than 95 %) and energy consumption. The authors have used the three-level Box-Behnken design (BBD) based response surface methodology (RSM) for the experimental design, data analysis and parametric optimization. Empirical polynomial equations were then proposed for taking into account the operating parameters (*e.g.,* Cl^- concentration, pH, current density, time) and predicting the energy cost of the UOR. This process allowed transforming urea into NO_3^- and NH_4^+ by the action of $^{\bullet}OH$ (**reaction (5)**) and active chlorine species reacting in an indirect pathway with urea (**reaction (4)**). The use of light demonstrated a synergistic effect on mineralization because of the generation of strong oxidants like ClO^- and $^{\bullet}OH$ during both direct and indirect oxidation.

The durability of mixed metal oxide anodes was demonstrated by performing 90 cycles. The total operating cost for UOR was estimated at 0.78 $ m^{-3}. This PEC process [223], as well as some photoelectro-Fenton processes [229–231] have been demonstrated efficient for the electrochemical/photoelectrochemical mineralization of organic pollutants including urea. They proved the relevant role of the indirect pathway of urea conversion by active chlorine and hydroxyl radicals. Thus, future research efforts should consider this phenomenon in any PECR for urine treatment as Cl^- ions are naturally present in urine (≈ 0.1 M) [13], as previously described for electrochemical urine treatment in Section 2.1.

An annular electrochemical reactor illuminated from the internal side was developed by Peralta-Hernandez et al. [232] for generating hydroxyl radicals (Table 7). It consisted of a divided PECR (Fig. 34) coupled with an external tank acting as an oxygen absorber. A nanocrystalline-TiO_2 semiconductor cylinder was used as anode (diameter 1.0 cm, length 12 cm) and irradiated by a medium-pressure mercury lamp (the main radiations emitted by this polychromatic light source is at 365 nm, corresponding to the wavelength required for exciting TiO_2). TiO_2 was deposited on a glass substrate previously covered by a SnO_2–Sb_2O_3 layer in order to get some conductive and electrocatalytic properties. The cathode was a carbon cloth cylinder and a membrane could be introduced so as to separate the anolyte from the catholyte. Experiments were carried out in recycle-batch mode, meaning that the anolyte continuously flowed between the external absorber tank and the cell. Gaseous O_2 was dissolved into the absorber to get H_2O_2 from the O_2 cathodic reduction.

As shown in Table 7, combining the action of the electrogenerated H_2O_2 on $Fe^{(II)}$ (EAOP) and photocatalysis (PC) enables the efficient oxidation of Direct Yellow-52 dye in dilute acidic solution at high rates. Although this compound is chemically stable under UV radiation, the electrochemical oxidation rate increases substantially when the semiconductor anode is illuminated, compared to the same processes operating in the dark. By monitoring the H_2O_2 concentration, the TOC and the dye absorbance during the electrolysis, the authors have demonstrated the positive effect of the irradiation on the dye degradation.

Such a PEC system (EAOP + PC) could be adapted for continuously treating urea. For that,

- the transparent glass substrate used as an anode current collector needs to allow a strong adhesion of the deposits (eventual electrocatalysts and/or photocatalysts) to avoid possible attrition induced by some solid particles present into the effluents and/or release of bubbles, while possessing good electronic conduction to drive the electrons to the electronic collector and reduce the cell voltage as much as possible;
- the membrane, if used (to avoid hydrogen oxidation or other undesirable side reactions), should exhibit sufficient ionic porosity to limit ohmic losses (for example, some ceramic materials having porosity grades from 2 to 3 could be suitable);
- the radius of the anodic cylinder has to be reduced so as to maximize the irradiated specific area (defined as the ratio between the irradiated surface and the electrolyte volume).

A similar type of PECR was proposed by Shih et al. [233] for photo/anodic mineralization of organic acids (such as acetic, maleic, malonic, citric, oxalic, and succinic acids). The authors have implemented into a simple parallelepipedous tank (12 cm × 12 cm × 30 cm) four undivided cylindrical electrochemical cells without any ionic separator (Fig. 35). All the cells were immersed into the same electrolyte, which also contained NaCl (0.5 M) in order to take advantage of the electrogenerated ClO^- action. Both electrodes were made from titanium-based DSA coated with IrO_2/RuO_2. For each cell, a central rod constituted the cathode while a cylindrical grid, quasi-transparent to the UV light, was used as anode. A cylindrical UV-C lamp was located in the middle of the parallelogram tank, enabling it to simultaneously illuminate all four cells, at 254 nm. The mean light intensity supplied by this lamp is 2.04 mW cm^{-2} at a distance of 3 cm away from the lamp.

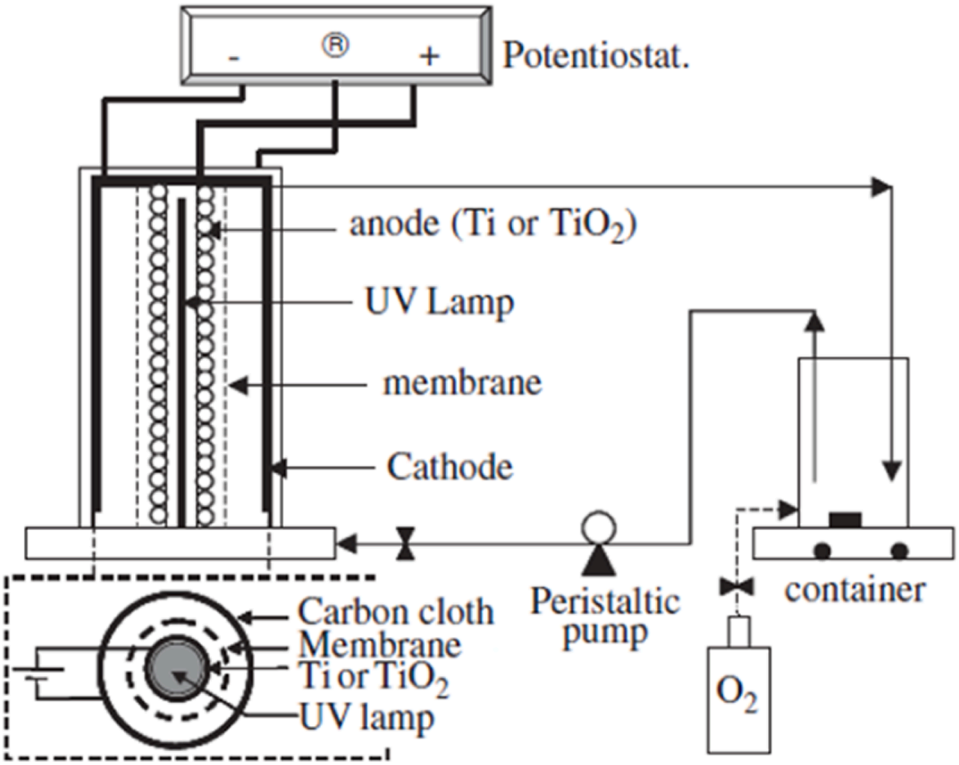

Fig. 34. Schematic representation of a stirred PECR operating with a recycling loop for the anolyte coupled to an O_2 absorber and used for the photo-electrochemical oxidation of the Direct Yellow-52 dye. Adapted from [232], Copyright (2006), with permission of Elsevier.

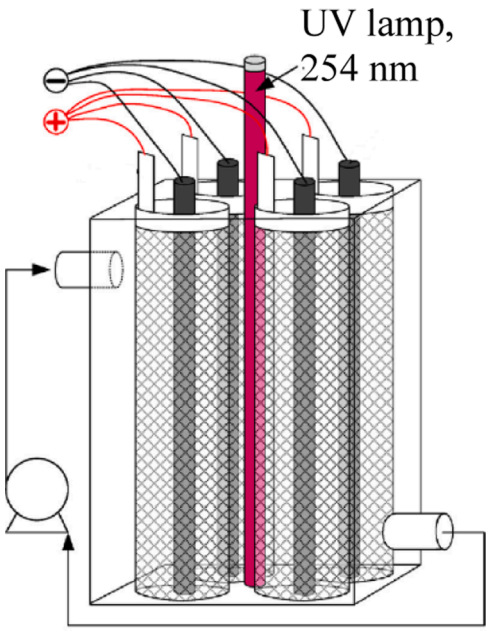

Fig. 35. Schematic representation of a continuous recycling electrolyte PECR made of four undivided annular elementary cells, illuminated by an UV-C lamp located in the middle of the parallelepiped tank. The four cathodes (internal cylinders) and the four anodes (external cylindrical grids) are made of the same material (Ti – IrO_2/RuO_2). Adapted from [233]; Copyright (2014), with permission of Elsevier.

Galvanostatic electrolyses of the acidic solutions, coupled or not with light illumination, were performed. The authors showed that the mineralization of organic acids remained low (*i.e.*, TOC removal below 30 %) if only the electrochemical or photochemical action was involved. However, combining electrolysis and photocatalysis enabled a substantial improvement of the mineralization whatever the nature of the organic acid studied (*i.e.*, the TOC removal varies between 83 % and 95 %). This enhanced performance (EAOP + PC) was attributed to the activation of the anode (Ti covered by IrO_2/RuO_2) by the UV irradiation that generated some radicals $^{\bullet}OH$ and $^{\bullet}Cl$. Unfortunately, neither the products formed at the cathode nor the possible effect of H_2 generation on the illumination efficiency (*i.e.*, the light scattering induced by H_2 bubbles) were discussed.

This set-up could be easily extrapolated for the UOR treatment at the lab scale, by choosing the adapted electrode materials, and after performing some minor modifications such as:

- in the case of an undivided cell, one should operate with a vertical flow for each cathode to easily remove the hydrogen gas that must be generated and kept far from the anodes.
- reflective mirrors should be implemented at the internal walls of the parallelepipedous container to extend the irradiated specific area and thus maximize the number of photons absorbed per unit of volume and time.

3.2.2. *Cylindrical continuous-flow type photoelectrochemical reactors*

Esquivel et al. [234] proposed a lab-scale cylindrical continuous-flow PECR illuminated by UV-C light, equipped with three-compartments of 9 cm length and 5.5 cm inner diameter (Fig. 36) and coupled with a continuously oxygenated storage tank containing the pollutant (Azo orange II dye) solution. The principle is similar to the one described in

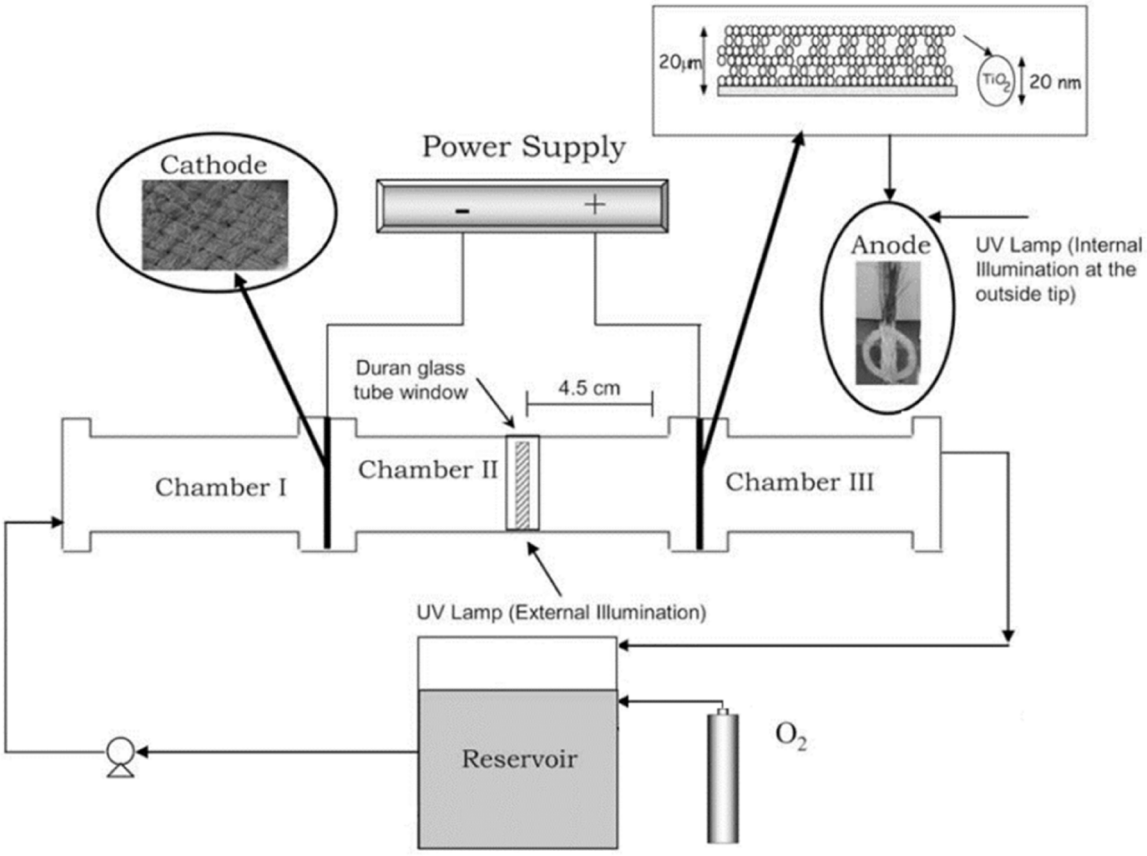

Fig. 36. Schematic representation of a cylindrical continuous-flow PECR (0.64 L), constituted by three successively supplied compartments, and operating with a recycling loop. Adapted from [234]; Copyright (2009), with permission of Elsevier.

Fig. 34 [232]. The authors investigated the combined action of photochemical and PEC treatment for the anodic degradation of organic pollutants. The mixture was saturated in O_2 in the storage tank with the idea to generate H_2O_2 from the O_2 cathodic reduction. The solution was continuously recycled into the three-compartment reactor (at a constant flow rate of 80 L h^{-1}), first across a carbon felt cathode to allow H_2O_2 generation. Then, the solution went through a second compartment, which could be externally illuminated, to activate the photochemical pathway *via* the reaction between pollutants and generated hydroxyl radicals (Fenton reagent). Finally, the electrolyte arrived inside the third 'photoanodic' compartment where was located an optical fiber support: on the surface of this support a semiconducting layer was deposited and acted as either a photocatalytic or photoelectrocatalytic anodic material (30 mm thickness SnO_2 : Sb film on which the photoactive TiO_2 layer was electrophoretically deposited). In this way, the authors successfully achieved the complete removal of Azo orange II dye (15 mg L^{-1}) and a 57 % TOC removal efficiency within 60 min of operation duration. This efficiency resulted from the simultaneous implementation of three treatments: chemical (H_2O_2), photocatalysis with TiO_2 and electrochemical oxidation are close to those observed in the work of Peralta-Hernandez et al. [232].

However, the scale-up of this PECR remains challenging without loss of performance due to the difficulty of maintaining at both scales the same (or higher) electrode specific area (*i.e.*, the ratio between the electrode surface and treated volume). A numbering-up strategy could be an interesting alternative, consisting of multiplying the number of individual set-up (cylindrical reactors) for treating larger volumes of pollutants. In this case, it would be more convenient to put these cylindrical reactors in a semi-circular configuration for operating with an external illumination source, even if, in the case of natural solar light irradiation, mirrors would be also required for an efficient use of the light at the whole surface of the photoanode. To avoid any possible mass transfer limitation (not studied in this work), the system could be optimized by *(i)* choosing a horizontal photoanode (such as a functionalized expanded grid), *(ii)* reducing the compartment diameter (a few cm), and also *(iii)* creating tangential inlets of electrolyte to intensify the mixing between the different reacting species (by generating swirling turbulent flows). This system could be applied to the urea treatment provided that a hydrogen gas collecting system is implemented so as *(i)* to avoid its reoxidation at the anode (studied in [235]), *(ii)* to reduce the ohmic drop introduced by the gas, and *(iii)* to avoid losses by the light scattering of the H_2 bubbles. Finally, the vertical configuration could be more efficient for the removal of H_2, instead of a horizontally-oriented reactor.

The review of Keane et al. [236] addressed the main challenges related to the application of solar photocatalysis for wastewater treatment. These authors included the description of the reactional mechanisms, the advances in electrode materials and the recent developments in reactor design. They showed that the combination of solar disinfection and photocatalysis technologies (based on the use of semiconductors such as TiO_2, ZnO and nano-heterojunctions) could enable efficient removal of pathogens from drinking water. In particular, reactors made of glass tubes (several continuous-flow reactors) and mirrors, used as light parabolic concentrators/'recuperators', were specifically discussed (Fig. 37). According to these authors, the high efficiency of these reactors, in particular when compared to flat systems, was due to the homogeneous distribution of solar radiation into the absorber by using both diffuse and direct radiations (Fig. 37b). The major factors affecting the efficiency of solar-based photocatalysis systems were the following:

- the fraction between the irradiated volume and the total volume (the dark zones, such as the storage tank or pipes, must be minimized);
- the photoreactor diameter which controls the optical path length;
- the catalyst loading, in suspension into the liquid phase or immobilized over a solid, which needs subsequent post-disinfection/treatment;
- the optimal inclination of the reactor that enhances the collection of direct natural solar radiation to the detriment of the diffuse ones, and that can be adjusted depending on the position of the sun in the sky during the day and all along the year;
- the solution flow rate, which should allow *(i)* avoiding aggregation of the catalyst while inducing efficient collisions between the pathogens and the catalyst, *(ii)* good absorption flux to operate with sufficient oxygen content.

At last, these authors concluded that the commercialization and massive production of solar photocatalytic systems remain nowadays highly challenging, and thus provided various guidelines for addressing issues related to mass transfer, photoreactor design and visible light absorption by TiO_2 coatings.

It is interesting to note that such compound parabolic collectors (CPCs) shown in Fig. 37 could be applied for solar UOR treatment at a large-scale, and more generally for any solar process producing H_2 at the cathode. Indeed, they allow for increasing the light absorption yield, but also achieving homogeneous photochemical treatment over the whole treated solution volume. For cylindrical-shaped anodes generating a photocurrent, this light collector is also of great interest. In contrast, the horizontal configuration of the photoreactors is not suitable because of the difficulty of H_2 bubbles removal from the reactor: vertical, or even inclined, configurations should be preferred.

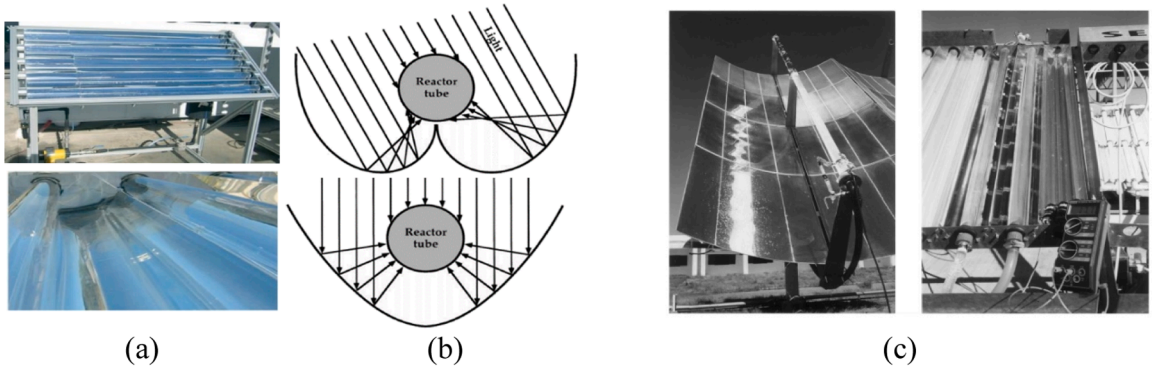

Fig. 37. Pictures of typical solar photochemical reactors for water disinfection: (a) and (b) are adapted from [236]; Copyright (2011) with permission of Royal Society of Chemistry and (c) is adapted from [237]; Copyright (1999), with permission of Elsevier). (a): the reactor was made of several glass tubes (borosilicate having 90 % transmission at UV) and of polyethylene pipes and valves. The parabolic collector of the light (anodized aluminum with a high (~90 %) reflectivity in the UV range) was located around the tube. (b): Schematic solar light pathways involving direct and diffuse radiations for two different incident radiations. (c) The solar photochemical reactor for water disinfection was initially designed by Fernandez-Ibañez et al. (1999) [237].

3.2.3. Filter-press continuous-flow type photoelectrochemical reactors

An undivided filter-press type PECR was used by Malpass et al. [238] for the degradation of atrazine (pesticide). Continuously supplied by the electrolyte (flow rates varying between 32 and 425 cm^3 min^{-1}), the reactor (Fig. 38) was illuminated from the rear side (Ti grid cathode), across a quartz plate which defined the illumination window (14 cm^2). The light penetrated into the electrolyte through the Ti grid cathode, then crossed the IONAC® membrane window, and finally illuminated the photoanode (DSA-chlorine made by $Ti/Ru_{0.3}Ti_{0.7}O_2$). The electrolyte (Na_2SO_4 and organic compound), stored in an external tank, was continuously recycled into the unique compartment of the reactor.

Malpass et al. [238] used as criterion, the electric energy per order, E_{EO}, defined by Bolton et al. [239] when low concentrations of pollutants are involved, according to Eq. (4):

$$E_{EO} = \frac{\text{Electrical power supplied} \times \text{time}}{\text{Total solution volume} \times \log(C_{initial}/C_{final})} \quad \text{(Eq. 4)}$$

E_{EO} thus represents the electrical energy in kWh required to reduce the concentration of atrazine by one order of magnitude in a unit volume (m^3) of contaminated water. This parameter allows to compare the performances of electrolyses performed with or without photochemical assistance. The authors observed that the current-potential curves before electrolyses did not indicate significant effect of the anode illumination on the pesticide oxidation rate. However, the electrolyses carried out under illumination (at 200 A m^{-2}) and at various operating conditions, revealed that the electric energy per order, E_{EO}, was 20 times lower than the one obtained for the purely electrochemical oxidation at the same current density. Moreover, the combined photo-assisted method enabled fast and efficient pollutant removal (less than 2 h of photoelectrolysis with more than 80 % of pollutant abatement). The effect of electrolyte was systematically studied. Note that:

- even if satisfactory results were achieved, the irradiation from the cathode side was again suffering from losses by light scattering due to the H_2 bubbles;
- the efficiency of this filter-press reactor would be difficult to maintain at larger-scale, mainly due to the limited light penetration across a stack of several electrolytic compartments (especially in the presence of ion-exchange membrane).

A similar design of PECR was built by Lopes et al. [202] (Fig. 39) to split water into H_2 and O_2. It consisted of a continuous-flow parallelepipedal-shaped PECR, with or without separator (Dark Nafion® membrane or Teflon diaphragm exhibiting high reflectance). This study focused rather on the electrode material and its characterization than on the importance of the device and the associated treatments reported. The authors investigated various types of photoelectrodes: WO_3 anodized on a metal substrate (not transparent) or deposited on a transparent conductive oxide (TCO) glass substrate, and undoped Fe_2O_3 also deposited on a TCO glass substrate (transparent). To concentrate the received light and to ensure efficient illumination of the electrodes from both sides, high reflectance mirrors were used, located on both sides of the transparent windows on the PECR.

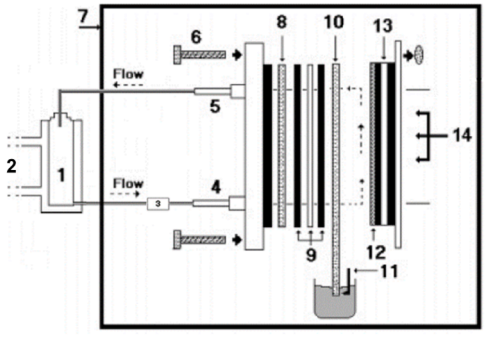

Fig. 38. Schematic representation of an undivided filter press PECR: (1) continuously recycled electrolyte's tank; (2) thermoregulated fluid; (3) pump; (4)/(5) electrolyte inlet and outlet; (6) screw; (8) photoanode ($Ti/Ru_{0.3}Ti_{0.7}O_2$); (9) Teflon gaskets for studying the effect of the thickness of the electrolytic compartments; (10) IONAC® membrane acting as ionic conductor for the reference electrode (11); (12) cathode: Ti-mesh; (13) quartz glass; (14) Incident UV light produced by a mercury lamp (4.2 kW m^{-2} emitted at 254 nm). Adapted with permission from [238]; Copyright (2007), American Chemical Society.

The authors claimed that the system also took advantage of the reflectance of the Teflon diaphragm, which would increase the generated photocurrent. Different materials were used for the lighting window: *(i)* quartz window cutting the light absorption below 250 nm; *(ii)* soda lime glass cutting below 350 nm; *(iii)* amorphous / fused silica (90 % of transmittance in the visible and good stability against bases or acids at concentrations below 1 mol L^{-1}), or *(iv)* Pyrex (similar properties than iii). Cheaper materials, such as polycarbonate (having good, *i.e.*, ~ 90 %, transmittance in the visible) could also be used for the lighting window, even though they could be easily scratched during handling and thus need to be changed more often. The measurements were performed in the dark and under solar light simulator conditions (AM1.5 G: 1 kW Xe lamp, 1 kW m^{-2}, 25°C). The obtained current-potential curves showed an increase of the current under illumination at a constant potential, but this increase remained low (~ 1 mA cm^{-2}) and the observed solar-to-H_2 conversion efficiency, STH, defined by the Eq. (5), did not exceed 1 % during the electrolyses. Note that these authors also suggested to use hydrophobic Teflon membrane to separate electrogenerated gases from the electrolyte.

$$STH = \frac{H_2 \text{ production } \left(\frac{mol}{s}\right) \times \text{molar free enthalpy } H_2 \left(\frac{kJ}{mol}\right)}{\text{illumination power (W)}} \quad \text{(Eq. 5)}$$

Brillas et al. investigated the degradation of different organics by the electro-Fenton process. In particular, some interesting results at large scale have been achieved in a PECR composed of a 10 L reservoir, an undivided filter-press electrochemical cell of 90.2 cm^2 electrode surface area and a solar CPC photoreactor of 1.57 L irradiated volume (Fig. 40). The photoelectrolyzed solution was continuously recycled into a storage tank. The cathode used was an air-diffusion 3D material generating H_2O_2 for the further hydroxyl radicals production through the Fenton reagent action. These authors have chosen paracetamol [230] and chloramphenicol [231] as two typical biomedical pollutants to mineralize [229]. Even if satisfactory results were obtained with paracetamol (solar photoelectro-Fenton treatment enabling a TOC abatement of 75 % in 2 hours of electrolysis, with an energy consumption of 7.0 kWh m^{-3} and a mineralization current efficiency of 71 %), the results with chloramphenicol were modest (TOC abatment ~90 % in 3 hours of electrolysis, with an energy consumption of 30.8 kWh m^{-3} and a mineralization current efficiency of 36 %). They proposed an empirical relationship enabling to model the TOC evolution as a function of the applied current, as well as the concentration of the pollutant in solution. These authors deeply examined their systems and proposed an oxidation mechanism, showing that the light irradiation had a relevant impact on the acidic intermediates formed during pollutants degradation (complexed with the iron(III)). Unfortunately, no comparative energy consumption calculation was made between electrolysis and photoelectrolysis configurations. Implementing such PECR for the UOR treatment would certainly require some additional precautions and investigations. Indeed, the chemical oxidation of urea by NiOOH leads to the production of some small organic fragments, that would probably not directly react with the photons emitted by the solar irradiation, especially in absence of active chlorine species or $^{\bullet}OH$ radicals. More importantly, the supplementary advantage related to the H_2 cathodic production during UOR disappears if the O_2 reduction reaction takes

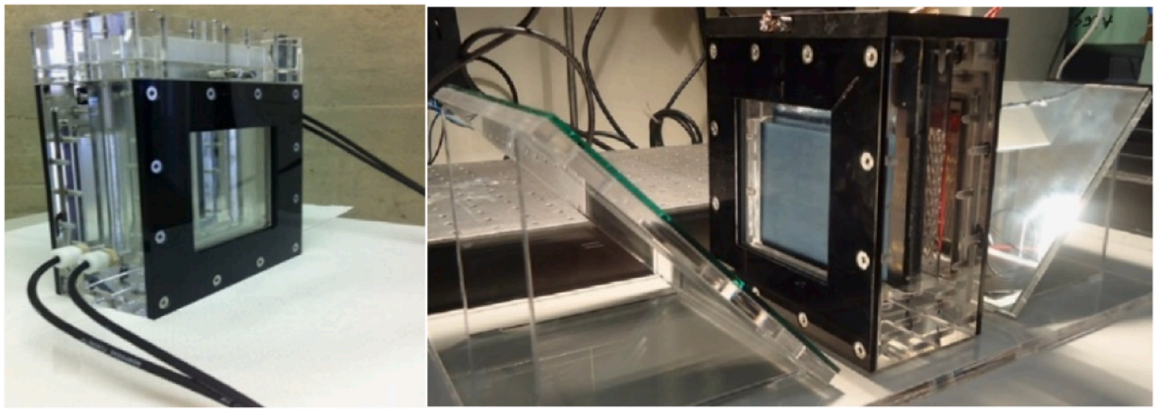

Fig. 39. Schematic representations of a filter press PECR (left side) and the experimental device exhibiting reflecting mirrors on both sides of the reactor (right side). Adapted from [202]; Copyright (2014), with permission of Elsevier.

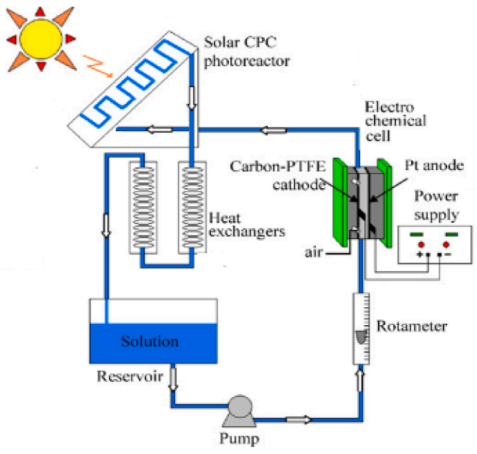

Fig. 40. Solar photoelectro-Fenton degradation of paracetamol using a non-divided filter press PECR with a Pt/air-diffusion cell coupled to a light parabolic collector. Reprinted from [230]; Copyright (2011), with permission of Elsevier.

place at the cathode (to generate H_2O_2).

3.2.4. *Modeling electrochemical and photoelectrochemical reactors*

Mousset and Dionysiou [212] recently proposed a review on PECR for treatment of water and wastewater. Interestingly, a table introducing the type of the reactor as function of the process implemented (mainly focusing on photoelectro-Fenton/photocatalysis) was established, allowing to briefly summarize a very large number of studies. From it, these authors provided, depending on the targeted application, practical guidelines in terms of reactor design, sequential *vs.* hybrid reactors, divided *vs.* undivided cells, continuous *vs.* batch mode, mass transfer enhancement, light source positioning and light source distance to the electrode. This table also pointed out the existing combinations between electrolysis, photocatalysis or photoelectrocatalysis technologies applied to wastewater treatment (see Table 8). Nevertheless, the UOR treatment was not included in this review paper. Moreover, FTO electrode was generally proposed as anodic current collector, which was not the most appropriated system for large scale industrial applications requiring high current densities, especially because of the difficulty to ensure efficient long-term electrical connection.

Kelsall et al. [203–205] pointed out, for H_2 production by water splitting, the need to optimize the design of the PECR for improving the performance, typically for *(i)* maximizing the photon absorption, *(ii)* preventing side reactions by separating the electrogenerated products, *(iii)* optimizing the potential distribution, *(iv)* improving the stability of the electrode materials used, and finally *(v)* reducing the cost of the reactor. For this purpose, they consider small-scale reactors based on PVDF body with a single quartz aperture, externally illuminated and involving composite photoanodes made by Ti/Sn^{IV} –Fe_2O_3 [203–205]. The latter consisted of Fe_2O_3 films deposited on transparent glass substrates coated with a thin layer of conductive FTO. Various configurations of the system 'illumination source *vs* electrodes position' were examined (Fig. 41, a-d) in order to define the optimum (shorter) ionic current pathway, namely the one minimizing potential losses (ohmic losses). By such investigations, the authors aimed at designing, optimizing and demonstrating the commercial feasibility of such PECR. These different configurations were modelled using the software COMSOL Multiphysics 4.4 (Batteries and Fuel Cells module with LiveLink for MATLAB and with implementing finite element method). The potential and current distributions were determined, as well as the effect of ohmic drop caused by various parameters (such as the photoanode type/-geometry and the gas bubbles electrogenerated). These simulations showed that all four configurations presented some disadvantages:

- The configurations (a) and (d) induced non-uniform current density distributions between the two electrodes, which was expected to give rise to regions of very low current density on the surface of the photoanode. This effect was investigated by systematically decreasing the electroactive Fe_2O_3 surface area using varnish to partially block the electrode surface, starting from the center of the electrode and measuring the resulting current. The results showed that the current flowed at the perimeter of the electrode, with more than 25 % of electro-inactive surface in the middle of the FTO plate.
- The drawback of the configuration (b) was the inevitable attenuation of the photons by the mesh cathode, as well as by the membrane which, even not shown, would be necessary in practice. Since the open area of the mesh was ca. 50 % of the geometric area, it would proportionally decrease the mean photon flux.
- Despite the current distribution problems of the configuration (a), the performance of the photoanode remained better than in the case of configuration (b).

The current density decreased from the extremities of the anode (i.e the electrical connection) to the middle of the electrode for FTO-based electrodes, implying that the scale-up based on such electrodes would be challenging because of the important losses in potential. Thus, these authors proposed to use a partially expanded mesh substrate as photoanode, in order to prevent any problem of current distribution and maintain an 'acceptable' quality of the electrode illumination (Fig. 41c). Furthermore, they also demonstrated that O_2 bubbles could be detrimental *(i)* to the photons absorption efficiency (light scattering) and *(ii)* to the H_2 production rate because of the O_2 reduction at the cathode.

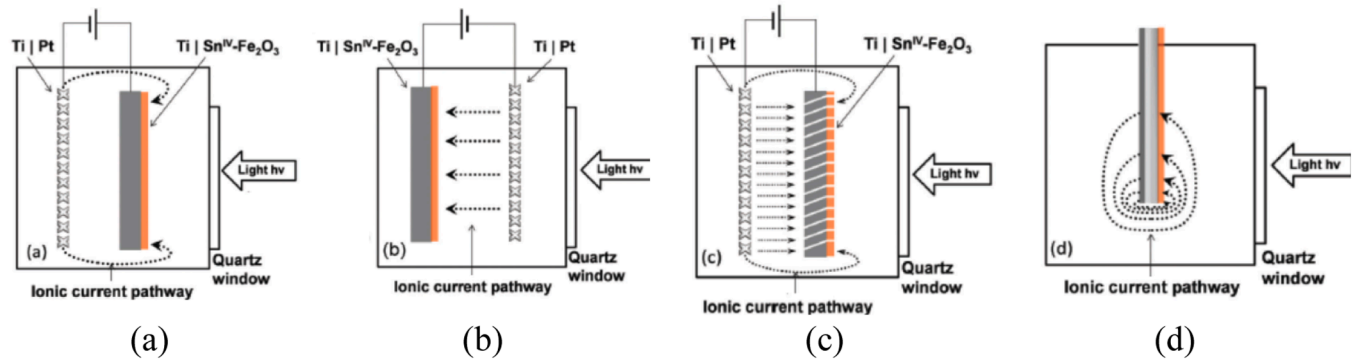

Fig. 41. Schematic representation of the current pathways as function of the geometry of the PECR, and in particular of the relative position of the electrodes with respect to the light source (Reprinted from [204]; Copyright (2016), with permission of Royal Society of Chemistry).

Consequently, they suggested to remove the gas from the reactor volume and to define an *ad hoc* reactor geometry enabling the most possible uniform current distribution. Kelsall et al. have also modelled larger scale PECR (*i.e.*, larger than 0.1 m × 0.1 m) in order to evaluate the effect of electrode geometry and configuration, on the spatial distributions of the current and the potential, photon flux, as well as the resulting H_2 evolution rates [204]. Typically, lowering the ionic conductivity or/and increasing the activity of the photo-anode induced inhomogeneities. Such findings were essential for optimizing the design and photon energy-to-H_2 conversion efficiencies of PECR for their industrial implementation. For example, they proposed choosing an 'open shape' mesh type photoanodes (such as indicated in Fig. 41c), which allowed decreasing 'ionic current path lengths' and thus uniformizing the current density distribution; such improvement was preferred even if it led to significant losses in the photon absorption. All these results could be transposed to the UOR treatment. An undivided reactor enabling to reduce the ohmic drop in the PECR due to the separator appears as the most suitable configuration. Typically, a vertical cylindrical reactor could be chosen and the whole system could be composed of a central tubular cathode and a photoanode made of cylindrical expanded metal (coaxial to the cathode) and externally illuminated. This geometry offers the following advantages: *(i)* easy removal of the H_2 bubbles (at the top of the reactor) and *(ii)* an easy and efficient illumination at the entire peripheral area of the photoanode by using parabolic mirrors irradiated by natural solar power.

Recently, the UOR has been also studied and modeled (Fig. 42, a-b) by Hopsort et al. [141] using an electrochemical H-type reactor (divided, as the one shown in Fig. 32). An original approach was developed to determine and model the kinetics of the catalytic UOR in alkaline medium on nickel(III) sites with the perspective of scaling up the UOR in pilot reactors. A multi-pathway mechanism was also proposed enabling to better understand the formation of UOR byproducts. After an extensive kinetic and mechanistic study, the same authors built microscopic and macroscopic models combining kinetic laws with diffusive and convective transport phenomena (assuming a fast electronic transfer). The robustness and relevance of the latter were demonstrated (Fig. 42, c-e) by comparing the experimental results obtained during laboratory-scale electrolysis with those predicted by the model. The theoretical results, confronted to the experimental ones, allowed to show the effect on the urea conversion *(i)* of the alkalinity and *(ii)* the electrode geometrical localization into the reactor. In agreement with the results already reported by Kelsall et al., Hopsort et al. pointed out (Fig. 42, e) the undesired anodic oxidation of electrogenerated H_2 in the case of an undivided PECR.

4. Conclusion and perspectives

Electrochemical and PEC methods for urea and ammonia conversion from urine by UOR and AOR, respectively, were deeply described in the present review article and the most recent achievements have been included by updating Fig. 43.

Urine collected in urban wastewater represents 80 % of the total nitrogen load reaching WWTP. Selective collection and treatment of urine at the source can significantly reduce energy consumption and increase treatment capacity in WWTP. In particular, urea contained in urine (0.2 – 0.33 M) represents a cheap, abundant and recyclable nitrogen source relevant in circular economy from simultaneous wastewater treatment and H_2 production. Two different electrochemically active N-rich molecules can be found in urine depending on the urine effluent stored time and pH ($CO(NH_2)_2$ or NH_3). Strong alkalinization (pH>14) of fresh urine properly blocks the biological urea degradation into NH_3 ($\leq$ 5 %). However, it provokes scaling and clogging in the pipelines. In contrast, more than 90 % of urea is converted into NH_3 in stored urine, which provokes a moderate alkalinization (pH $\approx$ 9), as well as Ca^{2+} and Mg^{2+} precipitation.

The electrochemical UOR and AOR represent an interesting approach for urine valorization and have been explored in Cl^- containing solutions because those anions are present in the standard urine composition ($\approx$ 0.1 M). This implies urea and NH_3 conversion through an indirect pathway by reacting with electrogenerated active chlorine species and hydroxyl radicals. Nevertheless, this Cl^- based conversion pathway might provoke the formation of dangerous chlorinated products such as chloroamines, which represent a particularly relevant side reaction in NH_3-rich stored urine effluents. Depending on the nature of the anode, the final products from UOR and AOR differ, being the incomplete oxidation of nitrogen species to NO_2^- more relevant from active chlorine than hydroxyl radicals. In addition to this, electrolysis of stored urine with simultaneous urea and ammonia oxidations in alkaline solution requires a comparative study of the most promising catalytic materials, since only independent studies for either UOR or AOR have been reported so far. $Ni(OH)_2$ doped with Cu and NiOOH electrodes represent two of the few active electrocatalysts for both UOR and AOR. However, the optimal solution pH in each case is different. Moreover, a severe corrosion of NiOOH electrode and subsequent release of Ni cations in solution has been reported during AOR. The performance of those anodic materials for UOR and AOR is impacted by the presence of creatinine and other electroactive organic molecules (histidine and creatine) in the urine matrix, as they contribute to electrode deactivation and/or compete with urea degradation at the electrode surface. Some different approaches based on electrocatalyst engineering are under development to overcome the electrode deactivation issue.

The UOR mechanism on NiOOH catalyst mainly follows an indirect pathway where the chemical oxidation reaction of urea takes place at the NiOOH electrode surface, as demonstrated by XRD, Raman spectroscopy and CV. In contrast, the AOR mechanism on NiOOH electrode follows an inner sphere reaction mechanism [240] where the reactant is initially adsorbed on the electrode before the electron transfer takes place. However, the production of green H_2 coupled with either UOR or

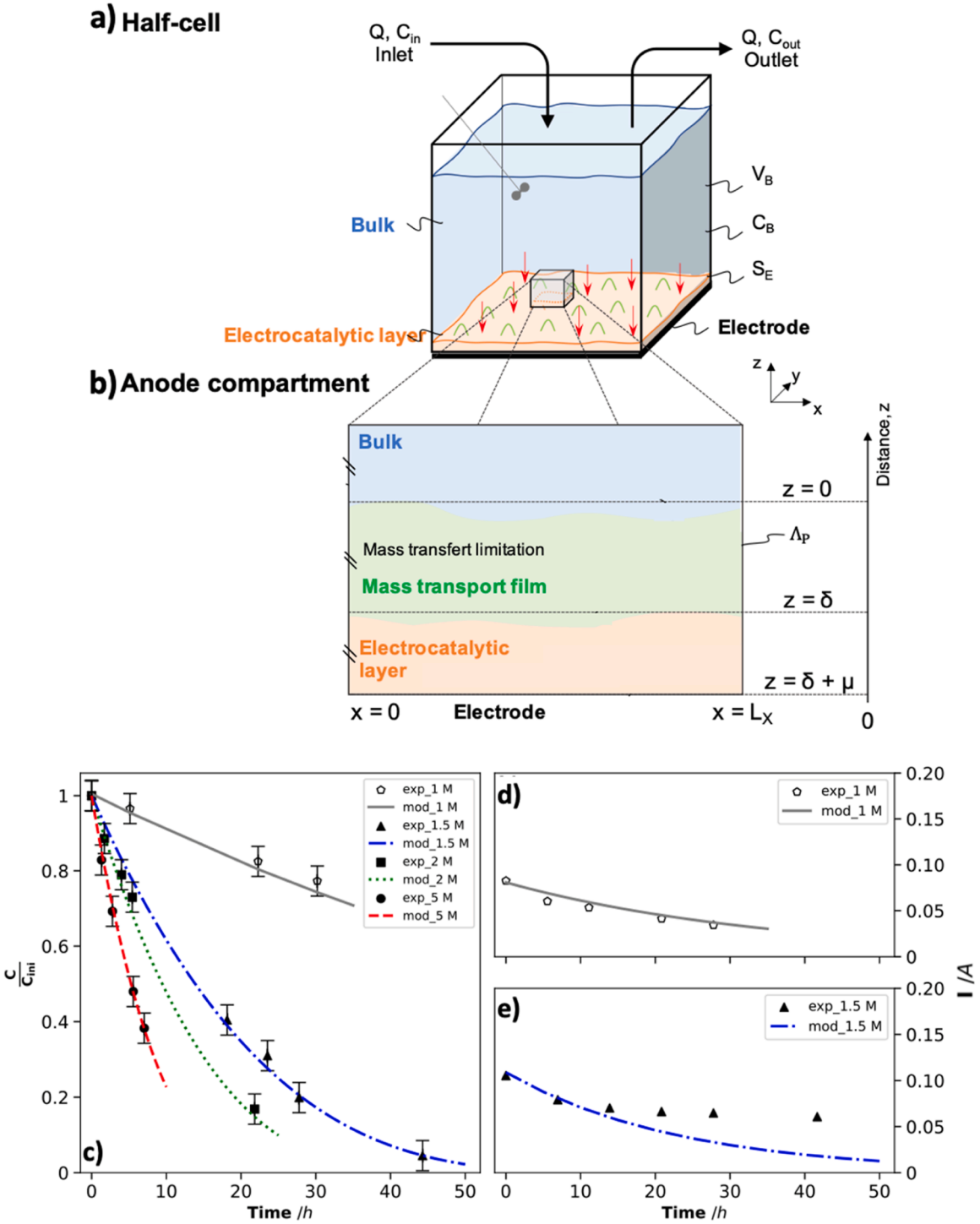

Fig. 42. Some results obtained for the UOR modeling. (a) Schematic representation of the electrochemical half-cell. The blue area represents a perfectly stirred liquid phase (the bulk), and bottom area represents an electroactive layer of Ni-based oxides on the metal electrode surface. (b) View of the various "sensitive" areas including limiting physical phenomena. (c) Temporal variations of the normalized urea concentration in the bulk during potentiostatic electrolyses on massive Ni electrode in alkaline media. Experimental results are plotted for different KOH concentrations: 1 M (⌓), 1.5 M (●), 2 M (■) and 5 M (▲). Filled symbols are obtained with an S/V ratio of 8 m^{-1}. The unfilled symbols are obtained with an S/V ratio equal to 20 m^{-1}. The lines represent the temporal profiles of the urea concentration predicted by the model at each KOH concentration. (d-e) Experimental and predicted profiles of the current intensity during electrolysis with a distance between electrodes of (d) 15 cm using a H-type cell without separator and (e) 3 cm using an undivided Metrohm® type-cell. Adapted from [141] (CC-BY 4.0 Wiley Periodicals LLC).

AOR on NiOOH anodes from a thermodynamic point of view requires an E^o_{cell} of −1.32 V, a bit larger than the one required for H_2O electrolysis (-1.23 V). Thus, these thermodynamic calculations presented here challenge the potential of UOR and AOR in replacing the OER for H_2 production from electrolysis in alkaline solution on NiOOH anodes, due to the high E^o value required for the formation of NiOOH. Finding new highly active catalysts for either UOR or AOR is crucial to compete with water splitting for H_2 production by minimizing the overpotential and

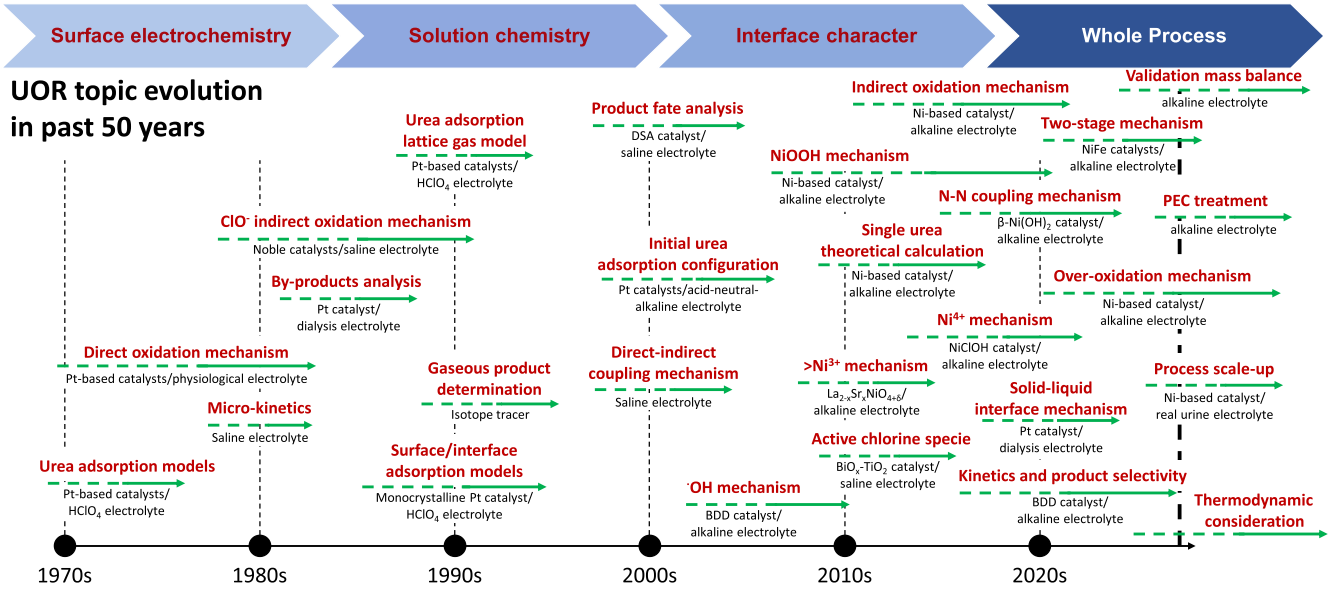

Fig. 43. Topic evolution on EC urea oxidation in the past 50 years.
(a) Adapted and updated from [35]. (b) Copyright (2022), with permission from John Wiley and Sons.

consequently the cost of the urea/NH_3 effluent treatment, as well as H_2 production.

Other products different than N_2 have been very recently identified from UOR ($^-$OCN, NO_2^- and NH_3) and AOR ($NO_2^-$and NO_3^-) and the corresponding mechanisms have been proposed. However, there is not an electrochemical pathway describing the NH_3 production during UOR. Moreover, both UOR and AOR do not follow Levich equation in RDE studies at high rotation speeds, which demonstrates the relevant role in the electrocatalytic activity of additional factors besides reactant mass-transfer such as for instance, *(i)* variations in the local pH at the electrode surface due to the OH^- consumption, *(ii)* slow UOR/AOR kinetics on some catalysts, leading to an overall reaction rate that is constantly governed by a combination of kinetics and mass transport rate, *(iii)* a competition of the indirect UOR pathway (between chemical reaction and NiOOH regeneration), and *(iv)* intermediate adsorptions on porous layer of nickel oxides. Nowadays, directing UOR selectivity towards specific products such as N_2 represents one of the most relevant trends in that research field. This purpose requires product detection and mechanistic comprehension to avoid overoxidized N-compounds such as NO_2^- and NO_3^-. Novel strategies were implemented to improve the N_2 production rate based on *(i)* increasing the residence time of urea within the diffusion layer at the nickel electrode and (ii) adding co-metal catalysts.

Some wastewater decontamination processes are based on the coupling of photo- to electrochemical methods (photo-assisted processes), but no PEC method devoted to the treatment of a urine effluent has been reported yet. The available literature is poor concerning both photo-assisted UOR and AOR, which represents a lot of potential as a future research field to be developed. For this reason, this article reviews PEC processes developed in other application fields that exhibit as a common feature, the generation of H_2 (mainly organic pollutants removal and water splitting). From this, one can conclude that strong research efforts are still necessary to develop an efficient and scalable photo-assisted urine valorization treatment in a PECR. The optimization of various parameters is crucial for the ideal configuration of the PECR. Notably, selecting the most effective PECR design—be it simple cubic, cylindrical, or filter-press—requires consideration of how geometry impacts both transport phenomena and radiative transfer. An example is a tubular reactor encased by a solar concentrator, utilizing fiber optics to introduce light directly into the reactor core, which helps to avoid most limitations. Furthermore, while most PECRs are designed with a single electrochemical cell to facilitate lighting a single photoanode, illuminating a multicell stack remains a challenge. The electrode design is equally critical, with the photoanode requiring enhancements in light absorption, reductions in charge carrier recombination, and catalysis of either the UOR or AOR, while the cathode should minimize the overpotential needed for hydrogen production using cost-effective materials. Operational considerations also include choosing between batch or continuous modes, and the decision to use stirred tank or filter press reactors with internal or external light sources. Particularly for processes combining urea treatment with hydrogen production, a series of vertically arranged single plug flow reactors may be advantageous. This configuration allows efficient hydrogen gas removal, uses internal illumination, and employs an external parabolic concentrator to light the entire photoanode surface. Additionally, the choice of the illumination source—whether UV or visible light—greatly influences the material selection for the photoanode, as materials like TiO_2, which absorb UV light, are unsuitable for solar-driven PECRs. Light sources can be either natural, requiring parabolic concentrators, or artificial, such as xenon, halides, mercury lamps, or LEDs. Finally, in order to gain a better understanding of the process's scale-up potential, studies to assess the process's techno-economic and environmental footprint criteria should be carried out as part of the AOR/UOR (*i.e.,* already carried out for other types of effluent [241,242]).

To summarize, the findings of this research illuminate the EC and PEC treatment of human urine, thereby paving the way for groundbreaking advancements in waste treatment technologies. Furthermore, this study facilitates the recuperation of valuable materials, aligning with the principles of a circular economy. This contributes significantly to enhancing the sustainability and efficiency of waste management practices, ultimately diminishing the environmental impact associated with these processes.

Future perspective developments should point towards photo-assisted urine electrolysis. In addition to this, novel types of electrocatalysts and photoelectrocatalyts exhibiting high surface area and controlling the chemical composition, as well as the crystallographic facets present at their surface, represent a novel strategy to overcome the electrode deactivation during electrolysis. Enhancing the direct electron transfer mechanism on NiOOH or other catalyst, where no NiOOH catalyst regeneration is needed, represents a very interesting approach to avoid electrode deactivation by slow NiOOH catalyst

regeneration. By addressing these challenges, scalable urine electrolysis systems will be able to move from a low technology readiness level (TRL) towards a widespread water treatment technology.

CRediT authorship contribution statement

Sophia Akkari: Investigation, Formal analysis, Validation, Visualization, Writing – original draft, Writing – review & editing. **Guillaume Hopsort:** Conceptualization, Data curation, Formal analysis, Investigation, Validation, Visualization, Writing – original draft, Writing – review & editing. **Karine Groenen Serrano:** Conceptualization, Supervision, Writing – review & editing. **Karine Loubière:** Conceptualization, Supervision, Writing – review & editing. **Théodore Tzedakis:** Conceptualization, Supervision, Writing – review & editing, Funding Acquisition. **Raihana Benyahia:** Investigation, Formal analysis, Validation, Visualization. **Lamia Rebiai:** Investigation, Formal analysis, Writing – original draft. **Stéphane Bastide:** Conceptualization, Formal analysis, Validation, Writing – review & editing, Funding acquisition. **Christine Cachet-Vivier:** Conceptualization, Formal analysis, Validation, Writing – review & editing, Funding acquisition. **Vincent Vivier:** Formal analysis, Supervision, Writing – review & editing. **Melissa Lopez-Viveros:** Conceptualization, Investigation (WWTP data), Validation (WWTP data), Writing – review & editing. **Sam Azimi:** Conceptualization, Validation (WWTP data), Funding acquisition. **Carlos M. Sánchez-Sánchez:** Conceptualization, Formal analysis, Supervision, Validation, Visualization, Writing – review & editing, Funding acquisition.

Declaration of Competing Interest

The authors declare that they have no known competing financial interests or personal relationships that could have appeared to influence the work reported in this paper.

Acknowledgements

The authors acknowledge the support of the Centre National de la Recherche Scientifique (CNRS). This work was funded and supported by the Agence Nationale de la Recherche (ANR) project HYUREA [ANR-19-CE04-0009].

Data availability

Data will be made available on request.

References

[1] X. Lin, Z. Jin, S. Jiang, Z. Wang, S. Wu, K. Bei, M. Zhao, X. Zheng, Fertilizer recovery from source-separated urine by evaporation with a combined process of dehumidification and the addition of absorbent resin supplement, Water Res. 248 (2024) 120865, https://doi.org/10.1016/j.watres.2023.120865.

[2] P. Bucholtz, M. Steele, V. Tripathi, C. Graham, L. Crane, T.H. Boyer, Solar distillation of human urine to recover non-potable water and metal phosphate mineral, Water Sci. Technol. 88 (2023) 486–501, https://doi.org/10.2166/wst.2023.218.

[3] T.A. Larsen, W. Gujer, Waste design and source control lead to flexibility in wastewater management, Water Sci. Technol. 43 (2001) 309–318, https://doi.org/10.2166/wst.2001.0313.

[4] J. Wilsenach, M. van Loosdrecht, Impact of separate urine collection on wastewater treatment systems, Water Sci. Technol. J. Int. Assoc. Water Pollut. Res. 48 (2003) 103–110.

[5] J.A. Wilsenach, M.C. van Loosdrecht, Integration of processes to treat wastewater and source-separated urine, J. Environ. Eng. 132 (2006) 331–341, https://doi.org/10.1061/(ASCE)0733-9372(2006)132:3(331).

[6] J.A. Wilsenach, M.C.M. Van Loosdrecht, Effects of separate urine collection on advanced nutrient removal processes, Environ. Sci. Technol. 38 (2004) 1208–1215, https://doi.org/10.1021/es0301018.

[7] S. Azimi, V. Rocher, Energy consumption reduction in a waste water treatment plant, Water Pract. Technol. 12 (2017) 104–116, https://doi.org/10.2166/wpt.2017.006.

[8] J. Drewnowski, A. Remiszewska-Skwarek, S. Duda, G. Łagód, Aeration process in bioreactors as the main energy consumer in a wastewater treatment plant. Review of solutions and methods of process optimization, Processes 7 (2019) 311, https://doi.org/10.3390/pr7050311.

[9] M.L. Viveros, S. Azimi, E. Pichon, C. Roose-Amsaleg, A. Bize, F. Durandet, V. Rocher, Wild type and variants of SARS-COV-2 in Parisian sewage: presence in raw water and through processes in wastewater treatment plants, Environ. Sci. Pollut. Res. 29 (2022) 67442–67449, https://doi.org/10.1007/s11356-022-22665-x.

[10] U. Badeti, N.K. Pathak, F. Volpin, U. Dorji, S. Freguia, H.K. Shon, S. Phuntsho, Impact of source-separation of urine on effluent quality, energy consumption and greenhouse gas emissions of a decentralized wastewater treatment plant, Process Saf. Environ. Prot. 150 (2021) 298–304, https://doi.org/10.1016/j.psep.2021.04.022.

[11] E. Igos, M. Besson, T. Navarrete Gutiérrez, A.B. Bisinella de Faria, E. Benetto, L. Barna, A. Ahmadi, M. Spérandio, Assessment of environmental impacts and operational costs of the implementation of an innovative source-separated urine treatment, Water Res. 126 (2017) 50–59, https://doi.org/10.1016/j.watres.2017.09.016.

[12] M. Maurer, W. Pronk, T.A. Larsen, Treatment processes for source-separated urine, Water Res. 40 (2006) 3151–3166, https://doi.org/10.1016/j.watres.2006.07.012.

[13] T.A. Larsen, M.E. Riechmann, K.M. Udert, State of the art of urine treatment technologies: a critical review, Water Res. X 13 (2021) 100114, https://doi.org/10.1016/j.wroa.2021.100114.

[14] S.P. Hilton, G.A. Keoleian, G.T. Daigger, B. Zhou, N.G. Love, Life cycle assessment of urine diversion and conversion to fertilizer products at the city scale, Environ. Sci. Technol. 55 (2021) 593–603, https://doi.org/10.1021/acs.est.0c04195.

[15] Y. Qin, J.M.S. Cabral, Review properties and applications of urease, Biocatal. Biotransformat. 20 (2002) 1–14, https://doi.org/10.1080/10242420210154.

[16] J.J. Sigurdarson, S. Svane, H. Karring, The molecular processes of urea hydrolysis in relation to ammonia emissions from agriculture, Rev. Environ. Sci. Biotechnol. 17 (2018) 241–258, https://doi.org/10.1007/s11157-018-9466-1.

[17] B. Krajewska, Ureases I. Functional, catalytic and kinetic properties: a review, J. Mol. Catal. B Enzym. 59 (2009) 9–21, https://doi.org/10.1016/j.molcatb.2009.01.003.

[18] L. Mazzei, M. Cianci, S. Benini, S. Ciurli, The structure of the elusive urease–urea complex unveils the mechanism of a paradigmatic nickel-dependent enzyme, Angew. Chem. Int. Ed. 58 (2019) 7415–7419, https://doi.org/10.1002/anie.201903565.

[19] M.E. Lilov, P.P. Kirilov, Decomposition of 8mol·L−1 urea solution at 298.15K, J. Solut. Chem. 47 (2018) 930–938, https://doi.org/10.1007/s10953-018-0762-8.

[20] J.R. Marier, D. Rose, Determination of cyanate, and a study of its accumulation in aqueous solutions of urea, Anal. Biochem. 7 (1964) 304–314, https://doi.org/10.1016/0003-2697(64)90135-6.

[21] K.M. Udert, T.A. Larsen, W. Gujer, Biologically induced precipitation in urine-collecting systems, Water Sci. Technol. Water Supply 3 (2003) 71–78, https://doi.org/10.1016/S0043-1354(03)00065-4.

[22] K.M. Udert, T.A. Larsen, M. Biebow, W. Gujer, Urea hydrolysis and precipitation dynamics in a urine-collecting system, Water Res. 37 (2003) 2571–2582, https://doi.org/10.1016/S0043-1354(03)00065-4.

[23] S. Chutipongtanate, V. Thongboonkerd, Systematic comparisons of artificial urine formulas for in vitro cellular study, Anal. Biochem. 402 (2010) 110–112, https://doi.org/10.1016/j.ab.2010.03.031.

[24] S. Bouatra, F. Aziat, R. Mandal, A.C. Guo, M.R. Wilson, C. Knox, T.C. Bjorndahl, R. Krishnamurthy, F. Saleem, P. Liu, Z.T. Dame, J. Poelzer, J. Huynh, F.S. Yallou, N. Psychogios, E. Dong, R. Bogumil, C. Roehring, D.S. Wishart, The human urine metabolome, PLOS ONE 8 (2013) e73076, https://doi.org/10.1371/journal.pone.0073076.

[25] T.M.P. Martin, F. Esculier, F. Levavasseur, S. Houot, Human urine-based fertilizers: a review, Crit. Rev. Environ. Sci. Technol. 52 (2020) 890–936, https://doi.org/10.1080/10643389.2020.1838214.

[26] D.G. Randall, M. Krähenbühl, I. Köpping, T.A. Larsen, K.M. Udert, A novel approach for stabilizing fresh urine by calcium hydroxide addition, Water Res. 95 (2016) 361–369, https://doi.org/10.1016/j.watres.2016.03.007.

[27] J. De Paepe, L. De Pryck, A.R.D. Verliefde, K. Rabaey, P. Clauwaert, Electrochemically induced precipitation enables fresh urine stabilization and facilitates source separation, Environ. Sci. Technol. 54 (2020) 3618–3627, https://doi.org/10.1021/acs.est.9b06804.

[28] E. Urbańczyk, M. Sowa, W. Simka, Urea removal from aqueous solutions—a review, J. Appl. Electrochem. 46 (2016) 1011–1029, https://doi.org/10.1007/s10800-016-0993-6.

[29] Z. Cui, M.A. Marx, M.N. Tegomoh, A.C. Co, A guide to evaluate electrolyte purity for CO_2 reduction studies, ACS Energy Lett. 8 (2023) 5201–5205, https://doi.org/10.1021/acsenergylett.3c02343.

[30] C.S. Santana, E. Gjonaj, A.C. Garcia, Effect of iron impurities on the electrochemical oxidation of glycerol on Ni(OH) $_2$ /NiOOH electrodes, ChemElectroChem 11 (2024) e202300570, https://doi.org/10.1002/celc.202300570.

[31] E.T. Sayed, T. Eisa, H.O. Mohamed, M.A. Abdelkareem, A. Allagui, H. Alawadhi, K.-J. Chae, Direct urea fuel cells: challenges and opportunities, J. Power Sources 417 (2019) 159–175, https://doi.org/10.1016/j.jpowsour.2018.12.024.

[32] K. Ye, G. Wang, D. Cao, G. Wang, Recent advances in the electro-oxidation of urea for direct urea fuel cell and urea electrolysis, Top. Curr. Chem. 376 (2018) 42, https://doi.org/10.1007/s41061-018-0219-y.

[33] R.K. Singh, K. Rajavelu, M. Montag, A. Schechter, Advances in catalytic electrooxidation of urea: a review, Energy Technol. 9 (2021) 2100017, https://doi.org/10.1002/ente.202100017.

[34] X. Hu, J. Zhu, J. Li, Q. Wu, Urea electrooxidation: current development and understanding of Ni-based catalysts, ChemElectroChem 7 (2020) 3211–3228, https://doi.org/10.1002/celc.202000404.

[35] X. Wang, J. Li, Y. Duan, J. Li, H. Wang, X. Yang, M. Gong, Electrochemical urea oxidation in different environment: from mechanism to devices, ChemCatChem 14 (2022), https://doi.org/10.1002/cctc.202101906.

[36] X. Gao, S. Zhang, P. Wang, M. Jaroniec, Y. Zheng, S.-Z. Qiao, Urea catalytic oxidation for energy and environmental applications, Chem. Soc. Rev. 53 (2024) 1552–1591, https://doi.org/10.1039/D3CS00963G.

[37] L. Rebiai, D. Muller-Bouvet, R. Benyahia, E. Torralba, M.L. Viveros, V. Rocher, S. Azimi, C. Cachet-Vivier, S. Bastide, Photoelectrocatalytic conversion of urea under solar illumination using Ni decorated Ti-Fe2O3 electrodes, Electrochim. Acta 438 (2023) 141516, https://doi.org/10.1016/j.electacta.2022.141516.

[38] J. Dabboussi, R. Abdallah, L. Santinacci, S. Zanna, A. Vacher, V. Dorcet, S. Fryars, D. Floner, G. Loget, Solar-assisted urea oxidation at silicon photoanodes promoted by an amorphous and optically adaptive Ni–Mo–O catalytic layer, J. Mater. Chem. A (2022), https://doi.org/10.1039/D2TA01212J.

[39] W. Sun, M. Zhang, J. Li, C. Peng, Solar-driven catalytic urea oxidation for environmental remediation and energy recovery, ChemSusChem 15 (2022) e202201263, https://doi.org/10.1002/cssc.202201263.

[40] D. Yan, C. Mebrahtu, S. Wang, R. Palkovits, Innovative electrochemical strategies for hydrogen production: from electricity input to electricity output, Angew. Chem. Int. Ed. 62 (2023) e202214333, https://doi.org/10.1002/anie.202214333.

[41] T. Wang, X. Cao, L. Jiao, Progress in hydrogen production coupled with electrochemical oxidation of small molecules, Angew. Chem. Int. Ed. 61 (2022) e202213328, https://doi.org/10.1002/anie.202213328.

[42] A.N. Rollinson, J. Jones, V. Dupont, M.V. Twigg, Urea as a hydrogen carrier: a perspective on its potential for safe, sustainable and long-term energy supply, Energy Environ. Sci. 4 (2011) 1216, https://doi.org/10.1039/c0ee00705f.

[43] G.G. Botte, Electrolytic cells and methods for the production of ammonia and hydrogen, US8303781B2, 2012. https://patents.google.com/patent/US8303781B2/en (accessed February 6, 2024).

[44] S.J. Yao, S.K. Wolfson, B.K. Ahn, C.C. Liu, Anodic oxidation of urea and an electrochemical approach to De-ureation, Nature 241 (1973) 471–472, https://doi.org/10.1038/241471a0.

[45] R.W. Keller, S.J. Yao, J.M. Brown, S.K. Wolfson, M.V. Zeller, Electrochemical removal of urea from physiological buffer as the basis for a regenerative dialysis system, J. Electroanal. Chem. Interfacial Electrochem. 116 (1980) 469–485, https://doi.org/10.1016/S0022-0728(80)80271-3.

[46] J.F. Patzer, S.K. Wolfson, S.J. Yao, Reactor control and reaction kinetics for electrochemical urea oxidation, Chem. Eng. Sci. 45 (1990) 2777–2784, https://doi.org/10.1016/0009-2509(90)80170-J.

[47] E. Urbańczyk, M. Sowa, W. Simka, Urea removal from aqueous solutions—a review, J. Appl. Electrochem. 46 (2016) 1011–1029, https://doi.org/10.1007/s10800-016-0993-6.

[48] J. Dabboussi, R.-A. Eichel, H. Kungl, R. Abdallah, G. Loget, The rebirth of urea oxidation reaction for power-to-X and beyond, Curr. Opin. Electrochem. (2024) 101468, https://doi.org/10.1016/j.coelec.2024.101468.

[49] E.J. Cairns, E.L. Simons, A.D. Tevebaugh, Ammonia–oxygen fuel cell, Nature 217 (1968) 780–781, https://doi.org/10.1038/217780a0.

[50] D.W. McKee, A.J. Scarpellino, I.F. Danzig, M.S. Pak, Improved electrocatalysts for ammonia fuel cell anodes, J. Electrochem. Soc. 116 (1969) 562, https://doi.org/10.1149/1.2411963.

[51] E.L. Simons, E.J. Cairns, D.J. Surd, The performance of direct ammonia fuel cells, J. Electrochem. Soc. 116 (1969) 556, https://doi.org/10.1149/1.2411961.

[52] K.V. Kordesch, 25 years of fuel cell development (1951–1976), J. Electrochem. Soc. 125 (1978) 77C, https://doi.org/10.1149/1.2131782.

[53] W. Simka, J. Piotrowski, A. Robak, G. Nawrat, Electrochemical treatment of aqueous solutions containing urea, J. Appl. Electrochem. 39 (2009) 1137–1143, https://doi.org/10.1007/s10800-008-9771-4.

[54] H. Li, Q. Yu, B. Yang, Z. Li, L. Lei, Electro-catalytic oxidation of artificial human urine by using BDD and IrO2 electrodes, J. Electroanal. Chem. 738 (2015) 14–19, https://doi.org/10.1016/j.jelechem.2014.11.018.

[55] K.M. Udert, T.A. Larsen, W. Gujer, Fate of major compounds in source-separated urine, Water Sci. Technol. J. Int. Assoc. Water Pollut. Res. 54 (2006) 413–420, https://doi.org/10.2166/wst.2006.921.

[56] V. Amstutz, A. Katsaounis, A. Kapalka, C. Comninellis, K.M. Udert, Effects of carbonate on the electrolytic removal of ammonia and urea from urine with thermally prepared IrO2 electrodes, J. Appl. Electrochem. 42 (2012) 787–795, https://doi.org/10.1007/s10800-012-0444-y.

[57] H. Zöllig, C. Fritzsche, E. Morgenroth, K.M. Udert, Direct electrochemical oxidation of ammonia on graphite as a treatment option for stored source-separated urine, Water Res 69 (2015) 284–294, https://doi.org/10.1016/j.watres.2014.11.031.

[58] H. Zöllig, A. Remmele, E. Morgenroth, K.M. Udert, Removal rates and energy demand of the electrochemical oxidation of ammonia and organic substances in real stored urine, Environ. Sci. Water Res. Technol. 3 (2017) 480–491, https://doi.org/10.1039/C7EW00014F.

[59] X. Jiang, D. Ying, X. Liu, M. Liu, S. Zhou, C. Guo, G. Zhao, Y. Wang, J. Jia, Identification of the role of Cu site in Ni-Cu hydroxide for robust and high selective electrochemical ammonia oxidation to nitrite, Electrochim. Acta 345 (2020) 136157, https://doi.org/10.1016/j.electacta.2020.136157.

[60] D. Chun, C.-R. Lim, H.-S. Lee, W.-S. Yoon, T.-K. Lee, D.K. Kim, Electrochemical treatment of urine by using Ti/IrO2/TiO2 electrode, J. Water Process Eng. 26 (2018) 1–9, https://doi.org/10.1016/j.jwpe.2018.06.004.

[61] S. Garcia-Segura, E. Mostafa, H. Baltruschat, Electrogeneration of inorganic chloramines on boron-doped diamond anodes during electrochemical oxidation of ammonium chloride, urea and synthetic urine matrix, Water Res. 160 (2019) 107–117, https://doi.org/10.1016/j.watres.2019.05.046.

[62] X. Tang, I. Arif, P. Diao, Monitoring the chlorine evolution reaction during electrochemical alkaline seawater splitting, J. Electroanal. Chem. 942 (2023) 117569, https://doi.org/10.1016/j.jelechem.2023.117569.

[63] W. Tong, M. Forster, F. Dionigi, S. Dresp, R. Sadeghi Erami, P. Strasser, A. J. Cowan, P. Farràs, Electrolysis of low-grade and saline surface water, Nat. Energy 5 (2020) 367–377, https://doi.org/10.1038/s41560-020-0550-8.

[64] Y. Hong, Z. Zhu, W. Liao, Z. Yan, C. Feng, D. Xu, Freshwater water-quality criteria for chloride and guidance for the revision of the water-quality standard in China, Int. J. Environ. Res. Public. Health 20 (2023) 2875, https://doi.org/10.3390/ijerph20042875.

[65] G. Hopsort, L. Latapie, K. Groenen Serrano, K. Loubière, T. Tzedakis, Deciphering the human urine matrix: a new approach to simultaneously quantify the main ions and organic compounds by ion chromatography/mass spectrometry (IC-MS), Anal. Bioanal. Chem. 415 (2023) 5337–5352, https://doi.org/10.1007/s00216-023-04808-2.

[66] H.J. Song, H. Yoon, B. Ju, D.-Y. Lee, D.-W. Kim, Electrocatalytic selective oxygen evolution of carbon-coated $Na_2Co_{1-x}Fe_xP_2O_7$ nanoparticles for alkaline seawater electrolysis, ACS Catal. 10 (2020) 702–709, https://doi.org/10.1021/acscatal.9b04231.

[67] G. Bahuguna, F. Patolsky, Routes to avoiding chlorine evolution in seawater electrolysis: recent perspective and future directions, ACS Mater. Lett. 6 (2024) 3202–3217, https://doi.org/10.1021/acsmaterialslett.4c00409.

[68] L. Zhao, X. Li, J. Yu, W. Zhou, Design strategy of corrosion-resistant electrodes for seawater electrolysis, Materials 16 (2023) 2709, https://doi.org/10.3390/ma16072709.

[69] H.G. Oswin, M. Salomon, The anodic oxidation of ammonia at platinum black electrodes in aqueous koh electrolyte, Can. J. Chem. 41 (1963) 1686–1694, https://doi.org/10.1139/v63-243.

[70] H. Gerischer, A. Mauerer, Untersuchungen zuranodischen oxid. vonammoniak platin-elektroden (1969) 13.

[71] L.A. Diaz, A. Valenzuela-Muñiz, M. Muthuvel, G.G. Botte, Analysis of ammonia electro-oxidation kinetics using a rotating disk electrode, Electrochim. Acta 89 (2013) 413–421, https://doi.org/10.1016/j.electacta.2012.11.064.

[72] A. Kapałka, A. Cally, S. Neodo, C. Comninellis, M. Wächter, K.M. Udert, Electrochemical behavior of ammonia at Ni/Ni(OH)2 electrode, Electrochem. Commun. 12 (2010) 18–21, https://doi.org/10.1016/j.elecom.2009.10.026.

[73] Y.-J. Shih, Y.-H. Huang, C.P. Huang, Electrocatalytic ammonia oxidation over a nickel foam electrode: Role of Ni(OH)2(s)-NiOOH(s) nanocatalysts, Electrochim. Acta 263 (2018) 261–271, https://doi.org/10.1016/j.electacta.2018.01.045.

[74] P. Wang, X. Bai, H. Jin, X. Gao, K. Davey, Y. Zheng, Y. Jiao, S. Qiao, Directed urea-to-nitrite electrooxidation via tuning intermediate adsorption on Co, Ge Co-doped Ni sites, Adv. Funct. Mater. 33 (2023) 2300687, https://doi.org/10.1002/adfm.202300687.

[75] G. Zhan, L. Hu, H. Li, J. Dai, L. Zhao, Q. Zheng, X. Zou, Y. Shi, J. Wang, W. Hou, Y. Yao, L. Zhang, Highly selective urea electrooxidation coupled with efficient hydrogen evolution, Nat. Commun. 15 (2024) 5918, https://doi.org/10.1038/s41467-024-50343-8.

[76] E. Moran, C. Cattaneo, H. Mishima, B.A. López de Mishima, S.P. Silvetti, J. L. Rodriguez, E. Pastor, Ammonia oxidation on electrodeposited Pt–Ir alloys, J. Solid State Electrochem. 12 (2008) 583–589, https://doi.org/10.1007/s10008-007-0407-0.

[77] J.C.M. Silva, S. Ntais, É. Teixeira-Neto, E.V. Spinacé, X. Cui, A.O. Neto, E. A. Baranova, Evaluation of carbon supported platinum–ruthenium nanoparticles for ammonia electro-oxidation: combined fuel cell and electrochemical approach, Int. J. Hydrog. Energy 42 (2017) 193–201, https://doi.org/10.1016/j.ijhydene.2016.09.135.

[78] L. Wang, S. Zhu, N. Marinkovic, S. Kattel, M. Shao, B. Yang, J.G. Chen, Insight into the synergistic effect between nickel and tungsten carbide for catalyzing urea electrooxidation in alkaline electrolyte, Appl. Catal. B Environ. 232 (2018) 365–370, https://doi.org/10.1016/j.apcatb.2018.03.064.

[79] S.W. Tatarchuk, J.J. Medvedev, F. Li, Y. Tobolovskaya, A. Klinkova, Nickel-catalyzed urea electrolysis: from nitrite and cyanate as major products to nitrogen evolution, Angew. Chem. Int. Ed. 61 (2022) e202209839, https://doi.org/10.1002/anie.202209839.

[80] J. Li, J. Li, T. Liu, L. Chen, Y. Li, H. Wang, X. Chen, M. Gong, Z. Liu, X. Yang, Deciphering and suppressing over-oxidized nitrogen in nickel-catalyzed urea electrolysis, Angew. Chem. Int. Ed. 60 (2021) 26656–26662, https://doi.org/10.1002/anie.202107886.

[81] Z. Shen, Y. Qi, W. Ge, H. Jiang, C. Li, Highly selective electrooxidation of urea to nitrogen on copper/nickel boride interface under alkaline condition, Ind. Eng. Chem. Res. 62 (2023) 8736–8743, https://doi.org/10.1021/acs.iecr.3c00802.

[82] X. Gao, X. Bai, P. Wang, Y. Jiao, K. Davey, Y. Zheng, S.-Z. Qiao, Boosting urea electrooxidation on oxyanion-engineered nickel sites via inhibited water oxidation, Nat. Commun. 14 (2023) 5842, https://doi.org/10.1038/s41467-023-41588-w.

[83] K. Nagita, Y. Yuhara, K. Fujii, Y. Katayama, M. Nakayama, Ni- and Cu-co-intercalated layered manganese oxide for highly efficient electro-oxidation of ammonia selective to nitrogen, ACS Appl. Mater. Interfaces 13 (2021) 28098–28107, https://doi.org/10.1021/acsami.1c04422.

[84] K. Carpenter, Design, Development, and Operation of an Electrochemical Urea Removal Reactor for the Application of Portable Dialysis, University of Washington, 2021. ⟨http://hdl.handle.net/1773/47016⟩.

[85] K. Carpenter, E.M. Stuve, Electrooxidation of urea and creatinine on nickel foam-based electrocatalysts, J. Appl. Electrochem. 51 (2021) 945–957, https://doi.org/10.1007/s10800-021-01545-1.

[86] G. Hopsort, E. Piguet, L. Latapie, K. Groenen Serrano, K. Loubière, T. Tzedakis, Towards an industrial perspective for urea-to-hydrogen valorization by electro-oxidation on nickel(III): real effluents and pilot-scale proof of concept, Electrochim. Acta 479 (2024) 143886, https://doi.org/10.1016/j.electacta.2024.143886.

[87] B. Zhu, Z. Liang, R. Zou, Designing advanced catalysts for energy conversion based on urea oxidation reaction, Small 16 (2020) 1906133, https://doi.org/10.1002/smll.201906133.

[88] R.P. Forslund, J.T. Mefford, W.G. Hardin, C.T. Alexander, K.P. Johnston, K. J. Stevenson, Nanostructured LaNiO3 perovskite electrocatalyst for enhanced urea oxidation, ACS Catal. 6 (2016) 5044–5051, https://doi.org/10.1021/acscatal.6b00487.

[89] F. Guo, K. Ye, M. Du, X. Huang, K. Cheng, G. Wang, D. Cao, Electrochemical impedance analysis of urea electro-oxidation mechanism on nickel catalyst in alkaline medium, Electrochim. Acta 210 (2016) 474–482, https://doi.org/10.1016/j.electacta.2016.05.149.

[90] F. Lu, G.G. Botte, Electrochemically induced conversion of urea to ammonia, ECS Electrochem. Lett. 4 (2015) E5–E7, https://doi.org/10.1149/2.0041510eel.

[91] F. Lu, G.G. Botte, Understanding the electrochemically induced conversion of urea to ammonia using nickel based catalysts, Electrochim. Acta 246 (2017) 564–571, https://doi.org/10.1016/j.electacta.2017.06.055.

[92] R.C. Warner, The kinetics of the hydrolysis of urea and of arginine, J. Biol. Chem. 142 (1942) 705–723, https://doi.org/10.1016/S0021-9258(18)45072-7.

[93] D.A. Daramola, D. Singh, G.G. Botte, Dissociation rates of urea in the presence of NiOOH catalyst: a DFT analysis, J. Phys. Chem. A 114 (2010) 11513–11521, https://doi.org/10.1021/jp105159t.

[94] S. Akkari, V. Vivier, C.M. Sánchez-Sánchez, Urea electro-oxidation byproducts impact on NiO/NiOOH anode performance studied by operando electrochemical impedance spectroscopy, Electrochim. Acta 474 (2024) 143526, https://doi.org/10.1016/j.electacta.2023.143526.

[95] A. Tewari, V. Sambhy, M. Urquidi Macdonald, A. Sen, Quantification of carbon dioxide poisoning in air breathing alkaline fuel cells, J. Power Sources 153 (2006) 1–10, https://doi.org/10.1016/j.jpowsour.2005.03.192.

[96] F. Guo, K. Ye, K. Cheng, G. Wang, D. Cao, Preparation of nickel nanowire arrays electrode for urea electro-oxidation in alkaline medium, J. Power Sources 278 (2015) 562–568, https://doi.org/10.1016/j.jpowsour.2014.12.125.

[97] R. Ojani, E. Hasheminejad, J.B. Raoof, Hydrogen evolution assisted electrodeposition of bimetallic 3D nano/micro-porous PtPd films and their electrocatalytic performance, Int. J. Hydrog. Energy 39 (2014) 8194–8203, https://doi.org/10.1016/j.ijhydene.2014.03.162.

[98] Q. Zhang, F.M.D. Kazim, S. Ma, K. Qu, M. Li, Y. Wang, H. Hu, W. Cai, Z. Yang, Nitrogen dopants in nickel nanoparticles embedded carbon nanotubes promote overall urea oxidation, Appl. Catal. B Environ. 280 (2021) 119436, https://doi.org/10.1016/j.apcatb.2020.119436.

[99] F. Lu, G.G. Botte, Ammonia generation via a graphene-coated nickel catalyst, Coatings 7 (2017) 72, https://doi.org/10.3390/coatings7060072.

[100] B.K. Boggs, R.L. King, G.G. Botte, Urea electrolysis: direct hydrogen production from urine, Chem. Commun. (2009) 4859–4861, https://doi.org/10.1039/B905974A.

[101] P. Mirzaei, S. Bastide, A. Dassy, R. Bensimon, J. Bourgon, A. Aghajani, C. Zlotea, D. Muller-Bouvet, C. Cachet-Vivier, Electrochemical oxidation of urea on nickel-rhodium nanoparticles/carbon composites, Electrochim. Acta 297 (2019) 715–724, https://doi.org/10.1016/j.electacta.2018.11.205.

[102] D. Yang, L. Yang, L. Zhong, X. Yu, L. Feng, Urea electro-oxidation efficiently catalyzed by nickel-molybdenum oxide nanorods, Electrochim. Acta 295 (2019) 524–531, https://doi.org/10.1016/j.electacta.2018.10.190.

[103] W. Xu, Z. Wu, S. Tao, Urea-based fuel cells and electrocatalysts for urea oxidation, Energy Technol. 4 (2016) 1329–1337, https://doi.org/10.1002/ente.201600185.

[104] A.J. Bard, J. Jordan, R. Parsons. Standard Potentials in Aqueous Solution, 1st ed., M. Dekker, New York, 1985.

[105] N.M. Adli, H. Zhang, S. Mukherjee, G. Wu, Review—ammonia oxidation electrocatalysis for hydrogen generation and fuel cells, J. Electrochem. Soc. 165 (2018) J3130, https://doi.org/10.1149/2.0191815jes.

[106] V.S. Protsenko, Thermodynamic aspects of urea oxidation reaction in the context of hydrogen production by electrolysis, Int. J. Hydrog. Energy 48 (2023) 24207–24211, https://doi.org/10.1016/j.ijhydene.2023.03.295.

[107] V.S. Protsenko, L.S. Bobrova, T.E. Butyrina, O.D. Sukhatskyi, Thermodynamics of electrochemical urea oxidation reaction coupled with cathodic hydrogen evolution reaction in an alkaline solution: effect of carbonate formation, Int. J. Hydrog. Energy 59 (2024) 354–358, https://doi.org/10.1016/j.ijhydene.2024.02.006.

[108] R. Lan, S. Tao, Preparation of nano-sized nickel as anode catalyst for direct urea and urine fuel cells, J. Power Sources 196 (2011) 5021–5026, https://doi.org/10.1016/j.jpowsour.2011.02.015.

[109] R.H. Tammam, M.M. Saleh, On the electrocatalytic urea oxidation on nickel oxide nanoparticles modified glassy carbon electrode, J. Electroanal. Chem. 794 (2017) 189–196, https://doi.org/10.1016/j.jelechem.2017.04.023.

[110] R.L. King, G.G. Botte, Investigation of multi-metal catalysts for stable hydrogen production via urea electrolysis, J. Power Sources 196 (2011) 9579–9584, https://doi.org/10.1016/j.jpowsour.2011.06.079.

[111] W.H. Yun, G. Das, B. Kim, B.J. Park, H.H. Yoon, Y.S. Yoon, Ni–Fe phosphide deposited carbon felt as free-standing bifunctional catalyst electrode for urea electrolysis, Sci. Rep. 11 (2021) 22003, https://doi.org/10.1038/s41598-021-01383-3.

[112] W. Shi, R. Ding, X. Li, Q. Xu, E. Liu, Enhanced performance and electrocatalytic kinetics of Ni-Mo/graphene nanocatalysts towards alkaline urea oxidation reaction, Electrochim. Acta 242 (2017) 247–259, https://doi.org/10.1016/j.electacta.2017.05.002.

[113] X. Sun, R. Ding, Recent progress with electrocatalysts for urea electrolysis in alkaline media for energy-saving hydrogen production, Catal. Sci. Technol. 10 (2020) 1567–1581, https://doi.org/10.1039/C9CY02618E.

[114] R. Wang, H. Liu, K. Zhang, G. Zhang, L. Huachun, J. Qu, Ni(II)/Ni(III) redox couple endows Ni foam-supported Ni2P with excellent capability for direct ammonia oxidation, Chem. Eng. J. (2021), https://doi.org/10.1016/J.CEJ.2020.126795.

[115] K. Siddharth, Y. Chan, L. Wang, M. Shao, Ammonia electro-oxidation reaction: Recent development in mechanistic understanding and electrocatalyst design, Curr. Opin. Electrochem. 9 (2018) 151–157, https://doi.org/10.1016/j.coelec.2018.03.011.

[116] K. Dhaka, M.C. Toroker, Revealing the conducting character of the β-NiOOH catalyst through defect chemistry, J. Phys. Chem. C. 123 (2019) 18895–18904, https://doi.org/10.1021/acs.jpcc.9b01750.

[117] L. Li, J. Xu, J. Lei, J. Zhang, F. McLarnon, Z. Wei, N. Li, F. Pan, A one-step, cost-effective green method to in situ fabricate Ni(OH) $_2$ hexagonal platelets on Ni foam as binder-free supercapacitor electrode materials, J. Mater. Chem. A 3 (2015) 1953–1960, https://doi.org/10.1039/C4TA05156D.

[118] X. Xiong, D. Ding, D. Chen, G. Waller, Y. Bu, Z. Wang, M. Liu, Three-dimensional ultrathin Ni(OH)2 nanosheets grown on nickel foam for high-performance supercapacitors, Nano Energy 11 (2015) 154–161, https://doi.org/10.1016/j.nanoen.2014.10.029.

[119] B.J. Hernlem, Electrolytic destruction of urea in dilute chloride solution using DSA electrodes in a recycled batch cell, Water Res 39 (2005) 2245–2252, https://doi.org/10.1016/j.watres.2005.04.018.

[120] V. Grinval'd, G. Leshchinskii, V. Rodin, S. Strelkov, A. Yakovleva, Development and testing of a unit for electrochemical oxidation of products of hemodialysis, Biomed. Eng. 37 (2003) 67–72, https://doi.org/10.1023/A:1024727513884.

[121] L. Szpyrkowicz, C. Juzzolino, S. Daniele, M.D.D. Faveri, Electrochemical destruction of thiourea dioxide in an undivided parallel plate electrodes batch reactor, Catal. Today 66 (2001) 519–527, https://doi.org/10.1016/S0920-5861(00)00624-6.

[122] S.J. Yao, S.K. Wolfson, J.M. Tokarsky, B.K. Ahn, De-ureation by electrochemical oxidation, Bioelectrochem. Bioenerg. 1 (1974) 180–186, https://doi.org/10.1016/0302-4598(74)85019-1.

[123] J.F. Patzer, S.J. Yao, S.K. Wolfson, R. Ruppel-Kerr, Urea oxidation kinetics via cyclic voltammetry: application to regenerative hemodialysis, J. Electroanal. Chem. Interfacial Electrochem. 276 (1989) 341–353, https://doi.org/10.1016/0022-0728(89)87276-6.

[124] V. Vedharathinam, G.G. Botte, Understanding the electro-catalytic oxidation mechanism of urea on nickel electrodes in alkaline medium, Electrochim. Acta 81 (2012) 292–300, https://doi.org/10.1016/j.electacta.2012.07.007.

[125] W. Yan, D. Wang, G.G. Botte, Electrochemical decomposition of urea with Ni-based catalysts, Appl. Catal. B Environ. 127 (2012) 221–226, https://doi.org/10.1016/j.apcatb.2012.08.022.

[126] D. Wang, W. Yan, S.H. Vijapur, G.G. Botte, Enhanced electrocatalytic oxidation of urea based on nickel hydroxide nanoribbons, J. Power Sources 217 (2012) 498–502, https://doi.org/10.1016/j.jpowsour.2012.06.029.

[127] X. Zhu, X. Dou, J. Dai, X. An, Y. Guo, L. Zhang, S. Tao, J. Zhao, W. Chu, X.C. Zeng, C. Wu, Y. Xie, Metallic nickel hydroxide nanosheets give superior electrocatalytic oxidation of urea for fuel cells, Angew. Chem. Int. Ed. 55 (2016) 12465–12469, https://doi.org/10.1002/anie.201606313.

[128] H. Wang, L. Lu, P. Subramanian, S. Ji, P. Kannan, Co, Fe-ions intercalated Ni(OH) 2 network-like nanosheet arrays as highly efficient non-noble catalyst for electro-oxidation of urea, Int. J. Hydrog. Energy 46 (2021) 34318–34332, https://doi.org/10.1016/j.ijhydene.2021.08.022.

[129] N.A.M. Barakat, M.H. El-Newehy, A.S. Yasin, Z.K. Ghouri, S.S. Al-Deyab, Ni&Mn nanoparticles-decorated carbon nanofibers as effective electrocatalyst for urea oxidation, Appl. Catal. Gen. 510 (2016) 180–188, https://doi.org/10.1016/j.apcata.2015.11.015.

[130] C. Carlesi Jara, S. Di Giulio, D. Fino, P. Spinelli, Combined direct and indirect electroxidation of urea containing water, J. Appl. Electrochem. 38 (2008) 915–922, https://doi.org/10.1007/s10800-008-9496-4.

[131] V. Vedharathinam, G.G. Botte, Direct evidence of the mechanism for the electro-oxidation of urea on Ni(OH)2 catalyst in alkaline medium, Electrochim. Acta 108 (2013) 660–665, https://doi.org/10.1016/j.electacta.2013.06.137.

[132] M. Fleischmann, K. Korinek, D. Pletcher, The oxidation of organic compounds at a nickel anode in alkaline solution, J. Electroanal. Chem. Interfacial Electrochem. 31 (1971) 39–49, https://doi.org/10.1016/S0022-0728(71)80040-2.

[133] M. Fleischmann, K. Korinek, D. Pletcher, The kinetics and mechanism of the oxidation of amines and alcohols at oxide-covered nickel, silver, copper, and cobalt electrodes, J. Chem. Soc. Perkin Trans. 2 (1972) 1396–1403, https://doi.org/10.1039/P29720001396.

[134] Y. Miao, L. Ouyang, S. Zhou, L. Xu, Z. Yang, M. Xiao, R. Ouyang, Electrocatalysis and electroanalysis of nickel, its oxides, hydroxides and oxyhydroxides toward small molecules, Biosens. Bioelectron. 53 (2014) 428–439, https://doi.org/10.1016/j.bios.2013.10.008.

[135] M.A. Abdelkareem, E.T. Sayed, H.O. Mohamed, M. Obaid, H. Rezk, K.J. Chae, Nonprecious anodic catalysts for low-molecular-hydrocarbon fuel cells: theoretical consideration and current progress, Prog. Energy Combust. Sci. 77 (2019) 100805, https://doi.org/10.1016/j.pecs.2019.100805.
[136] G. Hopsort, D.P.D. Carmo, L. Latapie, K. Loubière, K.G. Serrano, T. Tzedakis, Progress toward a better understanding of the urea oxidation by electromediation of Ni(III)/Ni(II) system in alkaline media, Electrochim. Acta 442 (2023) 141898, https://doi.org/10.1016/j.electacta.2023.141898.
[137] D. Wang, G.G. Botte, In Situ X-ray diffraction study of urea electrolysis on nickel catalysts, ECS Electrochem. Lett. 3 (2014) H29–H32, https://doi.org/10.1149/2.0031409eel.
[138] N.N. Rao, C. Alex, M. Mukherjee, S. Roy, A. Tayal, A. Datta, N.S. John, Evidence for exclusive direct mechanism of urea electro-oxidation driven by in situ-generated resilient active species on a rare-earth nickelate, ACS Catal. 14 (2024) 981–993, https://doi.org/10.1021/acscatal.3c04967.
[139] C. Alex, M.S. Naduvil Kovilakath, N.N. Rao, C. Sathiskumar, A. Tayal, L. Meesala, P. Kumar, N.S. John, In-situ generated Ni(OH)2 on chemically activated spent catalyst sustains urea electro-oxidation in extensive alkaline conditions, Int. J. Hydrog. Energy 59 (2024) 390–399, https://doi.org/10.1016/j.ijhydene.2024.01.339.
[140] K. Ye, H. Zhang, L. Zhao, X. Huang, K. Cheng, G. Wang, D. Cao, Facile preparation of three-dimensional Ni(OH)2/Ni foam anode with low cost and its application in a direct urea fuel cell, N. J. Chem. 40 (2016) 8673–8680, https://doi.org/10.1039/C6NJ01648K.
[141] G. Hopsort, L. Latapie, K. Groenen Serrano, K. Loubière, T. Tzedakis, Indirect urea electrooxidation by nickel(III) in alkaline medium: from kinetic and mechanism to reactor modeling, AIChE J 69 (2023) e18113, https://doi.org/10.1002/aic.18113.
[142] G. Wang, K. Ye, J. Shao, Y. Zhang, K. Zhu, K. Cheng, J. Yan, G. Wang, D. Cao, Porous Ni2P nanoflower supported on nickel foam as an efficient three-dimensional electrode for urea electro-oxidation in alkaline medium, Int. J. Hydrog. Energy 43 (2018) 9316–9325, https://doi.org/10.1016/j.ijhydene.2018.03.221.
[143] C. Zhong, W.B. Hu, Y.F. Cheng, Recent advances in electrocatalysts for electro-oxidation of ammonia, J. Mater. Chem. A 1 (2013) 3216–3238, https://doi.org/10.1039/C2TA00607C.
[144] Y. Kang, W. Wang, J. Li, C. Hua, S. Xue, Z. Lei, High performance PtxEu alloys as effective electrocatalysts for ammonia electro-oxidation, Int. J. Hydrog. Energy 42 (2017) 18959–18967, https://doi.org/10.1016/j.ijhydene.2017.05.216.
[145] F.J. Vidal-Iglesias, J. Solla-Gullón, P. Rodríguez, E. Herrero, V. Montiel, J. M. Feliu, A. Aldaz, Shape-dependent electrocatalysis: ammonia oxidation on platinum nanoparticles with preferential (100) surfaces, Electrochem. Commun. 6 (2004) 1080–1084, https://doi.org/10.1016/j.elecom.2004.08.010.
[146] J. Zhang, J. Feng, J. Zhu, L. Kang, L. Liu, F. Guo, J. Li, K. Li, J. Chen, W. Zong, M. Liu, R. Chen, I.P. Parkin, L. Mai, G. He, Regulating reconstruction-engineered active sites for accelerated electrocatalytic conversion of urea, Angew. Chem. Int. Ed. (2024) e202407038, https://doi.org/10.1002/anie.202407038.
[147] D. Grujicic, B. Pesic, Electrochemical and AFM study of nickel nucleation mechanisms on vitreous carbon from ammonium sulfate solutions, Electrochim. Acta 51 (2006) 2678–2690, https://doi.org/10.1016/j.electacta.2005.08.017.
[148] W. Yan, D. Wang, L.A. Diaz, G.G. Botte, Nickel nanowires as effective catalysts for urea electro-oxidation, Electrochim. Acta 134 (2014) 266–271, https://doi.org/10.1016/j.electacta.2014.03.134.
[149] D. Wang, S.H. Vijapur, Y. Wang, G.G. Botte, NiCo2O4 nanosheets grown on current collectors as binder-free electrodes for hydrogen production via urea electrolysis, Int. J. Hydrog. Energy 42 (2017) 3987–3993, https://doi.org/10.1016/j.ijhydene.2016.11.048.
[150] W. Chen, L. Xu, X. Zhu, Y. Huang, W. Zhou, D. Wang, Y. Zhou, S. Du, Q. Li, C. Xie, L. Tao, C. Dong, J. Liu, Y. Wang, R. Chen, H. Su, C. Chen, Y. Zou, Y. Li, Q. Liu, S. Wang, Unveiling the electrooxidation of urea: intramolecular coupling of the N−N bond, Angew. Chem. Int. Ed. 60 (2021) 7297–7307, https://doi.org/10.1002/anie.202015773.
[151] G. Hopsort, L. Latapie, K. Groenen Serrano, K. Loubière, T. Tzedakis, New insights into urea electro-oxidation: complete mass-balances and proof of concept with real-matrix effluent, J. Electrochem. Soc. 170 (2023) 093507, https://doi.org/10.1149/1945-7111/acf87e.
[152] N. Hales, T.J. Schmidt, E. Fabbri, Reversible and irreversible transformations of Ni-based electrocatalysts during the oxygen evolution reaction, Curr. Opin. Electrochem. 38 (2023) 101231, https://doi.org/10.1016/j.coelec.2023.101231.
[153] C. Liu, F. Yang, A. Schechter, L. Feng, Recent progress of Ni-based catalysts for methanol electrooxidation reaction in alkaline media, Adv. Sens. Energy Mater. 2 (2023) 100055, https://doi.org/10.1016/j.asems.2023.100055.
[154] A.N. Vyas, G.D. Saratale, S.D. Sartale, Recent developments in nickel based electrocatalysts for ethanol electrooxidation, Int. J. Hydrog. Energy 45 (2020) 5928–5947, https://doi.org/10.1016/j.ijhydene.2019.08.218.
[155] Y. Zhao, Y. Sun, H. Li, S. Zeng, R. Li, Q. Yao, H. Chen, Y. Zheng, K. Qu, Highly enhanced hydrazine oxidation on bifunctional Ni tailored by alloying for energy-efficient hydrogen production, J. Colloid Interface Sci. 652 (2023) 1848–1856, https://doi.org/10.1016/j.jcis.2023.09.003.
[156] H. Li, Q. Yu, X. Zhu, H. Wu, Z. Dai, L. Li, W. Zhu, S. Li, Z. Chen, V-doping and cation-vacancy engineering synergistically promote the electrocatalysis ability of NiFe-layered double hydroxides towards the oxygen evolution and urea oxidation reactions, Chem. Eng. J. 493 (2024) 152860, https://doi.org/10.1016/j.cej.2024.152860.
[157] T.X. Nguyen, Z.-Y. Wei, T.-M. Zheng, Y.-H. Su, K.-S. Chuang, J.-M. Ting, Enhancement of urea oxidation reaction in alkaline condition via heterointerface engineering, Chem. Eng. J. 496 (2024) 153841, https://doi.org/10.1016/j.cej.2024.153841.
[158] J. Tang, Z. Li, H. Jang, X. Gu, C. Sun, M.G. Kim, L. Hou, X. Liu, Local charge modulation induced the formation of high-valent nickel sites for enhanced urea electrolysis, Adv. Energy Mater. (2024) 2403004, https://doi.org/10.1002/aenm.202403004.
[159] H.J. Kim, R. Santhosh Kumar, S. Tamilarasi, S. Vijayapradeep, H. Bin Kwak, D. Jin Yoo, Elevated electrocatalytic activity of high-efficiency urea induces water electrolysis via a ruthenium nickel oxynitride electrocatalyst, Chem. Eng. J. 489 (2024) 151003, https://doi.org/10.1016/j.cej.2024.151003.
[160] N.Q. Tran, N.H. Vu, J. Yu, K.V.P. Nguyen, T.T.N. Tran, T.-K. Truong, L. Peng, T. A. Le, Y. Kawazoe, Generating highly active oxide-phosphide heterostructure through interfacial engineering to break the energy scaling relation toward urea-assisted natural seawater electrolysis, J. Energy Chem. 97 (2024) 687–699, https://doi.org/10.1016/j.jechem.2024.07.010.
[161] N. Chai, Y. Kong, Q. Jiang, Q. Guo, T. Chen, X. Ma, F.-Y. Yi, Vanadium - doped bimetallic nanoporous metal–organic frameworks as bifunctional electrocatalysts for urea-assisted hydrogen production, ACS Appl. Nano Mater. 7 (2024) 14392–14405, https://doi.org/10.1021/acsanm.4c01898.
[162] P. Wang, W. Zheng, Y. Qu, N. Duan, Y. Yang, D. Wang, H. Wang, Q. Chen, Photo-excited high-spin state Ni (III) species in Mo-doped Ni $_3$ S $_2$ for efficient urea oxidation reaction, Small (2024) 2403107, https://doi.org/10.1002/smll.202403107.
[163] J. Huang, L. Zou, S. Wang, Y. Zhang, P. Yang, W. Tao, J. Xie, In-situ electrochemical activation of a nickel metal-organic framework modified TiO2 photoanode for urea photoelectrocatalysis, J. Solid State Chem. 336 (2024) 124779, https://doi.org/10.1016/j.jssc.2024.124779.
[164] S. Xu, X. Ruan, M. Ganesan, J. Wu, S.K. Ravi, X. Cui, Transition metal-based catalysts for urea oxidation reaction (UOR): catalyst design strategies, applications, and future perspectives, Adv. Funct. Mater. 34 (2024) 2313309, https://doi.org/10.1002/adfm.202313309.
[165] S. Zhou, S. Lv, J. Shi, L. Zhang, J. Li, W. Cai, Self-supported ultrathin NiMn-LDH nanosheets for highly active and robust urea oxidation, Chem. Eng. J. 484 (2024) 149706, https://doi.org/10.1016/j.cej.2024.149706.
[166] J. Wan, Z. Wu, G. Fang, J. Xian, J. Dai, J. Guo, Q. Li, Y. You, K. Liu, H. Yu, W. Xu, H. Jiang, M. Xia, H. Jin, Microwave-assisted exploration of the electron configuration-dependent electrocatalytic urea oxidation activity of 2D porous NiCo2O4 spinel, J. Energy Chem. 91 (2024) 226–235, https://doi.org/10.1016/j.jechem.2023.12.017.
[167] J. Xie, R. Ding, Y. Li, J. Guo, Y. Zhang, Q. Fang, M. Yan, Y. He, Z. Yan, Z. Chen, X. Guo, Q. Yang, J. Luo, Y. Zhang, X. Sun, E. Liu, Surface reconstruction and synergistic electrocatalysis of perovskite K-Ni-Zn-F for efficient urea-based energy conversion, Nano Energy 126 (2024) 109669, https://doi.org/10.1016/j.nanoen.2024.109669.
[168] H. Du, H. Hu, X. Wang, N. Ran, W. Chen, H. Zhu, Y. Zhou, M. Yang, J. Wang, J. Liu, Vertical cross-alignments of 2D semiconductors with steered internal electric field for urea electrooxidation via balancing intermediates adsorption, Small 20 (2024) 2401053, https://doi.org/10.1002/smll.202401053.
[169] F. Fang, Y. Zhang, J. Bai, J. Li, X. Mei, C. Zhou, M. Zhou, B. Zhou, Efficient urine removal, simultaneous elimination of emerging contaminants, and control of toxic chlorate in a photoelectrocatalytic-chlorine system, Environ. Pollut. 267 (2020) 115605, https://doi.org/10.1016/j.envpol.2020.115605.
[170] Z. Shen, Y. Zhang, C. Zhou, J. Bai, S. Chen, J. Li, J. Wang, X. Guan, M. Rahim, B. Zhou, Exhaustive denitrification via chlorine oxide radical reactions for urea based on a novel photoelectrochemical cell, Water Res. 170 (2020) 115357, https://doi.org/10.1016/j.watres.2019.115357.
[171] Y. Ji, J. Bai, J. Li, T. Luo, L. Qiao, Q. Zeng, B. Zhou, Highly selective transformation of ammonia nitrogen to N2 based on a novel solar-driven photoelectrocatalytic-chlorine radical reactions system, Water Res. 125 (2017) 512–519, https://doi.org/10.1016/j.watres.2017.08.053.
[172] Y. Zhang, J. Li, J. Bai, Z. Shen, L. Li, L. Xia, S. Chen, B. Zhou, Exhaustive conversion of inorganic nitrogen to nitrogen gas based on a photoelectro-chlorine cycle reaction and a highly selective nitrogen gas generation cathode, Environ. Sci. Technol. 52 (2018) 1413–1420, https://doi.org/10.1021/acs.est.7b04626.
[173] Y. Zhang, J. Li, J. Bai, L. Li, S. Chen, T. Zhou, J. Wang, L. Xia, Q. Xu, B. Zhou, Extremely efficient decomposition of ammonia N to N2 Using ClO• from reactions of HO• and HOCl generated in situ on a novel bifacial photoelectroanode, Environ. Sci. Technol. 53 (2019) 6945–6953, https://doi.org/10.1021/acs.est.9b00959.
[174] Z. Shen, J. Li, Y. Zhang, J. Bai, X. Tan, X. Li, L. Qiao, Q. Xu, B. Zhou, Highly efficient total nitrogen and simultaneous total organic carbon removal for urine based on the photoelectrochemical cycle reaction of chlorine and hydroxyl radicals, Electrochim. Acta 297 (2019) 1–9, https://doi.org/10.1016/j.electacta.2018.11.087.
[175] S. Kim, G. Piao, D.S. Han, H.K. Shon, H. Park, Solar desalination coupled with water remediation and molecular hydrogen production: a novel solar water-energy nexus, Energy Environ. Sci. 11 (2018) 344–353, https://doi.org/10.1039/C7EE02640D.
[176] S. Kim, D.S. Han, H. Park, Reduced titania nanorods and Ni–Mo–S catalysts for photoelectrocatalytic water treatment and hydrogen production coupled with desalination, Appl. Catal. B Environ. 284 (2021) 119745, https://doi.org/10.1016/j.apcatb.2020.119745.
[177] G. Wang, Y. Ling, X. Lu, H. Wang, F. Qian, Y. Tong, Y. Li, Solar driven hydrogen releasing from urea and human urine, Energy Environ. Sci. 5 (2012) 8215, https://doi.org/10.1039/c2ee22087c.

[178] D. Xu, Z. Fu, D. Wang, Y. Lin, Y. Sun, D. Meng, T. feng Xie, A Ni(OH)2-modified Ti-doped α-Fe2O3 photoanode for improved photoelectrochemical oxidation of urea: the role of Ni(OH)2 as a cocatalyst, Phys. Chem. Chem. Phys. 17 (2015) 23924–23930, https://doi.org/10.1039/C5CP03310A.
[179] R. Zhao, G. Schumacher, S. Leahy, E.J. Radich, Ni(OH)2 as hole mediator for visible light-induced urea splitting, J. Phys. Chem. C 122 (2018) 13995–14003, https://doi.org/10.1021/acs.jpcc.8b01116.
[180] J. Liu, J. Li, M. Shao, M. Wei, Directed synthesis of SnO2@BiVO4/Co-Pi photoanode for highly efficient photoelectrochemical water splitting and urea oxidation, J. Mater. Chem. A 7 (2019) 6327–6336, https://doi.org/10.1039/C8TA11573G.
[181] G. Loget, C. Mériadec, V. Dorcet, B. Fabre, A. Vacher, S. Fryars, S. Ababou-Girard, Tailoring the photoelectrochemistry of catalytic metal-insulator-semiconductor (MIS) photoanodes by a dissolution method, Nat. Commun. 10 (2019) 3522, https://doi.org/10.1038/s41467-019-11432-1.
[182] P. Aroonratsameruang, P. Pattanasattayavong, V. Dorcet, C. Mériadec, S. Ababou-Girard, S. Fryars, G. Loget, Structure–property relationships in redox-derivatized metal–insulator–semiconductor (MIS) photoanodes, J. Phys. Chem. C 124 (2020) 25907–25916, https://doi.org/10.1021/acs.jpcc.0c08971.
[183] S.A. Lee, J.W. Yang, T.H. Lee, I.J. Park, C. Kim, S.H. Hong, H. Lee, S. Choi, J. Moon, S.Y. Kim, J.Y. Kim, H.W. Jang, Multifunctional nano-heterogeneous Ni(OH)2/NiFe catalysts on silicon photoanode toward efficient water and urea oxidation, Appl. Catal. B Environ. 317 (2022) 121765, https://doi.org/10.1016/j.apcatb.2022.121765.
[184] B. Kim, Y. Jung, B.J. Park, G. Das, H.H. Yoon, Y.S. Yoon, Photo-assisted electrolysis of urea using Ni-modified WO3/g-C3N4 as a bifunctional catalyst, Int. J. Hydrog. Energy 47 (2022) 5797–5806, https://doi.org/10.1016/j.ijhydene.2021.11.237.
[185] S. Park, J.T. Lee, J. Kim, Photocatalytic oxidation of urea on TiO2 in water and urine: mechanism, product distribution, and effect of surface platinization, Environ. Sci. Pollut. Res. 26 (2019) 1044–1053, https://doi.org/10.1007/s11356-017-8380-3.
[186] J. Gan, B.B. Rajeeva, Z. Wu, D. Penley, Y. Zheng, Plasmon-enhanced hierarchical photoelectrodes with mechanical flexibility for hydrogen generation from urea solution and human urine, J. Appl. Electrochem. 50 (2020) 63–69, https://doi.org/10.1007/s10800-019-01369-0.
[187] P.S. Gurudayal, T. Bassi, L.H. Sritharan, Wong, Recent progress in iron oxide based photoanodes for solar water splitting, J. Phys. Appl. Phys. 51 (2018) 473002, https://doi.org/10.1088/1361-6463/aae138.
[188] A.G. Tamirat, J. Rick, A.A. Dubale, W.-N. Su, B.-J. Hwang, Using hematite for photoelectrochemical water splitting: a review of current progress and challenges, Nanoscale Horiz. 1 (2016) 243–267, https://doi.org/10.1039/C5NH00098J.
[189] A. Tofanello, S. Shen, F.L. de Souza, L. Vayssieres, Strategies to improve the photoelectrochemical performance of hematite nanorod-based photoanodes, APL Mater. 8 (2020) 040905, https://doi.org/10.1063/5.0003146.
[190] T. Lindgren, H. Wang, N. Beermann, L. Vayssieres, A. Hagfeldt, S.-E. Lindquist, Aqueous photoelectrochemistry of hematite nanorod array, Sol. Energy Mater. Sol. Cells 71 (2002) 231–243, https://doi.org/10.1016/S0927-0248(01)00062-9.
[191] J. Dabboussi, Y. Zhao, R. Abdallah, A. Gicquel, C. Bendavid, G. Loget, Infrared photoelectrochemical sensing of urea with silicon photoanodes, Biosens. Bioelectron. X 12 (2022) 100221, https://doi.org/10.1016/j.biosx.2022.100221.
[192] S.A. Lee, J.W. Yang, T.H. Lee, I.J. Park, C. Kim, S.H. Hong, H. Lee, S. Choi, J. Moon, S.Y. Kim, J.Y. Kim, H.W. Jang, Multifunctional nano-heterogeneous catalysts on silicon photoanode toward efficient water and urea oxidation, Soc. Sci. Res. Netw. (2022), https://doi.org/10.2139/ssrn.4048940.
[193] G. Loget, C. Mériadec, V. Dorcet, B. Fabre, A. Vacher, S. Fryars, S. Ababou-Girard, Tailoring the photoelectrochemistry of catalytic metal-insulator-semiconductor (MIS) photoanodes by a dissolution method, Nat. Commun. 10 (2019) 3522, https://doi.org/10.1038/s41467-019-11432-1.
[194] J. Dabboussi, R. Abdallah, L. Santinacci, S. Zanna, A. Vacher, V. Dorcet, S. Fryars, D. Floner, G. Loget, Solar-assisted urea oxidation at silicon photoanodes promoted by an amorphous and optically adaptive Ni–Mo–O catalytic layer, J. Mater. Chem. A (2022), https://doi.org/10.1039/D2TA01212J.
[195] Y. Wang, M. Zu, X. Zhou, H. Lin, F. Peng, S. Zhang, Designing efficient TiO2-based photoelectrocatalysis systems for chemical engineering and sensing, Chem. Eng. J. 381 (2020) 122605, https://doi.org/10.1016/j.cej.2019.122605.
[196] K. Esquivel, L.G. Arriaga, F.J. Rodríguez, L. Martínez, L.A. Godínez, Development of a TiO2 modified optical fiber electrode and its incorporation into a photoelectrochemical reactor for wastewater treatment, Water Res. 43 (2009) 3593–3603, https://doi.org/10.1016/j.watres.2009.05.035.
[197] M. Antoniadou, P. Lianos, Photoelectrochemical oxidation of organic substances over nanocrystalline titania: optimization of the photoelectrochemical cell, Catal. Today 144 (2009) 166–171, https://doi.org/10.1016/j.cattod.2009.02.024.
[198] M.K. van Gelder, J.A.W. Jong, L. Folkertsma, Y. Guo, C. Blüchel, M.C. Verhaar, M. Odijk, C.F. Van Nostrum, W.E. Hennink, K.G.F. Gerritsen, Urea removal strategies for dialysate regeneration in a wearable artificial kidney, Biomaterials 234 (2020) 119735, https://doi.org/10.1016/j.biomaterials.2019.119735.
[199] Ž. Kovačič, B. Likozar, M. Huš, Photocatalytic CO_2 reduction: a review of ab initio mechanism, kinetics, and multiscale modeling simulations, ACS Catal. 10 (2020) 14984–15007, https://doi.org/10.1021/acscatal.0c02557.
[200] J. Albero, Y. Peng, H. García, Photocatalytic CO_2 reduction to C2+ products, ACS Catal. 10 (2020) 5734–5749, https://doi.org/10.1021/acscatal.0c00478.
[201] T. An, Y. Xiong, G. Li, C. Zha, X. Zhu, Synergetic effect in degradation of formic acid using a new photoelectrochemical reactor, J. Photochem. Photobiol. Chem. 152 (2002) 155–165, https://doi.org/10.1016/S1010-6030(02)00211-3.
[202] T. Lopes, P. Dias, L. Andrade, A. Mendes, An innovative photoelectrochemical lab device for solar water splitting, Sol. Energy Mater. Sol. Cells 128 (2014) 399–410, https://doi.org/10.1016/j.solmat.2014.05.051.
[203] C. Carver, Z. Ulissi, C.K. Ong, S. Dennison, G.H. Kelsall, K. Hellgardt, Modelling and development of photoelectrochemical reactor for H2 production, Int. J. Hydrog. Energy 37 (2012) 2911–2923, https://doi.org/10.1016/j.ijhydene.2011.07.012.
[204] A. Hankin, F.E. Bedoya-Lora, C.K. Ong, J.C. Alexander, F. Petter, G.H. Kelsall, From millimetres to metres: the critical role of current density distributions in photo-electrochemical reactor design, Energy Environ. Sci. 10 (2017) 346–360, https://doi.org/10.1039/C6EE03036J.
[205] A. Hankin, G. Kelsall, C.K. Ong, F. Petter, Photo-Electrochemical Production of H_2 Using Solar Energy, Chem. Eng. Trans. 41 (2014) 199–204. https://doi.org/10.3303/CET1441034.
[206] W. Xu, Z. Wu, S. Tao, Urea-based fuel cells and electrocatalysts for urea oxidation, Energy Technol. 4 (2016) 1329–1337, https://doi.org/10.1002/ente.201600185.
[207] D. Xu, Z. Fu, D. Wang, Y. Lin, Y. Sun, D. Meng, T. feng Xie, A Ni(OH) $_2$ -modified Ti-doped α-Fe $_2$ O $_3$ photoanode for improved photoelectrochemical oxidation of urea: the role of Ni(OH) $_2$ as a cocatalyst, Phys. Chem. Chem. Phys. 17 (2015) 23924–23930, https://doi.org/10.1039/C5CP03310A.
[208] S. Lu, X. Li, Y. Liao, G. Zhang, Optimized titania nanotubes photoanode mediated photoelectrochemical oxidation of ammonia in highly chlorinated wastewater via Cl-based radicals, Environ. Res. 214 (2022) 113972, https://doi.org/10.1016/j.envres.2022.113972.
[209] L. Wang, J. Yu, Principles of photocatalysis. in: Interface Sci. Technol., Elsevier, 2023, pp. 1–52, https://doi.org/10.1016/B978-0-443-18786-5.00002-0.
[210] Y. Liu, P. Cheng, T. Li, R. Wang, Y. Li, S.-Y. Chang, Y. Zhu, H.-W. Cheng, K.-H. Wei, X. Zhan, B. Sun, Y. Yang, Unraveling sunlight by transparent organic semiconductors toward photovoltaic and photosynthesis, ACS Nano 13 (2019) 1071–1077, https://doi.org/10.1021/acsnano.8b08577.
[211] A. Saravanan, V.C. Deivayanai, P.S. Kumar, G. Rangasamy, R.V. Hemavathy, T. Harshana, N. Gayathri, K. Alagumalai, A detailed review on advanced oxidation process in treatment of wastewater: mechanism, challenges and future outlook, Chemosphere 308 (2022) 136524, https://doi.org/10.1016/j.chemosphere.2022.136524.
[212] E. Mousset, D.D. Dionysiou, Photoelectrochemical reactors for treatment of water and wastewater: a review, Environ. Chem. Lett. 18 (2020) 1301–1318, https://doi.org/10.1007/s10311-020-01014-9.
[213] C.C. Ryan, D.T. Tan, W.A. Arnold, Direct and indirect photolysis of sulfamethoxazole and trimethoprim in wastewater treatment plant effluent, Water Res. 45 (2011) 1280–1286, https://doi.org/10.1016/j.watres.2010.10.005.
[214] G. Ren, H. Han, Y. Wang, S. Liu, J. Zhao, X. Meng, Z. Li, Recent advances of photocatalytic application in water treatment: a review, Nanomaterials 11 (2021) 1804, https://doi.org/10.3390/nano11071804.
[215] N. Ungureanu, V. Vlăduț, M. Cristea, D. Cujbescu, Wastewater electrooxidation using stainless steel electrodes, E3S Web Conf. 180 (2020) 03015, https://doi.org/10.1051/e3sconf/202018003015.
[216] Z. Zheng, J. Yuan, X. Jiang, G. Han, Y. Tao, X. Wu, Combining ultraviolet photolysis with in-situ electrochemical oxidation for degrading sulfonamides in wastewater, Catalysts 12 (2022) 711, https://doi.org/10.3390/catal12070711.
[217] B.R. Garza-Campos, J.L. Guzmán-Mar, L.H. Reyes, E. Brillas, A. Hernández-Ramírez, E.J. Ruiz-Ruiz, Coupling of solar photoelectro-Fenton with a BDD anode and solar heterogeneous photocatalysis for the mineralization of the herbicide atrazine, Chemosphere 97 (2014) 26–33, https://doi.org/10.1016/j.chemosphere.2013.10.044.
[218] S. McMichael, P. Fernández-Ibáñez, J.A. Byrne, A review of photoelectrocatalytic reactors for water and wastewater treatment, Water 13 (2021) 1198, https://doi.org/10.3390/w13091198.
[219] F.C. Moreira, R.A.R. Boaventura, E. Brillas, V.J.P. Vilar, Electrochemical advanced oxidation processes: a review on their application to synthetic and real wastewaters, Appl. Catal. B Environ. 202 (2017) 217–261, https://doi.org/10.1016/j.apcatb.2016.08.037.
[220] N. Borràs, C. Arias, R. Oliver, E. Brillas, Mineralization of desmetryne by electrochemical advanced oxidation processes using a boron-doped diamond anode and an oxygen-diffusion cathode, Chemosphere 85 (2011) 1167–1175, https://doi.org/10.1016/j.chemosphere.2011.09.008.
[221] E. Brillas, A review on the photoelectro-Fenton process as efficient electrochemical advanced oxidation for wastewater remediation. Treatment with UV light, sunlight, and coupling with conventional and other photo-assisted advanced technologies, Chemosphere 250 (2020) 126198, https://doi.org/10.1016/j.chemosphere.2020.126198.
[222] J.M. Navia-Mendoza, O.A.E. Filho, L.A. Zambrano-Intriago, N.R. Maddela, M.M.M.B. Duarte, L.S. Quiroz-Fernández, R.J. Baquerizo-Crespo, J.M. Rodríguez-Díaz, Advances in the application of nanocatalysts in photocatalytic processes for the treatment of food dyes: a review, Sustainability 13 (2021) 11676, https://doi.org/10.3390/su132111676.
[223] J. Singla, V.K. Sangal, A. Verma, Evaluation and optimization of the process parameters for the photo-electrochemical treatment of urea using mixed metal oxide anodes, Process Saf. Environ. Prot. 130 (2019) 197–208, https://doi.org/10.1016/j.psep.2019.08.017.
[224] M. Antoniadou, D.I Kondarides, D. Labou, S. Neophytides, P. Lianos, An efficient photoelectrochemical cell functioning in the presence of organic wastes, Sol. Energy Mater. Sol. Cells 94 (2010) 592–597, https://doi.org/10.1016/j.solmat.2009.12.004.

[225] S. Krishnan, V. Koning, M. Theodorus De Groot, A. De Groot, P.G. Mendoza, M. Junginger, G.J. Kramer, Present and future cost of alkaline and PEM electrolyser stacks, Int. J. Hydrog. Energy 48 (2023) 32313–32330, https://doi.org/10.1016/j.ijhydene.2023.05.031.
[226] S. Mikhaylin, L. Bazinet, Fouling on ion-exchange membranes: classification, characterization and strategies of prevention and control, Adv. Colloid Interface Sci. 229 (2016) 34–56, https://doi.org/10.1016/j.cis.2015.12.006.
[227] Q. Xu, S. Liu, F. Longhin, G. Kastlunger, I. Chorkendorff, B. Seger, Impact of anodic oxidation reactions in the performance evaluation of high-rate CO_2/CO electrolysis, Adv. Mater. 36 (2024) 2306741, https://doi.org/10.1002/adma.202306741.
[228] G. Chehade, M.E. Demir, I. Dincer, B. Yuzer, H. Selcuk, Experimental investigation and analysis of a new photoelectrochemical reactor for hydrogen production, Int. J. Hydrog. Energy 43 (2018) 12049–12058, https://doi.org/10.1016/j.ijhydene.2018.04.110.
[229] I. Sirés, E. Brillas, M.A. Oturan, M.A. Rodrigo, M. Panizza, Electrochemical advanced oxidation processes: today and tomorrow. A review, Environ. Sci. Pollut. Res. 21 (2014) 8336–8367, https://doi.org/10.1007/s11356-014-2783-1.
[230] L.C. Almeida, S. Garcia-Segura, N. Bocchi, E. Brillas, Solar photoelectro-Fenton degradation of paracetamol using a flow plant with a Pt/air-diffusion cell coupled with a compound parabolic collector: process optimization by response surface methodology, Appl. Catal. B Environ. 103 (2011) 21–30, https://doi.org/10.1016/j.apcatb.2011.01.003.
[231] S. Garcia-Segura, E.B. Cavalcanti, E. Brillas, Mineralization of the antibiotic chloramphenicol by solar photoelectro-Fenton, Appl. Catal. B Environ. 144 (2014) 588–598, https://doi.org/10.1016/j.apcatb.2013.07.071.
[232] J.M. Peralta-Hernández, Y. Meas-Vong, F.J. Rodríguez, T.W. Chapman, M. I. Maldonado, L.A. Godínez, In situ electrochemical and photo-electrochemical generation of the fenton reagent: a potentially important new water treatment technology, Water Res 40 (2006) 1754–1762, https://doi.org/10.1016/j.watres.2006.03.004.
[233] Y.-J. Shih, K.-H. Chen, Y.-H. Huang, Mineralization of organic acids by the photo-electrochemical process in the presence of chloride ions, J. Taiwan Inst. Chem. Eng. 45 (2014) 962–966, https://doi.org/10.1016/j.jtice.2013.09.010.
[234] K. Esquivel, L.G. Arriaga, F.J. Rodríguez, L. Martínez, L.A. Godínez, Development of a TiO2 modified optical fiber electrode and its incorporation into a photoelectrochemical reactor for wastewater treatment, Water Res. 43 (2009) 3593–3603, https://doi.org/10.1016/j.watres.2009.05.035.
[235] Z. Zhou, Y. Liu, J. Zhang, H. Pang, G. Zhu, Non-precious nickel-based catalysts for hydrogen oxidation reaction in alkaline electrolyte, Electrochem. Commun. 121 (2020) 106871, https://doi.org/10.1016/j.elecom.2020.106871.
[236] D.A. Keane, K.G. McGuigan, P.F. Ibáñez, M.I. Polo-López, J.A. Byrne, P.S. M. Dunlop, K. O'Shea, D.D. Dionysiou, S.C. Pillai, Solar photocatalysis for water disinfection: materials and reactor design, Catal. Sci. Technol. 4 (2014) 1211–1226, https://doi.org/10.1039/C4CY00006D.
[237] P. Fernandez-Ibañez, S. Malato, O. Enea, Photoelectrochemical reactors for the solar decontamination of water, Catal. Today 54 (1999) 329–339, https://doi.org/10.1016/S0920-5861(99)00194-7.
[238] G.R.P. Malpass, D.W. Miwa, A.C.P. Miwa, S.A.S. Machado, A.J. Motheo, Photo-Assisted Electrochemical Oxidation of Atrazine on a Commercial $Ti/Ru_{0.3}Ti_{0.7}O_2$ DSA Electrode, Environ. Sci. Technol. 41 (2007) 7120–7125, https://doi.org/10.1021/es070798n.
[239] J.R. Bolton, K.G. Bircher, W. Tumas, C.A. Tolman, Figures-of-merit for the technical development and application of advanced oxidation technologies for both electric- and solar-driven systems (IUPAC Technical Report), Pure Appl. Chem. 73 (2001) 627–637, https://doi.org/10.1351/pac200173040627.
[240] A.J. Bard, Inner-sphere heterogeneous electrode reactions. electrocatalysis and photocatalysis: the challenge, J. Am. Chem. Soc. 132 (2010) 7559–7567, https://doi.org/10.1021/ja101578m.
[241] Y. Sun, S. Bai, X. Wang, N. Ren, S. You, Prospective Life cycle assessment for the electrochemical oxidation wastewater treatment process: from laboratory to industrial scale, Environ. Sci. Technol. 57 (2023) 1456–1466, https://doi.org/10.1021/acs.est.2c04185.
[242] C.A. Martínez-Huitle, M.A. Rodrigo, I. Sirés, O. Scialdone, A critical review on latest innovations and future challenges of electrochemical technology for the abatement of organics in water, Appl. Catal. B Environ. 328 (2023) 122430, https://doi.org/10.1016/j.apcatb.2023.122430.